Growth and Characterization of Thin Film Electroluminescent Devices Fabricated Using Atomic Layer Epitaxy

Weiran Kong
B.S. of Physics, NanKai University, Tianjin, China, 1985
M.S.E.E., Oregon Graduate Institute of Science & Technology, 1993

A dissertation submitted to the faculty of the
Oregon Graduate Institute of Science & Technology
in partial fulfillment of the
requirements for the degree
Doctor of Philosophy
in
Applied Physics

April, 1996

The dissertation "Growth and Characterization of Thin Film Electroluminescent Devices Fabricated Using Atomic Layer Epitaxy" by Weiran Kong has been examined and approved by the following Examination Committee:

Rajendra Solanki, Advisor
Associate Professor

Reinhart Engelmann
Professor

Anthony Bell
Associate Professor

Richard T. Tuenge, Ph.D
Planar America

To Jin and Andy

Acknowledgments

I would like to express my deepest appreciation to my advisor, Dr. Raj Solanki for his guidance, encouragement and support.

I am grateful to the members of the thesis committee: Drs. Reinhart Engelmann, Tony Bell and Dick Tuenge for reviewing this dissertation and offering many helpful suggestions.

Especially, I would like to thank Dr. Dick Tuenge, Dr. Sey-Shing Sun and Dr. Chris Schaus of Planar America for their support and helpful discussion during the course of this work.

Many thanks are also due to John Fogarty, John Ferguson, Shafqad Ahmed, Jerry Boehme, Dr. SukRyong Hahn and Gregg Kruaval, for their constant cooperation and invaluable assistance.

Finally, I wish especially to thank my wife Jin, my son Andy and our parents for their understanding, support and encouragement.

Table of Contents

ACKNOWLEDGMENTS iv

TABLE OF CONTENTS v

LIST OF TABLES vii

LIST OF FIGURES viii

LIST OF SYMBOLS xi

LIST OF ACRONYMS xiii

ABSTRACT xv

Chapter 1 Introduction 1

Chapter 2 Electroluminescent display 7

2.1 History of electroluminescence 7

2.2 The ACTFEL device structure and fabrication 8

2.3 ACTFEL device physics 10

2.4 ACTFEL device characterization by electrical measurement 14

2.5 Energy levels of rare earth atoms in a crystal 15

2.6 Device modeling 19

Chapter 3 Atomic layer epitaxy 22

3.1 History 22

3.2 Mechanisms of ALE 22

Chapter 4 Thin film synthesis by ALE and initial characterization 28

4.1 Introduction of the F-120 ALE reactor 28

4.2 Synthesis of Al_2O_3 by ALE 32
4.3 Synthesis of ZnS by ALE 35
4.4 Synthesis of SrS by ALE 43
4.5 Structure characterization by grazing incident angle X-ray diffraction 45
4.6 ACTFEL device fabrication by ALE 49
Chapter 5 Characterization of ZnS:Tb EL devices 52
5.1 Electrical characterization methods for ACTFEL devices 52
5.2 The dynamic study of polarization charge and internal field with the assistance of ultraviolet laser radiation 55
5.3 EL efficiency study of ZnS:Tb devices treated by rapid thermal annealing and at low temperature 61
5.4 Numerical modeling of C-V characteristics of ZnS:Tb ACTFEL devices 67
Chapter 6 Optical characteristics of the EL devices 72
6.1 Praseodymium doped SrS and ZnS 72
6.2 SrS:Ce, SrS:Eu and $SrCl_2$:Eu based devices 76
6.3 Summary 87
Chapter 7 Summary and conclusions 90
References 94
Vita 100

List of Tables

Table I	Diffraction peaks of ZnS grown on glass at various temperatures.	47
Table II	The process conditions of different types of phosphor layers.	50
Table III	Relaxation time and brightness of ZnS:Tb devices.	62
Table IV	Comparison of physical properties of SrS, CaS and ZnS.	74
Table V	Summary of TFEL device emission characteristics.	88

List of Figures

2.2.1	ACTFEL display device structure.	9
2.3.1	Schematic of ACTFEL device and electron tunneling model.	11
2.6.1	Equivalent circuit of a TFEL device.	20
3.2.1	Energy diagram comparing chemical and physical adsorption.	23
3.2.2	Processing temperature window ($T_{low} < T < T_{high}$) for atomic layer epitaxy process.	25
4.1.1	Schematic diagram of F-120 substrate holder.	30
4.1.2	Schematic of F-120 ALE reactor system.	31
4.2.1	Reactant gas pulse sequence in the ALE process.	33
4.2.2	Growth rate vs. temperature of Al_2O_3 ALE thin films grown on glass from $AlCl_3$ and $(CH_3)_3COH$.	34
4.3.1	Temperature dependence of ZnS growth rate.	37
4.3.2	Non-uniformity factor vs. temperature for ZnS grown on glass and ITO.	39
4.3.3	Dielectric constant variation of ZnS grown at different temperatures.	40
4.3.4a	AFM image of sample #14, grown on Al_2O_3 at 500 °C for 400 cycles (thickness≈360 Å).	41
4.3.4b	AFM image of sample #35, grown on Al_2O_3 at 500 °C for 6000 cycles (thickness≈5400 Å).	42
4.4.1	Temperature dependence of SrS growth rate grown on glass substrate.	44
4.5.1	X-ray diffraction patterns of ZnS thin films grown on glass substrates at various temperatures: (a) 380°C, (b) 420°C, (c) 460°C and (d) 500°C.	46

4.5.2 Ratio of X-ray diffraction peak intensity, peak (103) over peak (002). 48

4.6.1 Cross section view of the EL device fabricated by ALE process. 49

5.2.1 Experimental setup for characterizing EL device with UV radiation. 56

5.2.2 The emission intensity of the ZnS:Tb EL device with and without the laser radiation versus the operating pulse amplitude. 57

5.2.3 The charge $Q_l(t)$ stored at the phosphor/oxide interface (a), and the average electric field (b) at 130 V pulses, with and without 352 nm radiation. 59

5.2.4 The charge $Q_l(t)$ stored at the phosphor/oxide interface (a), and the average electric field (b) at 250 V pulses, with and without 352 nm radiation. 60

5.3.1 Emission spectrum of ZnS:Tb electroluminescent device. 64

5.3.2 Transferred charge (ΔQ) versus brightness plot for the medium doped device at f = 1kHz showing higher efficiency after RTA treatment. 65

5.3.3 Relationship between brightness and frequency for the medium doped as-grown device showing the brightness enhancement at lower temperature (77 K). 66

5.4.1 C-V characteristics from experimental measurement and computer simulation, based on a ZnS:Tb ACTFEL device. 68

6.1.1 Emission profiles of ZnS:Pr and SrS:Pr/ZnS electroluminescent devices. 73

6.1.2 Applied voltage pulse across the SrS:Pr/ZnS EL device and its corresponding current and optical emission response. 75

6.2.1 Electroluminescent and photo-luminescent emission spectra of the violet light emission from $SrCl_2$:Eu in type A devices. 77

6.2.2 Electroluminescent emission spectrum of type B device, SrS:Eu without ZnS buffer layers. 79

6.2.3 The driving voltage pulse (a); the corresponding emission of orange-red light from type B devices (b); and violet light from type A devices (c). 81

6.2.4 X-ray diffraction patterns of (i) device type B, without ZnS layer; (ii) device type A, with two ZnS buffer layers; (iii) device with ten ZnS-SrS alternative layers. 83

6.2.5 EL spectrum of the UV light emission from $SrCl_2$:Ce in type A devices. 85

6.2.6 Electroluminescent emission spectrum of type B devices, SrS:Ce/Eu without ZnS buffer layers. 86

6.3.1 CIE (Commission Internationale de l'Eclairage) coordinates measured from the devices shown in diagram. The CIE number of SrS:Ce with blue filter is from the reference [88] 89

List of Symbols

ν	Frequency of a photon
ε	Energy
θ	Diffraction angle
C	Capacitance
C_{ox}	Capacitance of oxide
C_{ph}	Capacitance of phosphor
C_s	Capacitance of the series capacitor in the Sawyer-Tower circuit
d	Growth rate
E_c	Activation energy of chemical adsorption
E_p	Activation energy of physical adsorption
eV	Electron volt
h	Plank constant
H_{total}	Total Hamiltonian of an atom
I	Current
I_d	Displacement current
k	Boltzmann constant
m^*	Effective mass of electron
m_e	Mass of electron
$N(\varepsilon)$	Energy distribution function
Q_l	Polarization charge
R	Resistance

R_{ox}	Resistance of oxide
R_{ph}	Resistance of phosphor
T	Temperature
V	Voltage
V_t	Breakdown voltage

List of Acronyms

ACTFEL	Alternating current thin film electroluminescence
AFM	Atomic force microscopy
ALE	Atomic layer epitaxy
ATO	Aluminum-Titanium oxide
BTO	Barium-Tantalum oxide
CRT	Cathode-ray tube
CV	Capacitance -voltage
CVD	Chemical vapor deposition
DUT	Device under test
EL	Electroluminescence
FE	Falling edge
FWHM	Full width at half maximum
HDTV	High definition television
ITO	Indium-Tin oxide
IV	Current-voltage
JCPDS	Joint committee of powder diffraction standards
LCD	Liquid crystal display
LE	Leading edge
LED	Light emitting diode
LPCVD	Low pressure chemical vapor deposition
PC	Personal computer

PL	Photoluminescence
RTA	Rapid thermal annealing
SID	Society for Information Display
SIMS	Secondary ion mass spectroscopy
STN	Super twist nematic
TFEL	Thin film electroluminescence
TFT	Thin film transistor
UV	Ultra violet

Abstract

Growth and Characterization of Thin Film Electroluminescent Devices Fabricated Using Atomic Layer Epitaxy

Weiran Kong

Supervising Professor: Rajendra Solanki

The thesis examines two aspects of electroluminescent (EL) devices. First, the atomic layer epitaxy (ALE) process, where thin film synthesis technique for growing Al_2O_3, ZnS and SrS on glass substrate is discussed. The second topic is electrical and spectral characterization of EL devices fabricated by ALE.

For Al_2O_3, the surface reaction was found to be exothermic, and the thin film was identified as amorphous by X-ray diffraction. For ZnS, atomic force microscope showed that the grain size is small at the beginning of growth and became larger as the growth progressed; X-ray diffraction showed that the thin film had a tendency to be in the hexagonal phase at higher substrate temperature (500 °C) and in the cubic phase at lower substrate temperature (400 °C). For SrS, the thin film was sodium chloride type cubic structure based on X-ray diffraction. During the SrS based EL device fabrication it was also found that when a ZnS buffer layer was grown prior to the SrS layer growth, a cubic $SrCl_2$ layer was formed near the ZnS-SrS interface. $ZnCl_2$, which is one of the precursors for ZnS growth, is believed to be the souce of chlorine.

A number of phosphor layers, including ZnS:Tb, ZnS:Pr and SrS:Pr, SrS:Eu and ZnS-SrS:Eu, SrS:Ce and ZnS-SrS:Ce were grown by ALE between the Al_2O_3 thin films to form different types of EL devices. Electrical and optical properties of the ZnS:Tb EL devices were characterized by various techniques, including C-V measurement, internal field and polarization charge measurement. Brightness vs. frequency measurement at room temperature and 77 K was used to show the effect of thermal quenching on EL efficiency. The enhancement and attenuation of EL emission by UV radiation on ZnS:Tb devices showed that the polarization charge was critical to the luminescent efficiency. Rapid thermal annealing (RTA) was performed on ZnS:Tb based device and showed a positive effect on electroluminescent efficiency. The numerical modeling results based on the tunneling model showed good agreement with the measured data, and the modeled parameters related to the electron density of states function were extracted. The model showed that the interface states are located about 0.7 eV below the ZnS conduction band.

Electroluminescence spectra and CIE (Commission Internationale de l'Eclairage) coordinates were measured. For the first time, two new emission peaks 406 nm from $SrCl_2$:Eu and 360 nm from $SrCl_2$:Ce were observed. The corresponding emission mechanism and energy levels were identified. The concept of the $SrCl_2$:Eu based purple light emitting device could be useful in the next generation full color TFEL display applications.

Chapter 1
Introduction

As portable computers and hand-held communication products are becoming popular, flat panel display devices are in increasing demand. Presently, there are several different technologies available for making flat panel displays, namely: liquid crystal, plasma, electroluminescent and field emission. Each of these technologies has its strengths and weaknesses. Because of the diversity of application requirements, these competing technologies are co-existent on the flat panel market. The electroluminescent (EL) display, as one of the most important flat panel display technologies, has gained a respectable market share due to its unique features, such as robustness, high brightness, good viewing angle and high resolution. In this chapter, the major flat panel display technologies are briefly reviewed. The remainder of the text will be devoted to the technology of thin film electroluminescence (TFEL) displays and the scope of this research work.

Liquid crystal display (LCD)

Currently liquid crystal displays are the dominant products in the flat panel display market. The basic operating mechanism of a liquid crystal display is based on the electro-optic effect of the liquid crystals. Because liquid crystals do not emit light, ambient light or backlighting is required. For this reason LCD is often categorized as a non-emissive display. Other types of displays are characterized as emissive, i.e., light is generated and emitted.

The thin film transistor (TFT) LCD, also known as active matrix LCD [1], offers the best color and contrast to laptop computers and small screen TVs on the market today. The idea of TFT is to use one thin film transistor for each pixel to increase the non-linearity of the liquid crystal light valve. By doing so the potential "cross talk" between pixels is greatly reduced and as a result the contrast of the display is increased. The major drawback of TFT LCD technology is an increased complexity for manufacturing, resulting in lower yield and higher cost. Because the number of transistors increases with the square of the display diagonal length, large screen displays using TFTs are difficult to produce. To date the largest TFT LCD (made by Sharp, 1994) is limited to 21 inches diagonal.

To increase non-linearity another technique, super twisted nematic (STN) LCD has been used [2]. This involves twisting liquid crystal by 270° instead of 90° as in a regular twisted nematic (TN) cell. These cells are less expensive to manufacture than the TFT technology. However, the performance of STN LCD has not yet been close to the expensive TFT counterpart. The engineers at InFocus have developed a new addressing algorithm called active addressing [3]. They are working on applying this technique to STN LCD to enhance performance without paying the high cost of TFT technology.

At present the trend of LCD technology development favors active matrix TFT technology for full color display applications. Ongoing research includes using polysilicon to replace amorphous silicon for making the thin film transistors. This will increase speed and possibly integrate display driver circuitry on the display panel. It is expected that as production volume increases, the manufacturing cost will eventually go down for TFT LCD products.

Plasma display

The working mechanism of plasma display is very similar to commonly used fluorescent lamps. The pixel cell consists of a cavity filled with discharge gases (Ne and Xe) and two electrodes. When the applied voltage reaches threshold two plasma glow zones, positive and negative, are formed. The negative glow produces UV radiation which stimulates a phosphor deposited on the glass substrate to produce fluorescent light. Owing to the physical limitation of the size of the cell (it has to be larger than certain dimensions (0.65 mm average pitch size [4]) in order to sustain a plasma glow), the plasma display is more suitable for large screen display applications. Large (40") screen color plasma displays operating in the HDTV video mode were demonstrated at the SID '94 conference [4]. The problems associated with plasma displays include: high operating voltage, low luminance and low luminous efficiency.

Field emission display (FED)

Field emission display technology is still in its infancy. The idea of field emission display is to utilize the mature phosphor technology of CRT displays, and to replace the hot electron gun of the CRT with an array of tiny cold field emission tips. At SID '94, a prototype field emission display was demonstrated [5]. The cone shaped tips were made by selective etching of a Si substrate. A layer of "amorphic diamond" thin film was coated on the tips to reduce the surface work function. The display was a 50x50 matrix and it was the very first prototype demonstrated. As yet there are no field emission displays on the market.

Electroluminescent displays

Commercial electroluminescent flat panel displays have been around for over a decade. These products are mostly used as displays for aviation, measurement, and medical instruments. The technology has proven to be very reliable, even in some extreme environments. It is characterized by high resolution, fairly good brightness, and good power efficiency (~ up to 6 lm/W) [6]. It is an emissive type display and very close to an ideal Lambertian light source, i.e., it does not have a viewing-angle problem. Large screen (19 inch) displays have been produced commercially.

For years, however, electroluminescent display products have been limited to a monochrome orange-yellow color based on the standard ZnS:Mn material system. There has been a constant effort to find a new material system that can deliver blue and green color emission and yet maintain high brightness and good reliability. It has been shown that terbium doped ZnS thin film EL devices can deliver green light close to the brightness requirement for flat panel display purposes [7, 8]. Recently great progress has been made on thiogallate (MGa_2S_4, M=Sr or Ca) [9] systems doped with Ce, which emits blue light with a wavelength peak centered at 455 nm [10]. This progress led to the first prototype full color electroluminescent display introduced at SID '93 by Planar Systems. Because three different material systems were used, namely ZnS:Mn and ZnS:Tb for red and green grown by atomic layer epitaxy (ALE) technique, and strontium thiogallate:Ce for blue which was sputter deposited, the device had to be made on two separate glass substrates. This overlaid substrate structure has increased complexity of fabrication. For this reason a system with a broad emission spectrum covering blue, green and red, i.e. a white light phosphor, is highly desirable.

Strontium sulfide is a wide band gap II-VI semiconductor (E_g = 4.3 eV) which is a well known orange-red light emitting phosphor when doped with Eu and a blue-green light emitting phosphor when doped with Ce [11, 12]. It was expected that a broad emission spectrum could be achieved by combining Ce and Eu in SrS TFEL devices. A few research groups have been working along this direction, using different deposition techniques, such as sputtering and e-beam evaporation for making SrS thin films [11,12,13]. The results reported to date are promising but more effort is needed in order to achieve efficient and stable full color display devices for commercial production.

The purpose of this research was to synthesize ZnS and SrS thin film EL devices using atomic layer epitaxy (ALE) technique and to study the electrical and spectral properties of these devices. Since ZnS thin film synthesis using ALE technique is a relatively mature process, ZnS thin film devices based on ZnS:Tb were initially produced to characterize the ALE reactor. This was followed by ALE growth of poly-crystalline SrS thin film. The SrS thin film devices synthesized by ALE have demonstrated broad spectra and new emission peaks.

This thesis contains 7 chapters including this introduction. The review of the EL flat panel display technology and the ALE thin film growth technology are presented in Chapter 2 and 3, respectively. In Chapter 4, the experimental results of the Al_2O_3, ZnS and SrS thin film syntheses by ALE technique are described. The X-ray diffraction analyses of the thin films are also presented. Chapter 5 and Chapter 6 present the electrical and optical properties of the EL devices. In Chapter 5, various characterization techniques and the experimental results of the ZnS:Tb device are described. A model based on electron tunneling is developed to explain the observed electrical properties. In Chapter 6, electroluminescent spectra of the devices made of ZnS, SrS and $SrCl_2$ are presented. The

energy levels of the rare earth ions responsible for emission are identified and transition mechanisms are discussed. Summary and conclusions are presented in Chapter 7.

Chapter 2
Electroluminescent Display

In this chapter, the literature relevant to alternating-current thin-film electroluminescent (ACTFEL) devices are reviewed. The history of electroluminescence, ACTFEL device structure, basic device physics, device characterization techniques, fundamentals of luminescence spectroscopy and three levels of the ACTFEL device modeling are discussed.

2.1 History of electroluminescence

Electroluminescence is defined as light generation by electricity or energetic electrons traversing a material. In scientific literature, two phenomena have been commonly referred to as electroluminescence. One is light from light emitting diodes (LEDs), where light is generated by electron-hole pairs (band to band recombination) close to a p-n junction. The other one is light generated by light emitting centers via collisions with hot electrons that are accelerated by a strong electrical field. In this thesis the later one, i.e. the high field electroluminescence (EL) will be explored in detail.

Destriau first reported luminescence from ZnS under the influence of an electrical field [14]. Later, "powder type" EL devices were studied for years with the expectation of achieving a "cold" light source for illumination. However, two problems; its inefficiency of energy-light conversion and short life span proved to be insurmountable. In the 1960's, the advance of research in the semiconductor industry provided a higher level of knowledge

about semiconductor material properties and crystal growth techniques. At that time, a group of researchers at Bell Labs studied thin film EL devices doped with rare earth elements [15, 19]. The research was discontinued when the field clamping behavior due to the polarization charge of this type of thin film devices was recognized. The revitalization of interest in EL devices started from the early 70's when Inoguchi proposed a double insulator sandwich structure [16], which increased the life span of the new devices significantly. In the late 70's, AC thin film EL displays became reality and in the early 80's commercial monochrome EL display products were made in Japan, Finland and the United States. Recently Planar America started its commercial full color VGA EL display production.

2.2 The ACTFEL device structure and fabrication

EL devices can be classified into four categories [17]: DC powder, AC powder, DC thin film and AC thin film. Although powder type EL devices may be inexpensive to make, for flat panel display applications, AC thin film electroluminescent (ACTFEL) devices have proven to be superior in many aspects, including its increased brightness and longer life span. The first ACTFEL structure was reported by Inoguchi et al. [16] as mentioned earlier. It was a multilayer structure composed of a ZnS:Mn phosphor layer sandwiched between two insulator layers. The structure of a typical ACTFEL device is shown in Fig. 2.2.1. The device is fabricated on a glass substrate and consists of a phosphor layer sandwiched between two insulating layers and a pair of electrodes. The lower electrode is usually Indium-Tin Oxide (ITO). This material is used because it is transparent to visible light and it has low sheet resistance. The insulator is typically Silicon

Oxinitride (SiON), Barium Tantalum Oxide (BTO), Aluminum Titanium Oxide (ATO) or Aluminum Oxide (Al_2O_3). These materials are chosen because they have high dielectric constants and high resistance to electrical breakdown. The reason for choosing a material with higher dielectric constant to be the insulating layer, is that the voltage drop across the dielectric would be smaller and therefore the voltage drop across the phosphor layer would be larger. Typically, the phosphor layer consists of ZnS, doped with manganese (ZnS:Mn), or SrS doped with rare earth elements (SrS:Ce, Eu...).

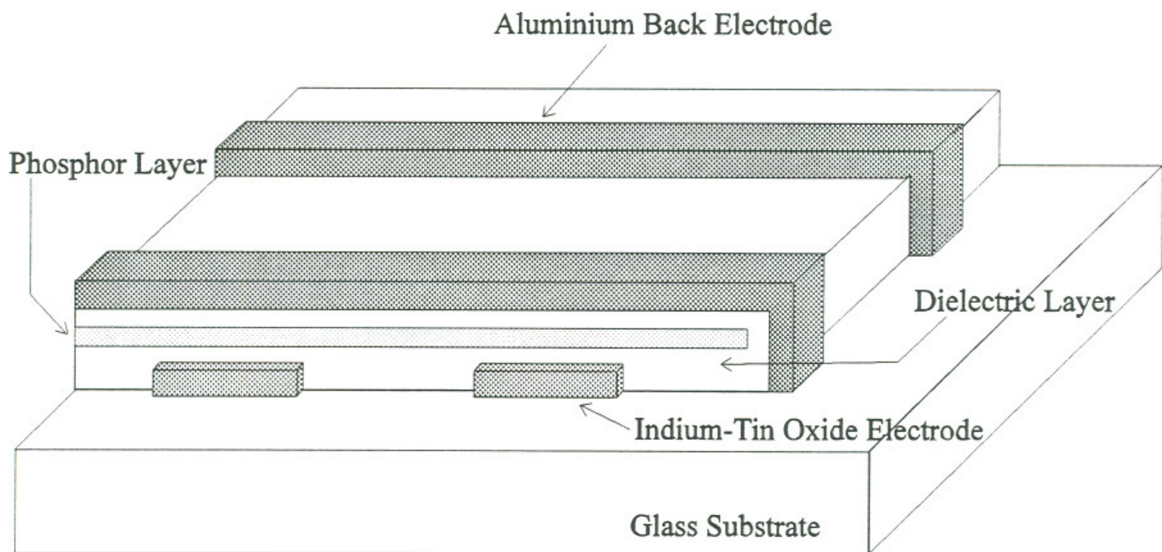

Fig. 2.2.1 ACTFEL display device structure.

The ACTFEL fabrication process begins with an ITO coated glass substrate. Deposition of thin film insulators and phosphors can be achieved by evaporation, sputtering, or chemical vapor deposition methods. This thesis focuses on devices

fabricated by atomic layer epitaxy (ALE). The detailed discussion of the ALE process is presented in chapter 3 and chapter 4.

2.3 ACTFEL device physics

The double insulating layer sandwich structure of the ACTFEL device demands operation in an AC environment. If an AC pulse is not used then the conducting charge inside the phosphor layer will build up at one of the insulator interfaces creating a local electrical field opposite to the applied field. This is called polarization charge. The polarization charge gives rise to a phosphor field component that opposes additional charge accumulation. To generate constant light a bipolar pulse sequence has to be applied. The bipolar pulse drives the conducting charge back and forth between the two interfaces.

Experimental evidence points to the electron as the primary conducting charge [18]. Therefore the electron transportation mechanism and the energy transfer mechanism between "hot electrons" and optical activators are the key in understanding the physics of EL device operation.

2.3.1 Electron tunneling theory

Under AC operation, electrons start traveling between the two phosphor-insulator interfaces only after the voltage pulses reach a threshold or breakdown. The electron states at the interfaces are commonly referred to as interface states. The interface states can hold electrons in between the pulses until the next pulse reaches the breakdown level, then electrons start tunneling out of the interface states with assistance of Poole-Frenkel

barrier lowering [20], see Fig. 2.3.1. Accurate information of the interface states, i.e., its location and distribution function are not clear. More discussion of computer simulation of the interface states is offered in section 5.4. The prevailing estimate for the energy levels of the interface states is about 0.6-1.0 eV below the phosphor conduction band [20, 21, 22, 23].

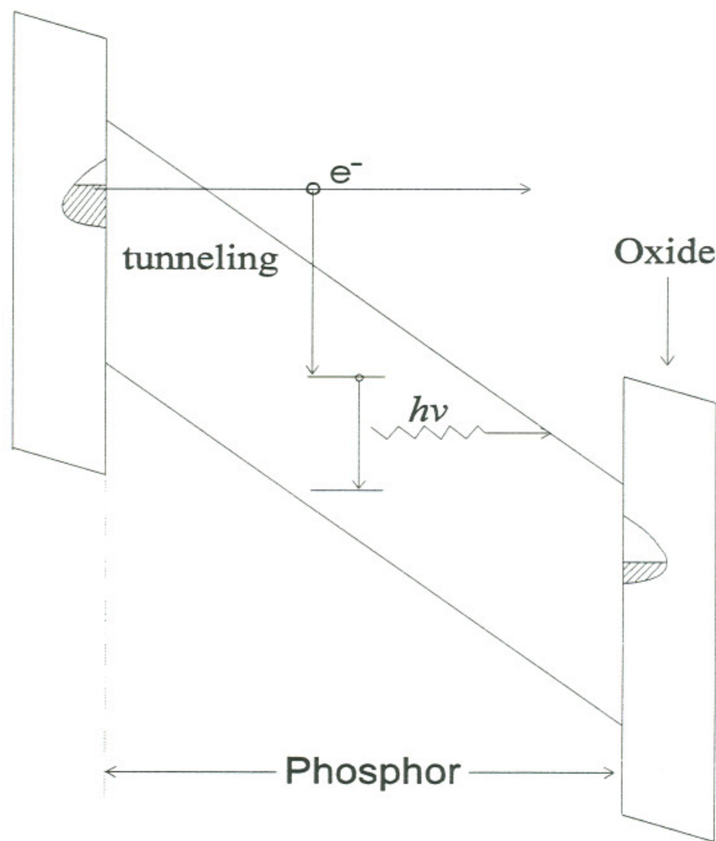

Fig.2.3.1 Schematic of ACTFEL device and electron tunneling model.

2.3.2 Electron transport in a wide band gap semiconductor

Electrons tunneling out of the interface states are accelerated under strong electrical field and gain energy. If the electron has gained sufficient energy in the process of acceleration, it may impact excite a luminescent impurity prior to reaching the other interface. In order to excite a luminescent center and emit visible light, the electron has to gain at least 2.0 eV during the acceleration. This implies the electron can not be in thermal equilibrium with the host lattice [24, 25]. Therefore these accelerated electrons are commonly referred to as "hot electrons". A Monte Carlo model on electron transport must consider lattice scattering, impurity scattering, phonon scattering, electron mutual scattering and so on [26, 27, 28]. As a result one can plot the electron energy distributions under different electrical fields. The simulations done by different authors have so far resulted in much controversy mainly due to the complexity of the problem, and the detailed discussion is beyond the scope of this work. However it should be pointed out that some of the electrons could gain enough energy to create band to band impact excitation [29,30], whether there actually is an avalanche effect in ACTFEL devices, however, is not known

Space charge inside the phosphor is another controversial issue in device operation. Space charge may be created by: (i) trapping of electrons tunneling from interface states, (ii) ionization of the impurities due to hot electron impact [31]. The existence of space charge causes a non-uniform electrical field inside the phosphor, possibly reducing the turn-on voltage. In addition, space charge results in Coulombic attractions to the electrons at the interface, leading to radiative or non-radiative recombination.

2.3.3 Impact excitation and indirect excitation

The strong electrical field can generate hot electrons with kinetic energy more than 2 eV. These hot electrons then transfer energy to the activators to emit photons. Two common energy transfer mechanisms governing this process are direct impact excitation and indirect excitation.

The direct impact excitation mechanism was proposed for the first time by Krupka for a ZnS:Tb device [32]. In this process, intra-shell emission of the rare earth ion is excited by impact with a hot electron accelerated by the strong electrical field. The process of impact excitation can be treated as inelastic scattering of hot electrons at the activator site. The cross section is determined by three factors [33, 34]; one is the host lattice property which causes a screening effect on the ion; the second is the excitation energy, i.e., activators with lower excitation energy has a larger cross section than with higher excitation energy; the third is the relaxation rate (lifetime) of the excited ion, the faster it relaxes, the more chances it will have, to be impact excited again.

An indirect excitation is a multi-step process involving at least one other center which does not relax quickly [35]. One typical scenario is the energy transfer from the initially excited activator to a nearby activator. Another case is that the activator can lose an electron to the conduction band and later recapture it to be at an excited state, i.e., goes through an ionization and recombination process. This excitation mechanism is determined by the properties of the host lattice and the activator. More discussion about the direct impact excitation and recombination process is presented later in conjunction with the specific devices.

In summary, in the ACTFEL device operation process, after reaching breakdown voltage, the trapped electrons are initially tunneled out of the interface states. Electrons

then accelerate in the strong electrical field to gain energy; energy is being transferred to the activators via direct or indirect excitation; and finally light is emitted. These are the most important aspects involving the ACTFEL device operation. In-depth discussions on these subjects will appear later.

2.4 ACTFEL device characterization by electrical measurement

Fundamentally, there are only a few electrically measurable quantities. Externally one can measure the total current flowing through the device as a function of time. Current is measured with either a current probe or a voltage drop across a small resistor in series with the device. Total external charge (charge on the electrode) is conveniently measured as function of time by measuring the voltage drop on a large capacitor in series with device. This is known as the Sawyer-Tower configuration [36]. The internal current flowing in the phosphor, i.e. the conduction current, can be measured with a bridge circuit [37] or mathematically determined by subtracting the displacement current from the total current. By knowing the external charge and the external voltage drop the polarization charge can be deduced, provided the device structure, i.e. each layer's thickness and its dielectric constant are known.

There are a few techniques to determine the electrical characteristics of TFEL devices. Those include I-V, C-V and Q-V measurement [38, 39]. These data are informative about the properties of the phosphor; among them the most important information is the breakdown voltage. It should be pointed out that the three techniques mentioned above are correlated. For instance, the polarization charge could be calculated

by integration of conductive current with time, i.e. by measuring I-V, the Q-V relation is known [40]. Some authors defined capacitance of a TFEL device as [40, 41],

$$C = \frac{dQ}{dV} = \frac{I}{dV/dt}$$

where dV/dt is a constant since a linear voltage ramp was applied. As a result, the C-V plot in this case is the same as I-V plot multiplied by a constant.

One should note here that these calculations were usually done with the assumption that there is no space charge distribution in the phosphor layer, i.e. the electrical field is a constant across the phosphor. The ionization of activators or other impurities in the phosphor layer would lead to the existence of space charge. Only when the majority of the polarization charge directly results from ionization in the phosphor, the space charge contribution to phosphor field could not be ignored.

2.5 Energy levels of rare earth atoms in a crystal

The phosphor layers in ACTFEL devices are usually made of wide band II-VI semiconductors doped with rare earth elements which serve as activators emitting visible light. To understand the spectral and emission characteristics of ACTFEL devices, it is necessary to review the fundamentals of energy levels of rare earth atoms in a crystal.

The rare earth elements have in common an unfilled 4f shell. They exist as doubly or triply positively charged ions in ionic solids such as ZnS and SrS. All trivalent rare earth ions have the xenon-like shell of 54 electrons in common and contain n 4f additional

electrons, with n ranging from 1 (Ce^{3+}) to 13 (Yb^{3+}). For example, Europium has the following electron configuration in its ground state:[42]

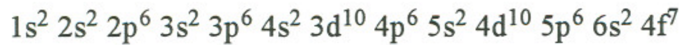

$$1s^2\ 2s^2\ 2p^6\ 3s^2\ 3p^6\ 4s^2\ 3d^{10}\ 4p^6\ 5s^2\ 4d^{10}\ 5p^6\ 6s^2\ 4f^7$$

where there are 7 electrons in the 4f subshell. The 6s subshell is filled in the neutral atom but is stripped off in the ions of interest, Eu^{2+} and Eu^{3+}, where for Eu^{3+} one additional electron from the 4f subshell is lost, making it $6s^0 4f^6$. The 5s and 5p subshells remain filled and they form a spherical symmetrical charge distribution whose mean radius is larger than the mean radius of 4f electrons. Therefore the optically active 4f electrons are partially shielded from the outside electrical field perturbations.

The rare earth ions in gas form at low pressure can be considered as isolated ions. Their emission and absorption spectra, therefore, consist of very sharp lines. The line width of the emission peaks is the natural width broadened by the Doppler Effect, i.e., the effects of free ion movement. However when a rare earth ion is placed in a crystal lattice, its energy levels are different from a free moving ion because of the perturbations from the crystal field. It is always possible to formulate Schrödinger's equation to determine the energy levels of an atom in a crystal. Consider an optically active atom in a crystal surrounded by a space lattice of atoms. The total Hamiltonian is:[43]

$$H_{total} = (H_0 + H_{SO} + H_{LS}) + H_{crystal\ field} + H_{phonon}$$

where,

H_0 is the Coulombic potential due to atomic nucleus and the screening of inner shell electrons. It yields quantum numbers n, l, m, s, which represent main orbit, subshells, directions of subshell orbit and electron spin, respectively.

H_{SO} is the effect of spin-orbit coupling.

H_{LS} is the effect of LS coupling which is important when considering multi-electron interaction within an unfilled subshell.

$H_{crystal\ field}$ is the electrical field contribution from the surrounding atoms.

H_{phonon} is the interaction between thermal vibration of lattice and the atom of interest.

Considering LS coupling, the spin angular momenta of all electrons add together, so do the orbital angular momenta, giving rise to a total spin s' and a total orbital momentum l'. The resulting energy levels from LS coupling are labeled as, for instance, $^5D_4$ for $4f^6$ electrons of Eu^{3+}. The superscript is 2s'+1. The capital letter designates l'(S, P, D, F, G…). The subscript is j' which is formed by adding s' and l' as vectors.

The ground states of both divalent and trivalent rare earth ions have electronic configurations of the 4f subshell; but an excited electron can stay either in the 4f subshell or move to the 5d subshell. For divalent rare earth ions, the first excited states have an electronic configuration of $4f^n5d$. For most trivalent ions the excited state still has a 4f configuration with the exception for Ce^{3+}.

When an electron is in an excited state with $4f^n5d$ configuration, the 5d electron is not well shielded since the radius of the 5d electron is larger than the 5s5p subshell. As a result the d type electronic states are sensitive to the crystal field of host lattice. In rare earth doped alkaline-earth sulfide TFEL devices, the d state electron can even escape to the conduction band, and become a free electron. It can also be recaptured by the activator ion [44]. Here the conduction band serves as a charge transfer state. The reason of the strong coupling between the dopants and host lattice is the similarity of their electronic states as will be discussed in the following paragraphs.

For trivalent ions, the first excited states are likely to have a $4f^n$ configuration. Due to the screening effect of the 5s5p subshells, the 4f electrons have much less interaction with the host lattice. As a result the energy levels are insensitive to the host lattice and are primarily determined by the Hamiltonian of inner shell electron-electron interaction, i.e. LS coupling. Ce^{3+} however is a special case since only 1 electron is left in the 4f subshell, the ground state is in the $4f^1(^2F_{5/2})$ configuration and the first excited state is in the $5d^1$ configuration. The resulting energy levels are $^2D_{5/2}$ and $^2D_{3/2}$. This is the reason why the Ce^{3+} emission spectrum, just like divalent ions, significantly depends on the host material.

For divalent ions such as Eu^{2+}, the first excited state is $4f^65d$. The 5d electron has strong coupling with the conduction band minimum of the alkaline-earth sulfide lattice like SrS and CaS. The energy level of the first excited state follows the band structure of the host material and results in different emission spectra. As an example, we observed that a $SrS:Eu^{2+}$ EL device emits orange-red light, while a $CaS:Eu^{2+}$ EL device emits deep red light. In contrast, $ZnS:Pr^{3+}$ and $SrS:Pr^{3+}$ have almost identical emission spectra because the excited state for Pr^{3+} is within the 4f subshell and the effects of the crystal field difference are negligible.

From the above discussions, it is not difficult to conclude that transitions between f states are less affected by surrounding perturbation and transitions between d and f states are more dependent upon host material. It is known that for the alkaline-earth sulfide lattice the electrons forming the conduction band are "d-like" [44]. The excited d electrons of the rare earth doping atoms therefore interact strongly with the conduction band of the alkaline-earth sulfide lattice. In addition, f-f transitions are parity forbidden, while d-f transitions are allowed electrical dipole transitions. This characteristic difference can be detected from the emission lifetime of the activators.[45]

There are more comprehensive theories using quantum mechanics and the configuration coordinate diagrams [46], that can give a more complete and more detailed description about the interaction between the optical activators and their surroundings. However, for the experimental results discussed in chapter 6, the theoretical explanation is sufficient within the scope described above.

2.6 Device modeling

ACTFEL device models can be categorized in three distinct classes. The simplest model is the equivalent circuit as shown in Fig. 2.6.1. The breakdown voltage of the Zener diodes is set to match the breakdown voltage of the device being modeled. From this circuit one can see that the phosphor capacitance is shorted during conduction. This model was proposed by Smith [23] and refined by Davidson [39]. Using this kind of circuit model and simulation software like TekSpice one can quantitatively simulate the electrical behavior, although a perfect curve fitting is somewhat difficult.

The next level of model complexity is referred to as the device physics model [23, 47, 48, 49]. All basic device physics and electrostatic equations in description of devices are included at this level. As an example, the tunneling theory in quantum mechanics has been used to model the electron origination. In the tunneling model, the electrons are thought to be tunneling to the conduction band from their interface states by the applied electrical field. The tunneling rate can be calculated as:[23]

$$\psi(\varepsilon, E) = \frac{eE}{4(2m^*\varepsilon)^{1/2}} \exp\left[-\frac{8\pi}{3}\frac{(2m^*)^{1/2}\varepsilon^{3/2}}{ehE}\right] \qquad \text{eq. (2.6.1)}$$

where ε is energy, E is the electric field in the phosphor, m^* ($m^* = 0.3\ m_e$ for ZnS) is the effective electron mass, and h is the Planck's constant.

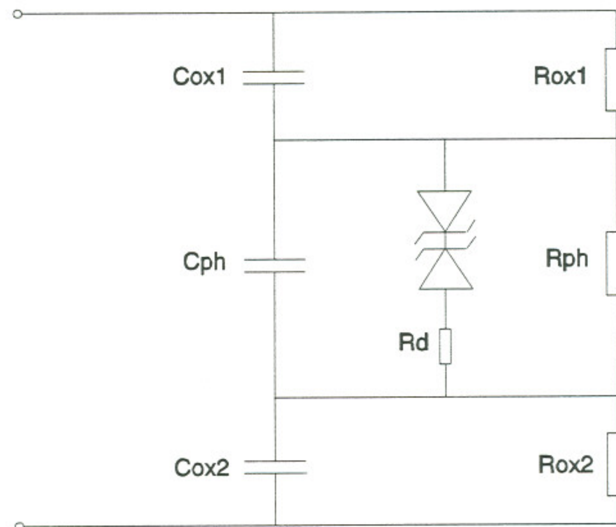

Fig. 2.6.1 Equivalent circuit of a TFEL device.

The highest level of modeling is Monte Carlo simulation. Currently, this form of device modeling is only concerned with the bulk properties of ZnS. Monte Carlo modeling simulates electron trajectories and scattering events as the electron moves under the influence of an electrical field. Scattering rates for all relevant physical phenomena which affect electron energy and momentum must be considered. Bhattacharyya et al. [26] have included polar optical phonon, acoustic phonon, intervalley scattering, ionized impurity, and neutral impurity scattering rates in their modeling. Additionally, one must describe the Brillouin zone. This is often approximated with parabolic conduction band minima or via a detailed band structure calculation [28]. Generally speaking, an accurate Monte Carlo

simulation depends on many material parameters; however many of those parameters are not known accurately.

So far in this chapter, the basics of electoluminescence and ACTFEL devices have been briefly reviewed. The device operation is very complicated and is still far from being fully understood. The intention of this thesis work is to add a bit more knowledge and understanding of electroluminescence mechanisms .

Chapter 3
Atomic Layer Epitaxy

3.1 History

In the early 1970's there was a need for a new technique to fabricate high quality thin films for EL display devices. Uniform ZnS thin films and pinhole free Al_2O_3 insulating films were needed. The atomic layer epitaxy (ALE) method was then developed to grow polycrystalline ZnS films on glass substrates from elemental zinc and sulfur and later from $ZnCl_2$ and H_2S compounds. The ALE method was first described in a US patent of Finnish origin filed in late 1975 and granted in 1977 [50]. Indeed, the first experiment was performed in 1974 by Suntola and Antson on a modified vacuum evaporator. In 1980, the company responsible for the patent, Lohja Co., developed the technique to make commercial electroluminescent displays based on ZnS:Mn [51] and in 1982 was awarded a prize by SID for the greatest advance in the display field. Following the initial success on growing ZnS thin film, the ALE method has been used for other material systems including GaAs, GaP, CdTe, ZnSe, etc.[52, 54]

3.2 Mechanisms of ALE

Atomic layer epitaxy can be briefly described as a deposition technique where the source materials are alternatively pulsed into a reactor chamber in the vapor phase. During each pulsing period, the chamber contains an excess of reactant in the vapor phase. By

keeping the substrates within a certain temperature range it is possible to grow one monolayer on the substrate's surface at one pulse. The excess reactant is purged out by a following pulse of inert gas. The second reactant is then introduced into the reactor and a monolayer of reactant is grown on the previously deposited monolayer. If the reactants are compounds they undergo chemical reactions on the surface of the substrates. After the reaction, the desired compound is deposited and the gas phase by-product is carried out by the purging gas pulse. By repeating the reaction cycles a controlled monolayer by monolayer growth is achieved.

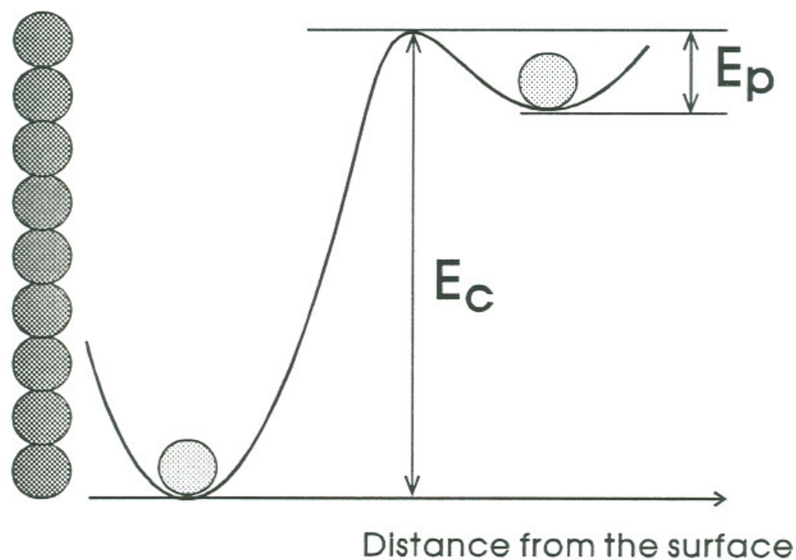

Fig 3.2.1 Energy diagram comparing chemical and physical adsorption.

The mechanism of the ALE process is based on the energy difference between chemical adsorption and physical adsorption on the surface of a substrate. When a flux of reactive molecular compounds or elemental atoms reach the surface of substrate, the first layer interacts strongly with the surface to form a chemical bond, i.e., chemical adsorption. The subsequent layers are much more weakly bonded so that only physical adsorption occurs. These two kinds of surface reactions can be distinguished by the different activation energies, E_c and E_p as shown in Fig 3.2.1., where E_c and E_p are the activation energies of chemical adsorption and physical adsorption [53], respectively. Here we can define a discrimination factor η as:

$$\eta = \exp(\frac{E_c}{E_p}).$$

To utilize the ALE technique, it is desirable to have a large discrimination factor η so that one can control the surface reaction more easily. When η is large enough, one can heat the substrate to a sufficiently high temperature so that $E_p < kT$ while keeping $E_c >> kT$. Here k is the Boltzmann constant. In this case only the chemically adsorbed layer remains attached and the excess reactants can be purged out. The suitable temperature range required to ensure a controlled ALE growth, the so-called ALE temperature window, has been studied by Suntola [54]. As shown in Fig. 3.2.2, the temperature window indicates the temperature range where monolayer growth can occur.

Operating the ALE process below the lower limit of the window temperature can give rise to the following problems:

(L1) Condensation, which includes condensation of all the reactants and their by-products, condensation can result in a higher but uncontrolled growth rate.

(L2) Incomplete reaction, which means extra energy is needed to overcome the activation energy needed to form chemisorption.

Operating the ALE process above the upper limit of the window temperature, another set of problems can arise including the following:

(H1) An undesirable decomposition of reactant condensed on the substrate. This is typical when a large molecular metal organic compound is used as reactant.

(H2) Re-evaporation of formed monolayers.

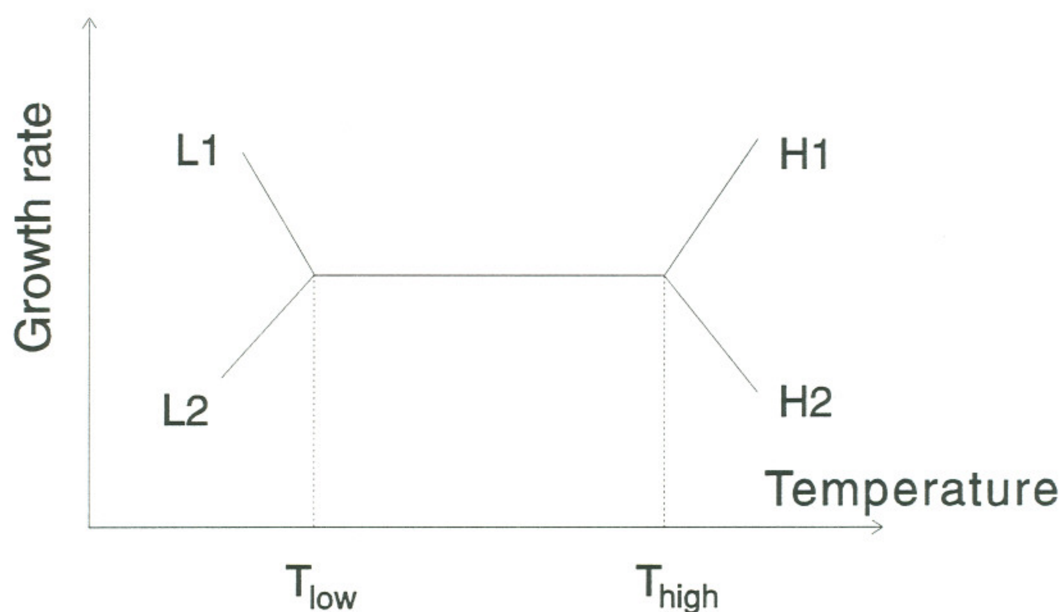

Fig. 3.2.2 Processing temperature window ($T_{low} < T < T_{high}$) for atomic layer epitaxy process, where L_1: condensation; L_2: Incomplete reaction; H_1: Undesirable decomposition; H_2: re-evaporation of formed monolayers.

Between these two limits, monolayer by monolayer ALE growth can occur. In an ideal case the growth rate should be independent of temperature.

For example, in the ZnS thin film growth process with elemental zinc and sulfur, initially the chemically adsorbed zinc atoms form the first saturated monolayer. The excess Zn atoms will be physisorbed and carried out by an inert purging gas pulse such as N_2. In the next phase, a flux of sulfur atoms comes in, but again only one monolayer of chemically adsorbed sulfur can stay on the surface to form Zn-S bonds; the rest of sulfur atoms will be carried out by N_2. This can be repeated many times with the thickness of the ALE grown thin films determined solely by the number of cycles. There is a major characteristic difference between ALE and CVD growth; ALE only allows one of the two source gases to reach the surface at a time so it only grows one atomic layer at a time. In CVD both source gases approach the surface simultaneously, hence the growth rate is determined by the substrate temperature and the amount of gas available.

Atomic layer epitaxy is a relative new and generally poorly understood thin film growth technique which is likely to find applications in high tech industries in the future. An ALE reactor that can handle 8 inch substrates has been shown during MRS Boston, 1994 fall by Microchemistry Ltd. ALE can be used to grow high quality thin films with specific crystal structure or orientations and with very fine control of film thickness to one atomic layer. Most thin film deposition technologies have, so far, simply involved material transfer from a suitable source to a suitable substrate via the vapor phase, e.g. vacuum evaporation, sputtering, or CVD. When nucleation takes place on the substrate surface, the molecules seek the most energetically favorable position relative to one another and form micro-crystals that in later phases control thin film growth. This results in uncontrolled crystal boundaries, producing poly-crystalline films whose average density

can be considerably below that of the corresponding bulk crystal. Usually annealing is employed to improve the quality of the deposited film. In ALE the compound thin film immediately achieves its final crystal form through sequential surface reactions in which one element of the compound reacts with the growing surface. This method is a self-controlled process that automatically accepts only one atomic layer at a time.

This chapter has been a review of the fundamentals of Atomic Layer Epitaxy, its development history, its operation mechanisms and its advantage over other thin film deposition techniques. This basic understanding of ALE served as a guide during the device fabrication which will be addressed in the next chapter.

Chapter 4
Thin Film Synthesis by ALE and Initial Characterization

In this chapter, the structure and the operational mechanism of the ALE reactor are described. The reactor was used to grow primarily Al_2O_3, ZnS and SrS thin films. The process conditions for growing these thin films on ITO coated glass substrates are presented. Atomic force microscope and grazing incident X-ray diffraction were employed to characterize the structures of these thin films.

4.1 Introduction of the F-120 ALE reactor

The F-120 ALE reactor was designed and manufactured by the Finnish company Microchemistry Ltd. headed by the inventor of ALE technology Dr. Suntola [50]. The design of the F-120 reactor was targeted at fulfilling the demand of research and development labs working on EL displays, where the capability of handling large quantities of substrates and large substrate size is not required. The schematic diagram of the substrate holder in the F-120 is shown in Fig 4.1.1, where two 50 mm x 50 mm x 1mm glass substrates are held face to face in a quartz substrate holder, and between the two substrates there is a quartz spacer so that reactant gases can flow.

The schematic of the gas handling system of F-120 reactor is shown in Fig. 4.1.2. There are a total of six source ports, four (#1, 2, 4, 5) are for solid source materials (usually powders), the other two, ports #3 and #6 are for gas (H_2S) or liquid vapor (H_2O or $[CH_3]_3COH$) sources. The solid source material is normally held in a glass boat with an

external thermo-couple attached to it for its temperature control. It is necessary to control the solid source temperature so that a desired vapor pressure can be achieved. The tubing and valving of the F-120 are fairly complicated. Each port consists of an inner glass tube and an outer glass tube as shown in Fig. 4.1.2. In the "off" state, i.e. at the moment the vapor is not needed in the reaction chamber, valve A is closed and only N_2 can flow in the outer tube and then is split going either to the substrate or along direction BDE (see Fig. 4.1.2) to carry the undesired vapor to exhaust. When the vapor is needed, valve A opens, N_2 now is divided to flow in both inner and outer tubes but mostly through the inner tube. Source vapor flows in direction DBC to the substrate holder.

The heating coils used for temperature control increases in temperature in the direction toward the substrate holder. In other words, the source which needs the highest temperature is put closest to the substrates and the source with the lowest temperature is put farthest away from the substrates. The obvious advantage of this temperature distribution is that gases traveling toward the substrates travel through regions of increasing temperature, reducing or eliminating the possibility of condensation on the gas tube wall.

Although there is only one designated heater for each source boat and thermocouple, the temperature setting for each solid source will be affected by neighboring heaters. This is due to the fact that two neighboring heaters are not well thermally insulated. When one heater is heated up, the neighbor will follow to a certain minimum value. This weakness can limit the choice of source materials.

A Compaq 386-PC computer allows the user of the F-120 reactor to program the temperature settings, N_2 flow rate, and pulsing sequence. Multilayer growth and doping can be conveniently achieved via programming the proper pulsing sequence.

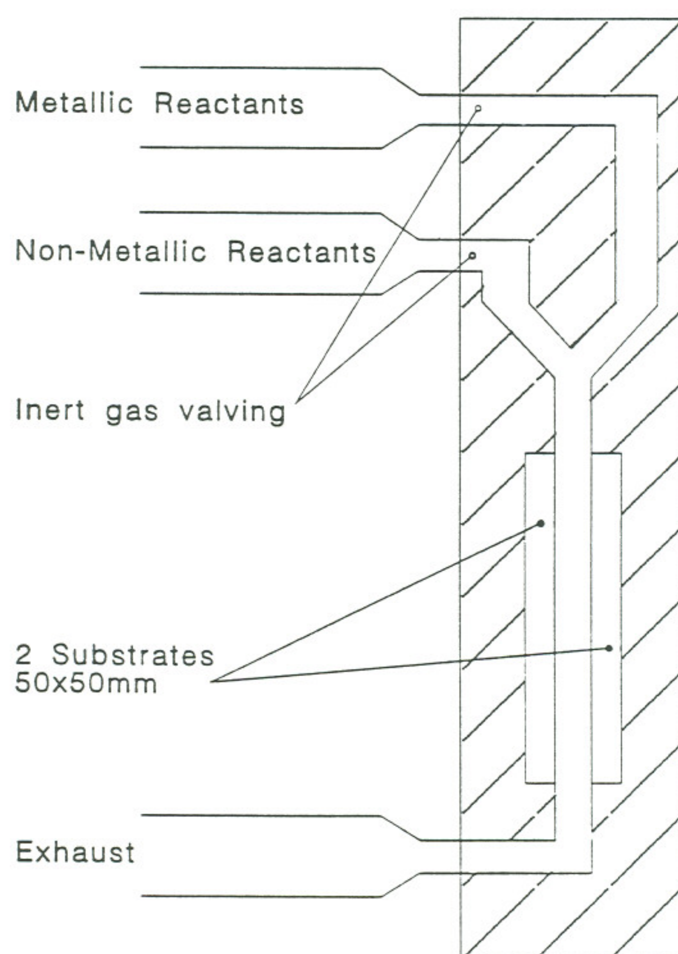

Fig. 4.1.1 Schematic diagram of F-120 substrate holder.

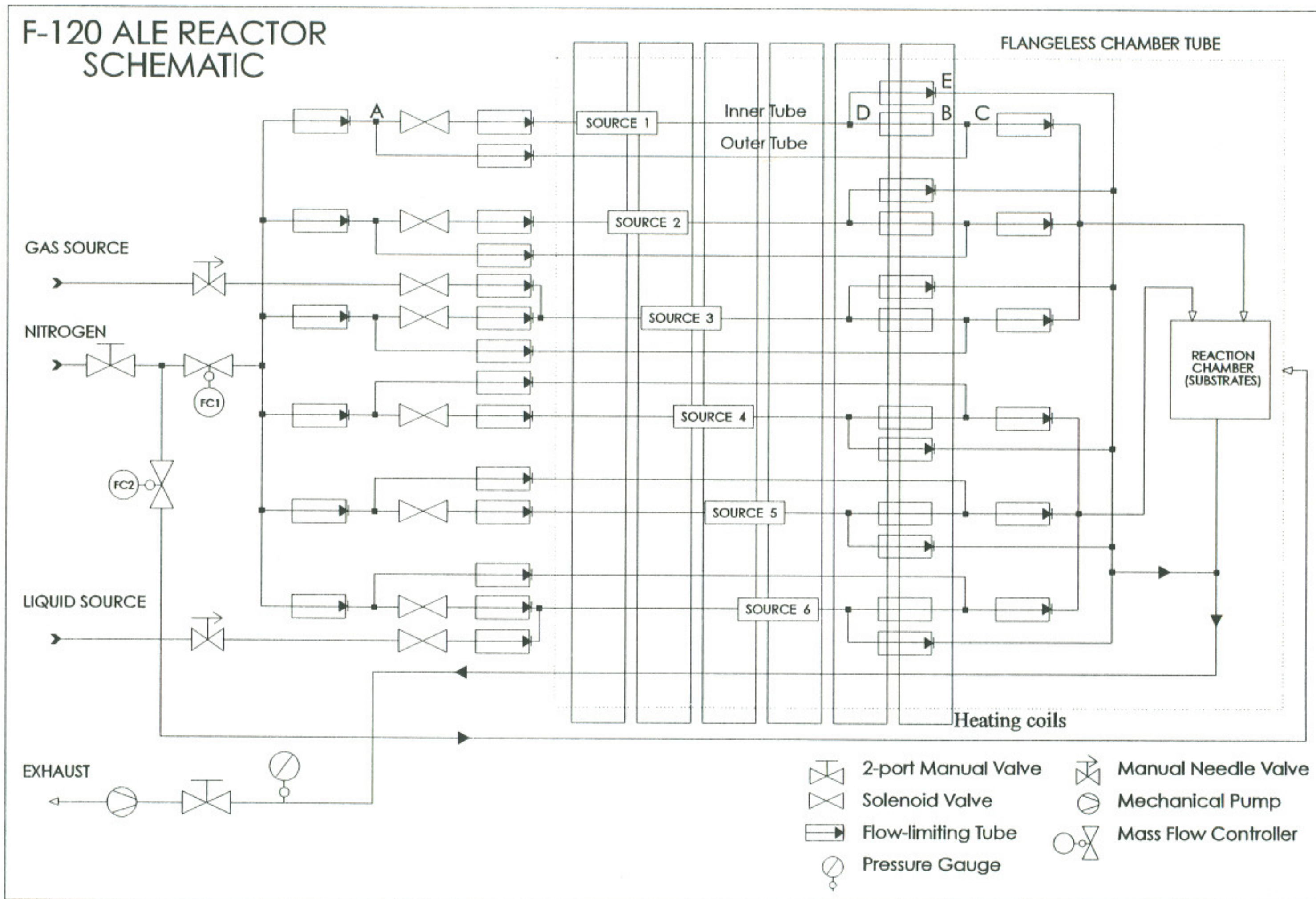

Fig. 4.1.2 F-120 ALE reactor system schematic.

4.2 Synthesis of Al2O3 by ALE

Aluminum oxide is regarded as an excellent electrical insulator. Single crystal Al_2O_3 (sapphire) has been widely used as substrate material for epitaxial growth of a variety of semiconductor thin films. Amorphous Al_2O_3 thin film can be conveniently prepared by ALE as the insulating thin film for application in TFEL flat panel displays. When growing Al_2O_3 via ALE, two pairs of compounds have been utilized as the source materials: $AlCl_3 + H_2O$ or $AlCl_3 + (CH_3)_3COH$ (2-methyl-2-propanol, also known as tert-butyl alcohol). Aluminum chloride has been used as the metallic source material while water or 2-methyl-2-propanol has been used as the oxidant source. $AlCl_3$ takes a solid form at room temperature, and when heated up to 80 °C ~ 100 °C, has a fairly high vapor pressure (80 Pa ~ 160 Pa). Water and 2-methyl-2-propanol are liquid and have reasonably high vapor pressures at room temperature. The vapor pressure for 2-methyl-2-propanol alcohol varies between 1210 Pa and 6690 Pa at between 5 °C and 30 °C. In order to control the process precisely, the water bath was kept at 19 °C and 2-methyl-2-propanol was kept at 27 °C. To grow Al_2O_3, 2-methyl-2-propanol vapor (or H_2O vapor) and $AlCl_3$ vapors were pulsed alternatively as shown in Fig 4.2.1. Both these vapors were transported by N_2. Between H_2O and $AlCl_3$ pulses there was a 0.4 s ~ 0.6 s pulse of dry N_2 as purging gas. The effect of N_2 pulses is to clean the reaction surface so that the excess gas molecules will be carried out, while the chemically bonded aluminum oxide remains. The chemistry on a surface exposed to H_2O and $AlCl_3$ leads to the formation of HCl and Al_2O_3. This is a chemically favored reaction since HCl is volatile and will be pumped out while Al_2O_3 is very stable. However the chemistry between 2-methyl-2-propanol and $AlCl_3$ is not very clear. It has been shown that both OH radical and chlorine

exist in the Al_2O_3 layer made from 2-methyl-2-propanol and $AlCl_3$ [55]. The advantage of using 2-methyl-2-propanol instead of water is to avoid excess water vapor in the system, especially after growing a SrS thin film, which absorbs water very fast.

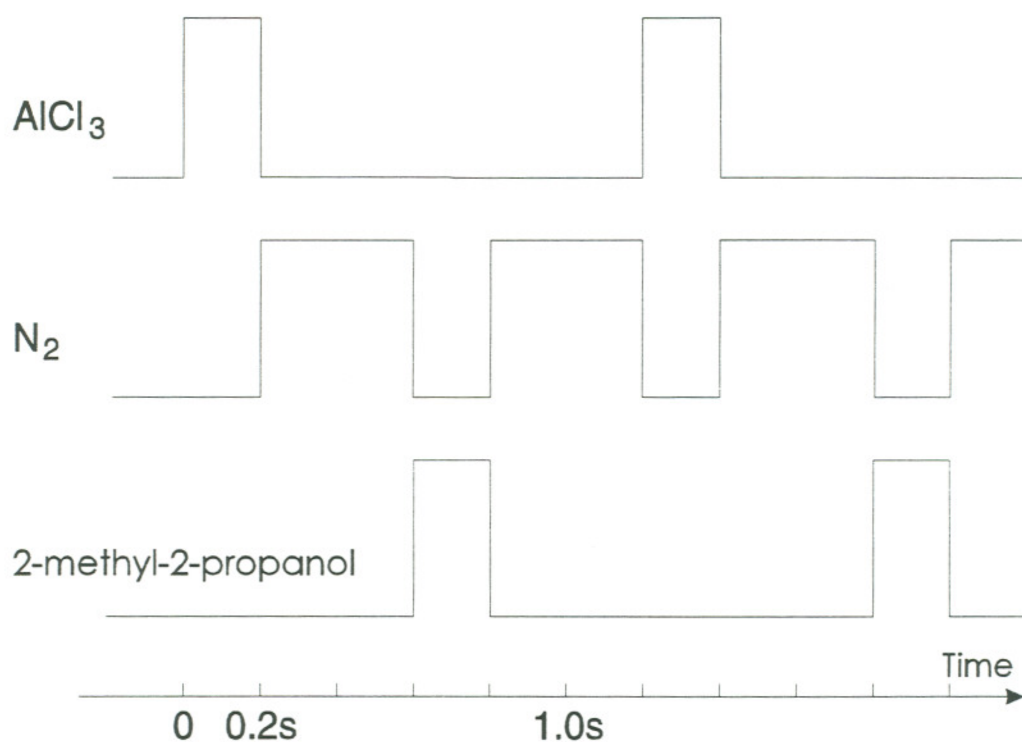

Fig. 4.2.1 Reactant gas pulse sequence in the ALE process.

The dependence of growth rate of Al_2O_3 on temperature has been studied for the $AlCl_3$ / 2-methyl-2-propanol process. As shown in Fig. 4.2.2., the growth rate decreases with an increase of glass substrate temperature. This suggests that an exothermic reaction controls the growth rate of Al_2O_3 thin film. The activation energy of the reaction can be estimated from the slope of the plot in Fig. 4.2.2. This is estimated to be about 9.7 kJ/mol.

which is twice that of the reported data for the same process [55] but smaller than the reported activation energy (16 kJ/mol) of the process using water [56] instead of 2-methyl-2-propanol.

In an effort to determine the dielectric constant $\varepsilon(0)$ of aluminum oxide, parallel plate capacitors were made by depositing aluminum thin film dots on aluminum oxide grown on ITO. The dielectric constant was determined from the thickness (via DekTak profilometer) and the capacitance measurement. The measured dielectric constant for our ALE prepared aluminum oxide thin film is 12.3±10%.

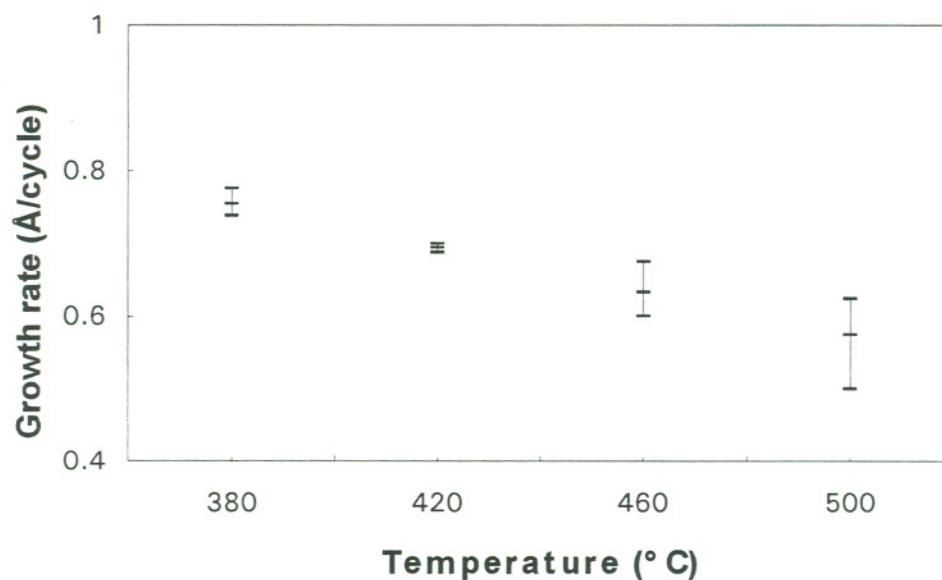

Fig. 4.2.2 Growth rate vs. substrate temperature of Al_2O_3 ALE thin films grown on glass by $AlCl_3$ and $(CH_3)_3COH$.

X-ray diffraction analysis was performed for all the thin films grown including aluminum oxide, zinc sulfide, strontium sulfide and strontium chloride. More detailed discussion about the X-ray diffraction characterization of the thin films will be presented later in section 4.5. It is evident from the X-ray diffraction data that the aluminum oxide thin films grown by our ALE reactor are indeed amorphous.

4.3 Synthesis of ZnS by ALE

Thin film ZnS can be deposited by many different techniques, including sputtering, atomic layer epitaxy, and metal-organic chemical vapor deposition. In the EL flat panel display business, ALE has been used as one of the primary methods to make ZnS:Mn displays since the very beginning of its commercialization. The time required for the ALE growth process is fairly long. Since an industrial ALE machine can handle tens of large panels in a run, a reasonable throughput has been achieved.

ZnS thin films are typically grown on top of amorphous Al_2O_3 (or Aluminum-Titanium-Oxide). Because there is no ordered crystalline phase to grow on, the initial surface reaction is complex. This complexity has the effect of reducing the growth rate (about 1 Å/cycle) to less than 30% of the expected rate, which means the ALE growth takes three cycles or more to grow a monolayer instead of one monolayer per cycle. A great deal of work has been done to investigate the mechanism governing the growth rate, grain size and preferred growth orientation. There are a few models to describe the initial formation of ZnS layers on an amorphous substrate [58]. In general the surface reaction mechanism varies from process to process. It is necessary in this work to understand the basic properties of our ZnS thin film growth by the F-120 reactor. In this section, thin film

ZnS properties including growth rate, thin film non-uniformity, dielectric constant, and the temperature dependence of growth rate are explored. Atomic force microscopy (AFM) was used to study the surface roughness. A grazing incident angle x-ray diffraction analysis has been performed and will be presented in section 4.5

To grow ZnS, $ZnCl_2$ and H_2S are used as metallic and non-metallic compound source materials, respectively. The melting point of $ZnCl_2$ is about 330 °C. The $ZnCl_2$ was normally heated in a glass boat to 335~340 °C. Electronic grade H_2S was used for this investigation. At room temperature, the H_2S cylinder has pressure of ~300 psi so that a gas regulator must be used to reduce the pressure down to about 13 psi. A needle valve was used to further control the flow rate of H_2S to 5.0 sccm, as shown in Fig. 4.1.2. The pulsing sequence for growing ZnS is similar to Fig. 4.2.1.

ZnS EL devices were doped with two rare earth elements, Tb and Pr. The precursors for these two dopants were $Tb(thd)_3$ and $Pr(thd)_3$, where thd = 2, 2, 6, 6-tetramethyl-3,5-heptanedione. The melting point for the two compounds is about 160 °C. It was usually heated to 155-158 °C to give a reasonable vapor pressure (accurate vapor pressure is not known). The doping pulse was introduced in the growth process, i.e., one doping pulse was allowed for every ten to fifty $ZnCl_2$ and H_2S pulses. Because the dopant atoms have their own incorporation rate into the host, the exact doping concentration must be calibrated by other direct tests like secondary ion mass spectroscopy (SIMS).

In an effort to determine the temperature dependence of ZnS thin film growth, four sets of two substrates, each set consisting of one blank glass substrate and one ITO coated glass substrate were used to grow ZnS at 380 °C, 420 °C, 460 °C, and 500 °C respectively. The purpose of using glass substrates is to get a clean x-ray diffraction pattern once growth has finished, eliminating any underlying ITO peaks which may

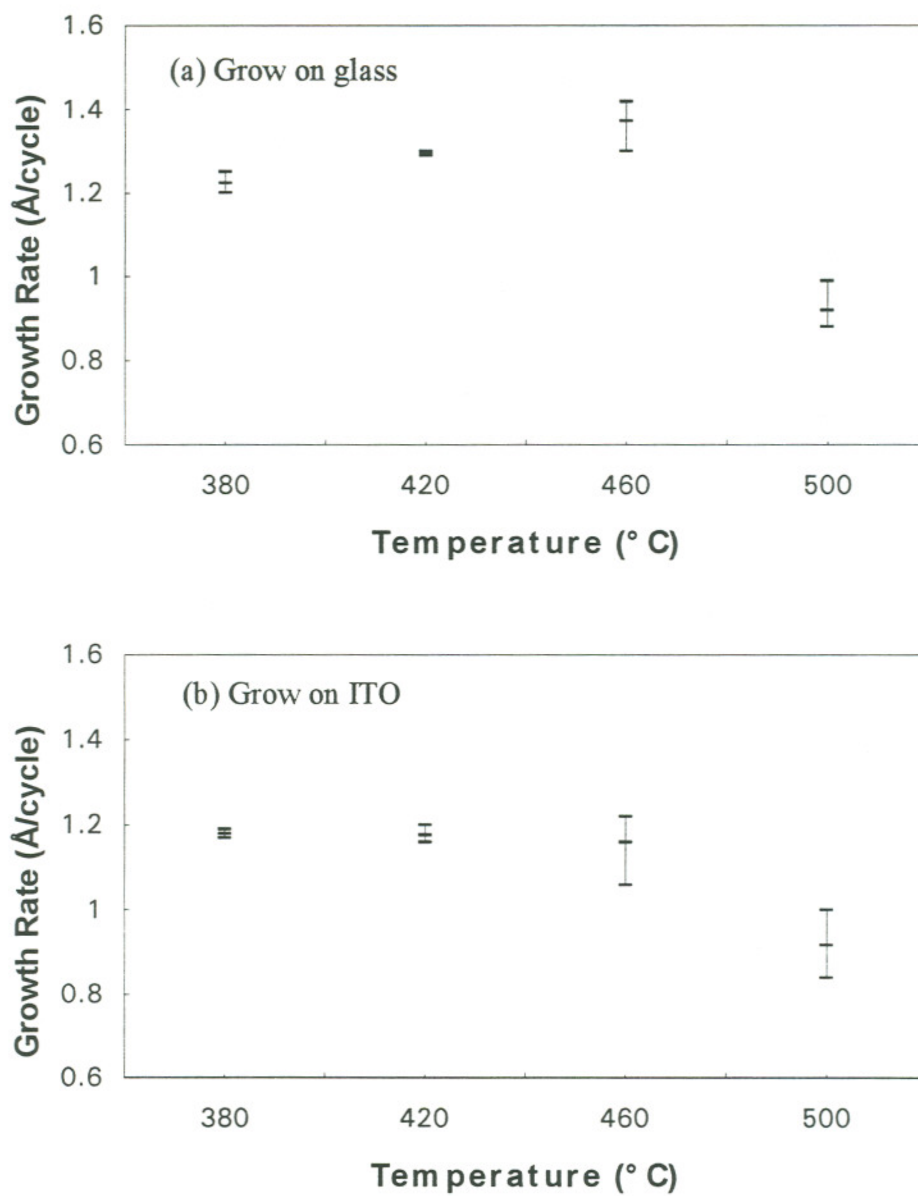

Fig. 4.3.1 Temperature dependence of ZnS growth rate.

interfere with analysis. Growth of ZnS on ITO directly allows capacitors be made from the ZnS film. The ITO layer and a layer of later evaporated aluminum can serve as the two electrodes. In Fig. 4.3.1, the growth rate is shown in terms of Å/cycle. The growth rate variation with the temperature is much less than the variation in a CVD growth [57]. However it is not constant in the studied temperature range from 380 °C to 500 °C. From the discussion in Chapter 3, it is known that there are four factors contributing to the growth rate variation, i.e., condensation and incomplete reaction at the low temperature, undesired decomposition of the source molecule and re-evaporation of formed layers at the high temperature. Condensation and undesired decomposition will lead to higher growth rate while incomplete reaction and re-evaporation will lead to lower growth rate. From Fig 4.3.1, one can postulate that incomplete reaction is attributed to the lower growth rate at low temperature, and re-evaporation attributed to the lower growth rate at high temperature. However, the real situation is always more complicated. It is believed that some kind of CVD type reaction exists at high temperature. The reason is that when two reactant gas pulses alternate, there could be some mixture of two gases in the gas inlet line. This situation has analogy to Low Pressure CVD (LPCVD) (the pressure in the reaction chamber is about 3 mBar). In the case of LPCVD, the growth rate is surface reaction limited, i.e., the growth rate is sensitive to the substrate temperature so that when the substrate temperature is high, the reaction rate is high and the local depletion of reactants could happen, and this could lead to film non-uniformity. People have observed a higher deposition rate on wafers located close to the inlet gas line in LPCVD systems operated at a high temperature [57]. It was known to the designer of the F-120 that there could be a thicker deposition along the section of gas inlet line between the substrate and

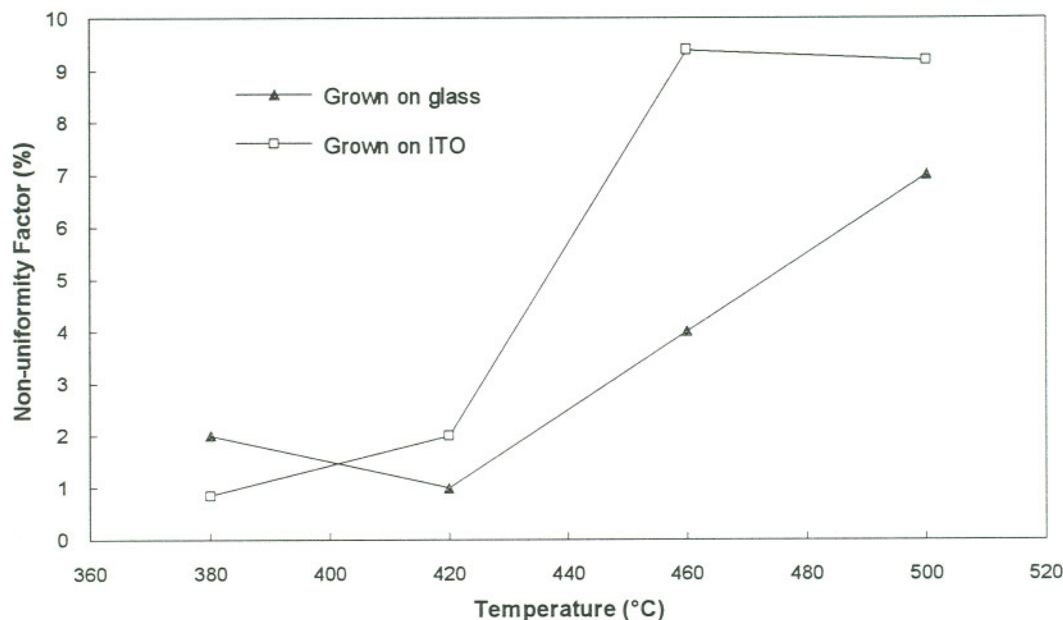

Fig 4.3.2 Non-uniformity factor vs. temperature for ZnS grown on glass and ITO.

the point where two gas lines meet (refer to Fig. 4.1.1, in the small section right on top of the substrates). The non-uniformity plot in Fig. 4.3.2 supports the above discussion, where the non-uniformity factor is defined as $(d_{max}-d_{min})/2d_{ave} \times 100\%$, where d is the thickness of the film measured by profiling an etched mesa with a DekTak profilometer (for each sample, 3 mesas were made at top, middle and bottom of the 50 mm square sample). At high growth temperature of 500 °C, the film is thicker along the side where reactant gas flows in, and it can be regarded as an extension of the CVD type deposition originating from the gas line.

The dielectric constant of thin film ZnS is a parameter of interest. The electric field in the ZnS layer and the charge transferred across it in a TFEL device can be calculated only when the dielectric constant is known. Knowing the device area and parallel plate

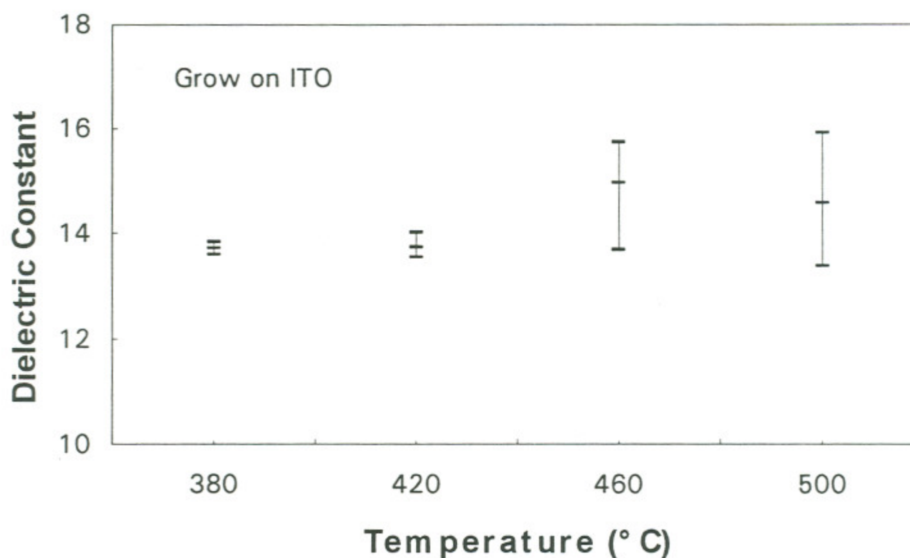

Fig. 4.3.3 Dielectric constant variation of ZnS grown at different temperatures.

capacitor's definition, the dielectric constant was determined by measuring the capacitance of an ITO-ZnS-Al parallel plate capacitor, and the thickness of ZnS film. Fig. 4.3.3 shows the dielectric constant variation vs. temperature, where it varies between 13.5 and 15. Depending on the cubic or hexagonal phase and orientation, the dielectric constant can vary from 8.7 to 16 for single crystal ZnS [59]. It is expected that the dielectric constant of a polycrystalline ZnS film consisting of two possible phases falls in between 8.7 and 16. The growth temperature variation of the dielectric constant could result from two reasons: (i) change of phases or change of the ratio of the two phases, i.e. cubic or hexagonal

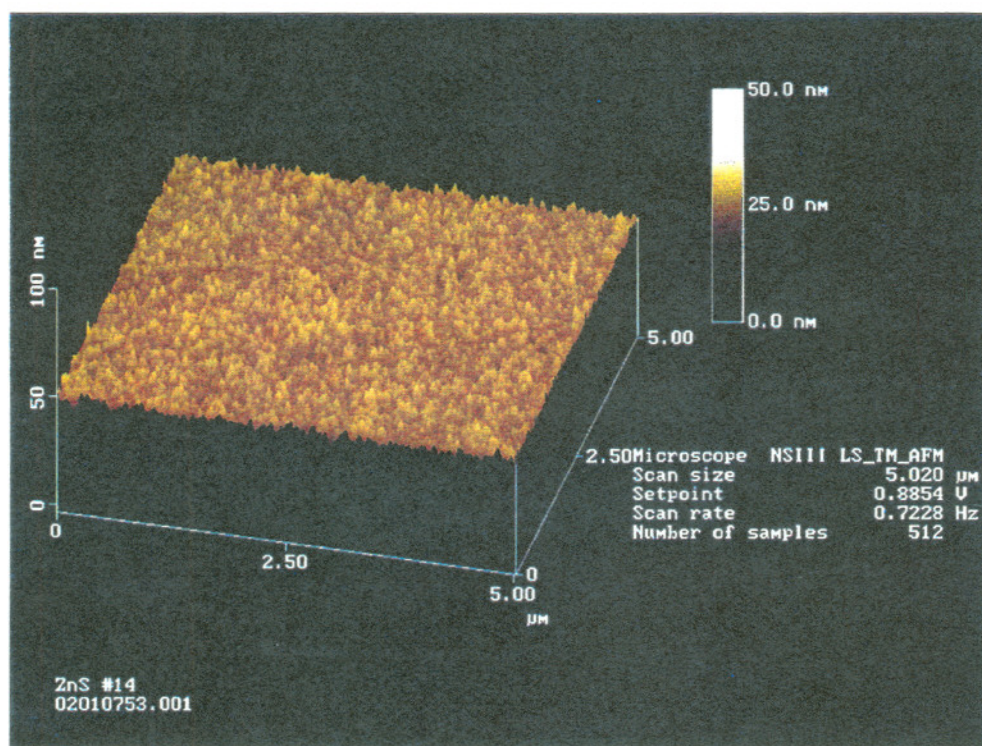

Fig 4.3.4a. AFM image of sample #14, grown on Al_2O_3 at 500 °C for 400 cycles (thickness≈360 Å).

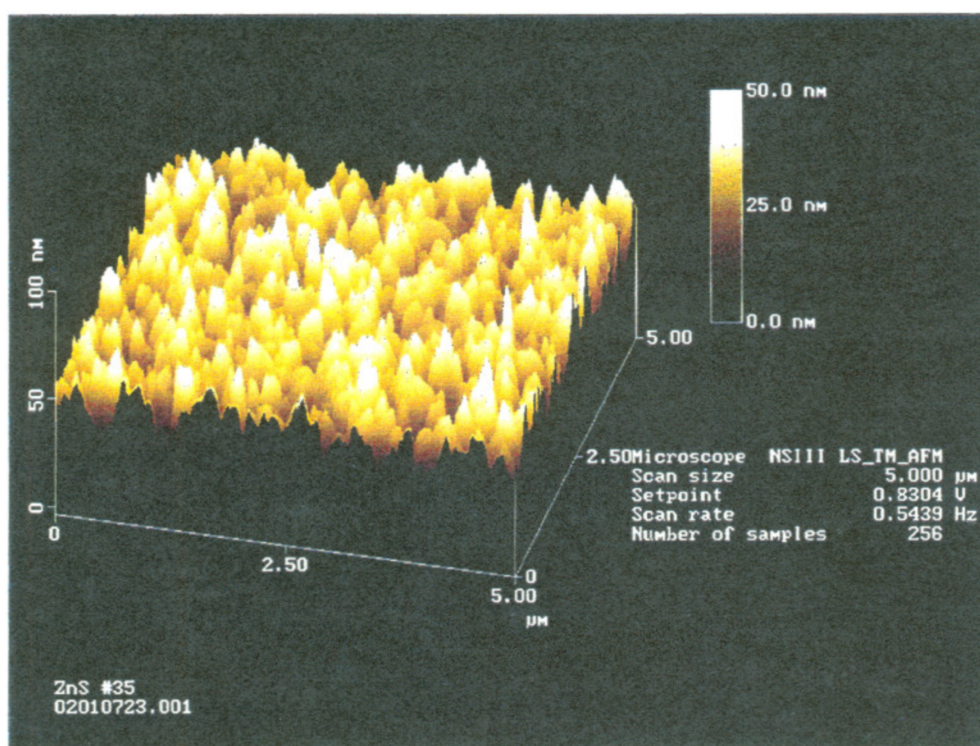

Fig 4.3.4b. AFM image of sample #35, grown on Al_2O_3 at 500 °C for 6000 cycles (thickness≈5400 Å).

phase; (ii) change of the preferred orientation. More detailed discussion of these two issues will be conducted in section 4.5 where the X-ray diffraction data is presented.

Two ZnS thin film samples were made for an atomic force microscopy (AFM) study conducted at Intel Corp. Both samples were grown on Al_2O_3 at 500 °C. Sample #14 was grown for 400 cycles, which led to a thickness of about 360 Å; Sample #35 was grown for 6000 cycles, which led to a thickness of about 5400 Å. Fig 4.3.4a and Fig. 4.3.4b show the AFM images of sample #14 and #35 respectively. The measured average grain size for sample #14 is 80 nm, and that for sample #35 is 250 nm. This grain growing phenomenon has been reported by other authors [58, 60].

4.4 Synthesis of SrS by ALE

Although ZnS:Mn based EL displays have been successfully commercialized for more than ten years, the products do not meet the full color display requirement. A variety of rare earth elements, like Ce and Eu, are good candidates as optical centers in a host matrix. However in most cases, rare earth elements doped ZnS EL devices can not deliver the required power efficiency and stability. One of the reasons is that the host lattice can easily be destroyed by the dopants that are too large to substitute in the zinc atom sites. Strontium has an atomic radius closer to the rare earth elements, and SrS is a wide band gap semiconductor (4.3 eV) which is essential for high field EL devices. SrS has been regarded as a promising alternative host for achieving blue and red color EL when doped with Ce and Eu, respectively. The common methods for SrS thin film deposition are electron beam evaporation [61] and sputtering [62]. Atomic layer epitaxy has also been

used by researchers in Finland to grow SrS thin film EL devices [63, 64]. One of the objectives of this work was to explore the growth of SrS by ALE.

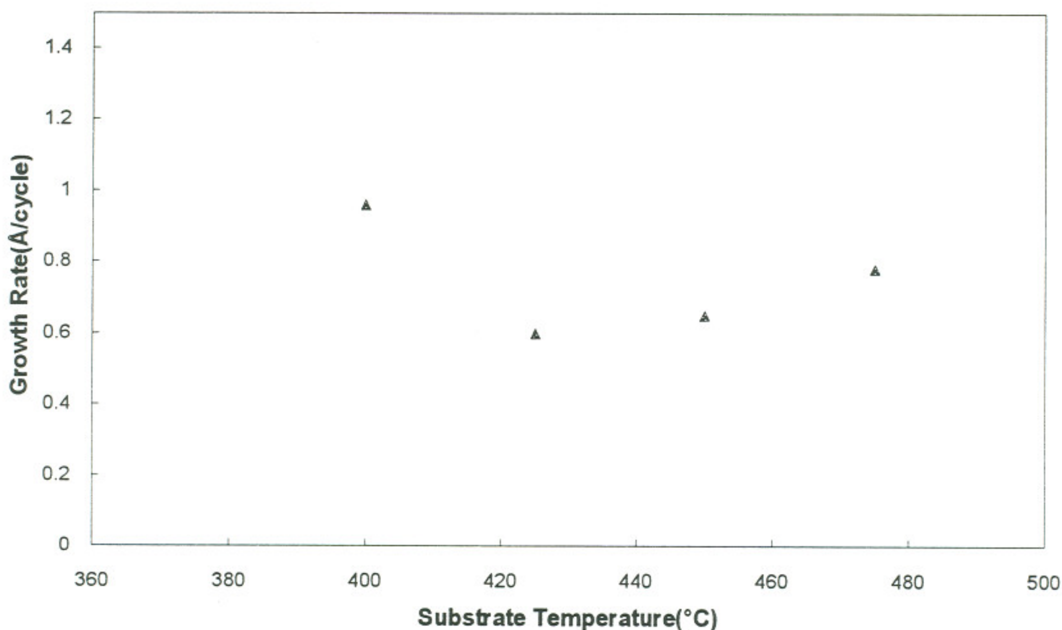

Fig. 4.4.1 Temperature dependence of SrS growth rate grown on glass substrate.

Unlike ZnS thin films which are stable in air, SrS thin films can easily be oxidized by moisture and air. These intrinsic properties demand a more rigid process control. The source materials for growing SrS were H_2S and $Sr(thd)_2$ (supplied by Strem Chemicals, thd = 2, 2, 6, 6-tetramethyl-3,5-heptanedione) which is subject to oxidization when exposed to air. The $Sr(thd)_2$ source temperature was normally between 220 and 230 °C. Due to the impurities in the source compound, the melting temperature was found to be unstable. The precursor varied from batch to batch. This variation made it difficult to control the growth in a repeatable manner. The flow rate for H_2S was set at 15.0 sccm by

a needle valve. A large H_2S flow rate is preferred to saturate the surface with sulfur. The pulse duration for $Sr(thd)_2$ and H_2S were 0.2 and 0.3 second, with 0.6~0.8 sec N_2 purging time respectively [65]. Fig. 4.4.1 shows the dependence of the growth rate on the substrate temperature. It was found that $Sr(thd)_2$ decomposed before reaching the substrates. This is known from the darkening walls along the $Sr(thd)_2$ source tube and inlet line during growth. The higher the substrate temperature, the darker the walls appeared. The decomposition and impurity of $Sr(thd)_2$ complicated the growth mechanism. As a result, the repeatability for growing SrS has been poor. Still devices are made of SrS thin films.

In Fig 6.2.4, an X-ray diffraction pattern for SrS thin film is shown. The strongest peak is (002) of sodium chloride-like cubic structure and it suggests that there is a slight preferred growth orientation. More discussions about its optical performance will be presented in Chapter 6.

4.5 Structure characterization by grazing incident angle X-ray diffraction

In order to get higher peak intensities, the X-ray diffraction method used was the grazing incident angle method, instead of the conventional θ-2θ scan method [66]. In the later case the X-ray can easily penetrate through the thin film and the detector will not detect a high enough count. In the grazing incident angle method, the incident X-ray makes a small angle of incidence (1-3°) with the film, and much stronger X-ray diffraction pattern from the top layer of the thin films can be easily obtained by scanning the detector along the 2θ circle of a diffractometer.

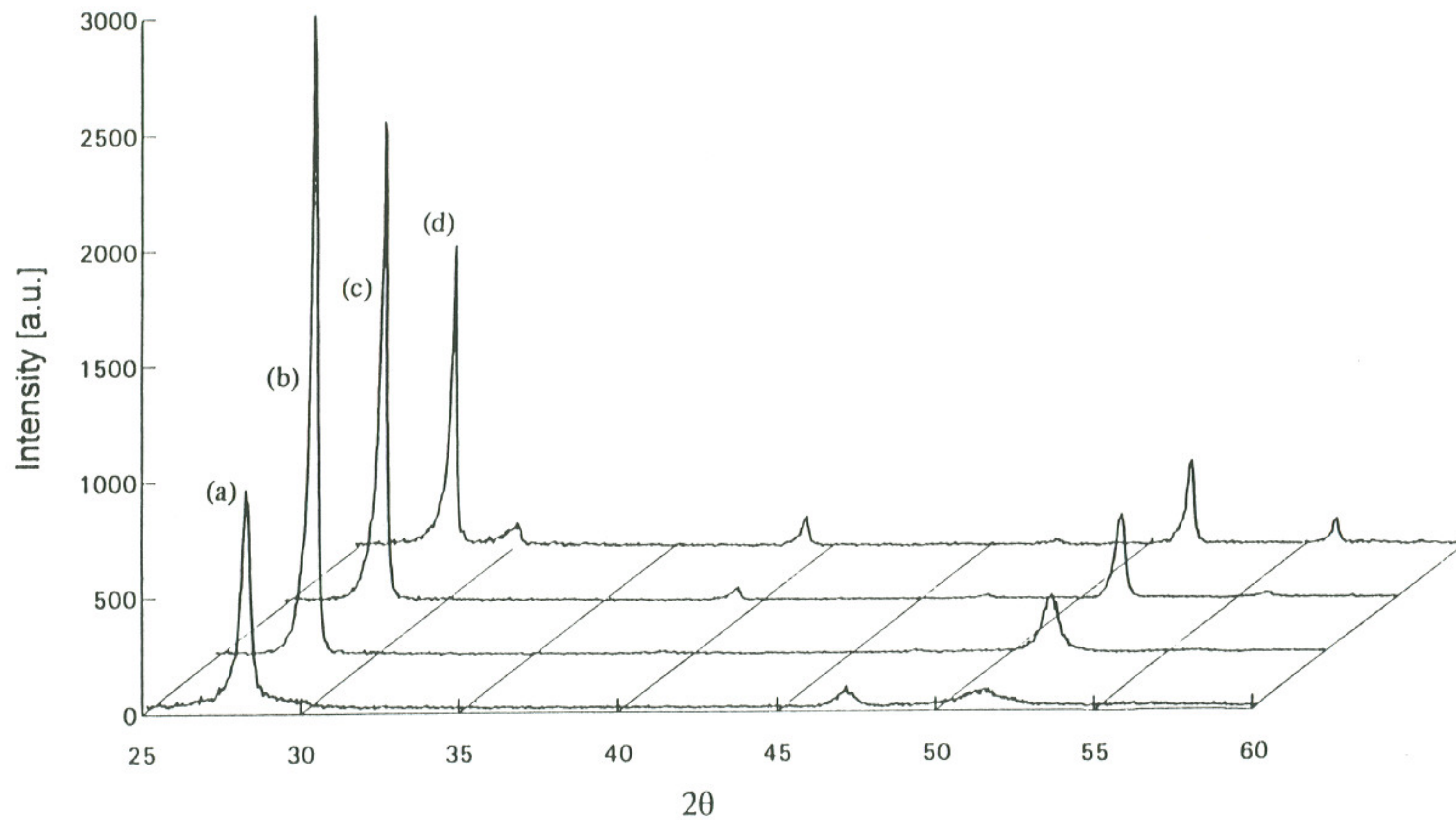

Fig. 4.5.1 X-ray diffraction patterns of ZnS thin films grown on glass substrates at various temperatures:

(a) 380 °C, (b) 420 °C, (c) 460 °C, (d) 500 °C.

Fig. 4.5.1 shows the X-ray diffraction patterns of the ZnS thin films grown on glass substrates at various temperatures: (a) 380 °C, (b) 420 °C, (c) 460 °C, (d) 500 °C. The incident X-ray wavelength of Cu-Kα1 line is 1.541Å. The spacing between adjacent diffraction planes, d can be calculated using equation $d = \lambda/(2\sin\theta)$. The d values of the observed peaks are listed in Table I along with the d values of standard cubic and hexagonal peaks of ZnS from JCPDS cards.

Table I. Diffraction peaks of ZnS grown on glass at various temperatures

	d Values (crystal plane spacing) of the Diffraction Peaks (Å)					
	Experiment results				JCPDS cards	
Peak #	380 °C	420 °C	460 °C	500 °C	Cubic	Hexagonal 2H
0	-	-	-	-		3.310 (100)*
1	3.128	3.131	3.131	3.134	3.123 (111)*	3.129 (002)*
2	-	-	-	2.934		2.926 (101)*
3	-	-	2.277	2.279		2.273 (102)*
4	1.919	1.917	1.916	1.914	1.912 (220)*	1.910 (110)*
5	1.765	1.770	1.769	1.768		1.764 (103)*
6	-	-	1.634	1.634		1.630 (112)*

* The values included in the parentheses are the orientations from the JCPDS (Joint Committee of Powder Diffraction Standard) cards.

It can be seen from Table I that the strongest peaks No. 1 and 4 are corresponding to both cubic and hexagonal structures, while the peaks No. 2, 3, 5 and 6 are only corresponding to the hexagonal structure. The fact that the ZnS films could easily be

grown with cubic and hexagonal structures simultaneously [67, 68] suggests that the film grown on the glass substrate is composed of grains with both cubic and hexagonal structures.

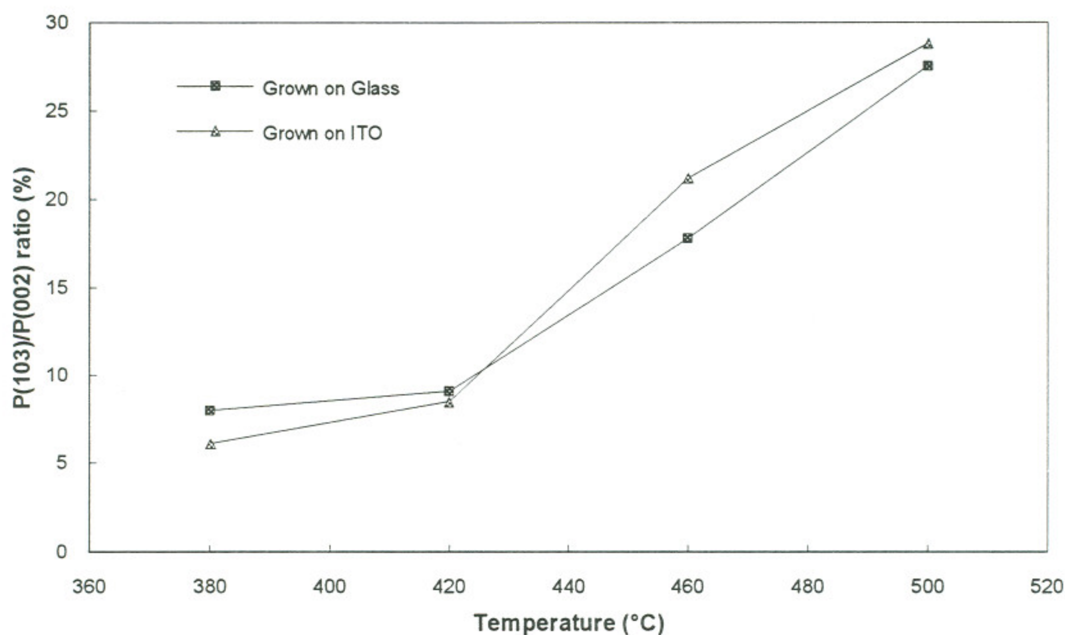

Fig. 4.5.2 Ratio of X-ray diffraction peak intensity, peak (103) over peak (002).

From the Fig. 4.5.1, we can see that the component of the hexagonal structure increases with an increase in growth temperature as indicated by the increasing intensity of the peaks (No. 2, 3, 5 and 6) belonging to the hexagonal structure. As shown in Fig. 4.5.2, we can also use the intensity ratio p(103)/p(002) to show this tendency, where p(103) (peak No. 5) is the intensity of peak (103) of hexagonal structure, and p(002) (peak No. 1) is possibly the combination of peak (002) of hexagonal phase and peak (111) of cubic phase. The increase of intensity ratio p(103)/p(002) from about 6-8% to 28-29% as shown

in Fig. 4.5.2 indicates a significant increase of the component of the hexagonal structure at higher growth temperature. Fig 4.5.2 also includes the results for ZnS grown on ITO substrates, which show similar tendencies.

It is worth noting from Table I that the hexagonal peak (100) is missing. This suggests that the (100) plane of the ZnS grains (of hexagonal phase) is not randomly oriented, but has a preferred orientation. We propose that the ALE ZnS thin film grows with the (100) plane parallel to the substrate.

4.6 ACTFEL device fabrication by ALE

As we have discussed in this chapter, the process conditions for Al_2O_3, ZnS and SrS films grown on glass substrates by ALE were studied. Based on the established conditions, the ZnS and SrS EL devices were fabricated using ALE technique.

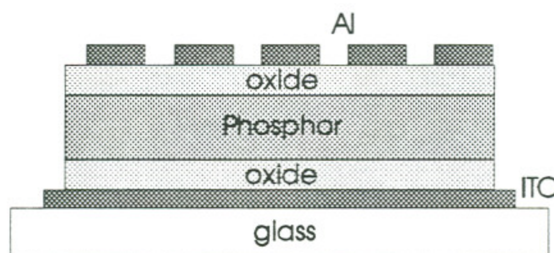

Fig. 4.6.1 Cross sectional view of the EL device fabricated by ALE process.

As shown in Fig. 4.6.1, the TFEL device fabricated in this work consists of a multilayer structure that is composed of a phosphor layer which is sandwiched between Al_2O_3 insulators. This structure is grown on an indium tin oxide (ITO) coated glass

Table II The Process Conditions of Different Types of Phosphor Layers.

Device type by Phosphor	Substrate temperature	Precursor for Sr/Zn :temperature.	Precursor for dopant/temp.	Number of growth cycle
ZnS:Tb	450 °C	$ZnCl_{2::}$340 °C	$Tb(thd)_3$:155 °C	ZnS:Tb - 10x600*
ZnS:Pr	450 °C	$ZnCl_2$:340 °C	$Pr(thd)_3$:160 °C	ZnS:Pr - 12x500
SrS:Pr/ZnS	380 °C / 420 °C	$Sr(thd)_2$ / $ZnCl_2$: 222 °C / 340 °C	$Pr(thd)_3$:160 °C	ZnS/SrS:Pr/ZnS: 800/10x600/800
SrS:Eu/ZnS	380 °C / 420 °C	$Sr(thd)_2$ / $ZnCl_2$: 230 °C / 340 °C	$Eu(thd)_3$:158 °C	ZnS/SrS:Eu/ZnS: 800/10x500/800
SrS:Ce/ZnS	380 °C / 420 °C	$Sr(thd)_2$ / $ZnCl_2$: 230 °C / 340 °C	$Ce(thd)_4$:160 °C	ZnS/SrS:Ce/ZnS 800/10x500/800
SrS:Eu	380 °C	$Sr(thd)_2$:220 °C	$Eu(thd)_3$:158 °C	SrS:Eu - 10x600
SrS:Ce	380 °C	$Sr(thd)_2$:220 °C	$Ce(thd)_4$:160 °C	SrS:Ce - 10x600

* Here 10x600 means that there are a total of 6000 ALE cycles with Tb introduced to the substrates for every 10 cycles.

substrate in the ALE reactor described in section 4.1. For the ZnS based device, the aluminum oxide insulating layers were grown from $AlCl_3$ and water at 450 °C with thickness of 240 nm. For SrS based devices, aluminum oxide layers were grown at 420 °C and 2-methyl-2-propanol was used as one of the precursors instead of water. For each multilayer structure growth, both aluminum oxide and phosphor layers were grown

sequentially after one pump down. Electrical connection to the bottom of the stack is via the transparent ITO film. The electrodes on top of the stack were 3 mm diameter aluminum pads deposited in a physical evaporator chamber at $6x10^{-7}$ torr vacuum.

The process conditions for growing various phosphor layers are listed in Table II. During these processes, the flow rate of N_2, which is the purging inert gas, was controlled by two mass flow controllers; the flow rate was kept at 700 sccm for the inner tube and 300 sccm for the outer tube. (sccm = standard cubic centimeter)

In this study, it was found that the green light emitting ZnS:Tb based devices were relatively stable, and more repeatable measurements could be done. Electrical and optical properties of ZnS:Tb based devices are discussed in Chapter 5.

For the devices based on SrS, a ZnS buffer layer was grown before and after each SrS layer growth to prevent SrS from reacting with oxygen in the aluminum oxide insulator. Devices doped with Pr, Eu and Ce were grown in order to develop a white phosphor material. The spectral characteristics of these devices are presented in Chapter 6. No electrical measurement was recorded for the SrS based devices because these devices were unstable and short lived.

Chapter 5
Characterization of ZnS:Tb EL Devices

Electrical and optical characterizations are crucial for understanding device physics and evaluating device performance of TFEL devices. In this chapter, the electrical test procedures and results for ZnS:Tb ACTFEL devices are presented. The device characteristics are also evaluated with the assistance of UV radiation. The transition energy levels of Tb ion in ZnS were identified via the spectral characterization. The correlation between the excited Tb ions and its surrounding lattice was studied via rapid thermal annealing treatment and relaxation time measurements. A computer model based on the tunneling theory was developed to fit the capacitance-voltage characteristics.

5.1 Electrical characterization methods for ACTFEL devices

As discussed in section 2.6 the equivalent circuit of an ACTFEL device can be regarded as three capacitors in series, where the capacitor in the middle corresponds to the phosphor layer becoming a leaky capacitor after breakdown, and the other two capacitors at each side correspond to the insulator layers being ideal capacitors. When the voltage applied across the device reaches a critical value, large amount of electrons start moving across the phosphor, i.e. the phosphor "breakdown". This voltage is called breakdown voltage. Since it is difficult to measure the charge transfer inside the phosphor, the Sawyer-Tower configuration [36], with a resistor or a capacitor in series with the device under test (DUT), is employed. The schematic of the studied ACTFEL device with the

Sawyer-Tower test setup is shown in Fig. 5.2.1. Each device is defined under a 3 mm diameter aluminum dot evaporated on a sample prepared by ALE.

For a standard capacitor, its capacitance is not a variable of the applied voltage, because the capacitance between the two electrodes is defined by the relative distance, the dielectric filled in between them, and their area. However for TFEL devices the capacitance C(V) is a function of the voltage applied. At a voltage below breakdown, the total capacitance C_t is a constant and can be calculated by treating the three layers as three capacitors in series (Fig. 2.6.1):

$$\frac{1}{C_t} = \frac{1}{C_{ox1}} + \frac{1}{C_{ph}} + \frac{1}{C_{ox2}} \qquad \text{eq. (5.1.1)}$$

where C_{ox} and C_{ph} are the capacitance corresponding to the oxide and phosphor layers, respectively.

To understand the characteristics of the EL device capacitance after phosphor breakdown, we shall consider the charge distribution of the capacitors when the voltage V(t) is applied. Before the breakdown, there are equal amounts of charge Q(t) on each of the three capacitors, C_{ox1}, C_{ph} and C_{ox2}, respectively. After breakdown, C_{ph} becomes leaky. Assume there is an amount of charge $Q_l(t)$ (polarization charge) that leaks to the opposite side of C_{ph}. The amount of charge on C_{ph} becomes $Q(t)-Q_l(t)$. From the measurement of Q(t) on the device, the C(V,t) can be calculated as:

$$C(V,t) = \frac{Q(t)}{V(t)}, \qquad \text{eq. (5.1.2)}$$

where $$V = V_2 - V_1 = V_{ox1} + V_{ph} + V_{ox2}.$$ eq. (5.1.3)

Substituting each term in eq. (5.1.3) with the relationship of eq. (5.1.2) yields:

$$\frac{Q(t)}{C(V,t)} = \frac{Q(t)}{C_{ox1}} + \frac{Q(t) - Q_l(t)}{C_{ph}} + \frac{Q(t)}{C_{ox2}}$$ eq. (5.1.4)

After rearranging eq. (5.1.4), we get,

$$\boxed{C(V,t) = C_t(1 + \frac{1}{C_{ph}} \cdot \frac{Q_l(t)}{V(t)})}$$ eq. (5.1.5)

where C_t is the total capacitance below the breakdown as defined in eq. (5.1.1). We consider V(t) to be a linear voltage ramp, i.e., V = (slew rate) * time. The significance of eq. (5.1.5) is that it allows us to measure the dynamics of the internal polarization charge $Q_l(t)$ from the capacitance-voltage measurement or vise versa.

To have a better understanding of the electron transport characteristics, it is very important to know the electric field in the phosphor. Since breakdown voltage is very much structure dependent, the electrical field of the phosphor at the breakdown becomes a more important parameter for EL devices. It is difficult, if not impossible, to measure the internal field directly. However, the Sawyer-Tower circuit does allow for measurement of the average internal field indirectly. From the measurement the required boundary conditions are determined as the voltage across the device $V_2(t)$-$V_1(t)$ and the amount of charge on the electrodes $Q(t) = C_s V_1(t)$ as measured with the series capacitor C_s (Fig. 5.2.1). Using $\overline{E}_{ph} = \frac{V_{ph}}{d_{ph}}$ and eq. (5.1.3), the following can be derived:

$$\overline{E}(t) = \frac{1}{d_{ph}}\left[V(t) - V_{ox1}(t) - V_{ox2}(t)\right]$$

i.e. $$\overline{E}(t) = \frac{1}{d_{ph}}\left(V_2(t) - V_1(t) - C_s \cdot V_1(t)\left(\frac{1}{C_{ox1}} + \frac{1}{C_{ox2}}\right)\right) \qquad \text{eq. (5.1.6)}$$

Rearranging eq. (5.1.4), the transferred charge becomes:

$$Q_l(t) = C_{ph}\left(V_2(t) - V_1(t) - V_1(t) \cdot \frac{C_s}{C_t}\right) \qquad \text{eq. (5.1.7)}$$

Therefore, the internal field and polarization charge can be calculated from the measurable quantities, V_1(t) and V_2(t), provided the structure parameters, including the thickness and dielectric constants of the phosphor and the two insulator layers, are known.

5.2 The dynamic study of polarization charge and internal field with the assistance of ultraviolet laser radiation

Photoluminescence is a powerful probe for analyzing the properties of solid state devices and materials [69, 70]. To find the origin of the electrons that are transported in a wide band gap ZnS phosphor in a TFEL device during breakdown, laser radiation at various wavelengths including visible (454 nm, 488 nm,) and ultraviolet (352 nm) wavelengths, was employed during emission measurements of the EL devices. It was expected that at a certain wavelength, the electrons could be excited to the conduction

band from either interface states or some energy levels in the forbidden band; but the results showed that only the UV (352 nm) radiation, which is on the edge of the absorption band of ZnS (326 nm) had any significant effects.

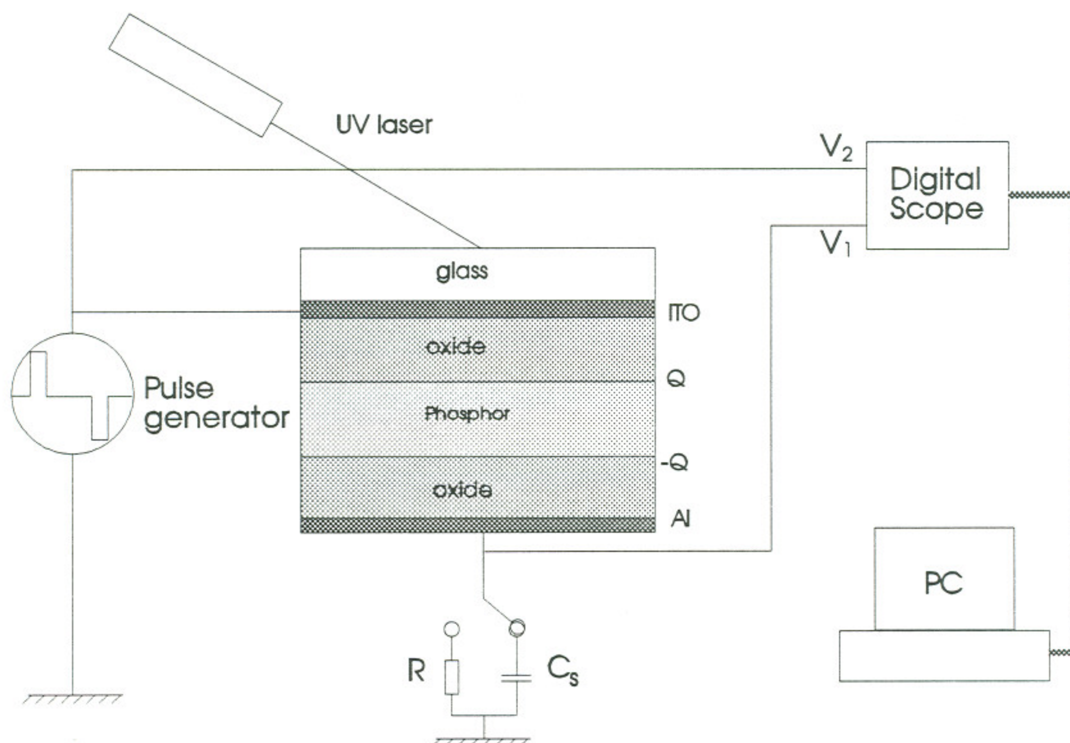

Fig. 5.2.1 Experimental setup for characterizing EL device with UV radiation.

The experimental setup for this study is shown in Fig. 5.2.1. The device used in this experiment was a ZnS:Tb TFEL device made by Planar America. A laser spot of about 3 mm diameter was projected on the EL device of similar dimension.

It was found that EL emission can be enhanced near the breakdown voltage and attenuated at higher voltage by irradiating the device with UV radiation from an argon ion laser. Fig 5.2.2 shows the emission light intensity vs. voltage with the UV laser on and off.

The breakdown voltage is about 100 V for this device. At a voltage above 150 V the laser reduces EL emission.

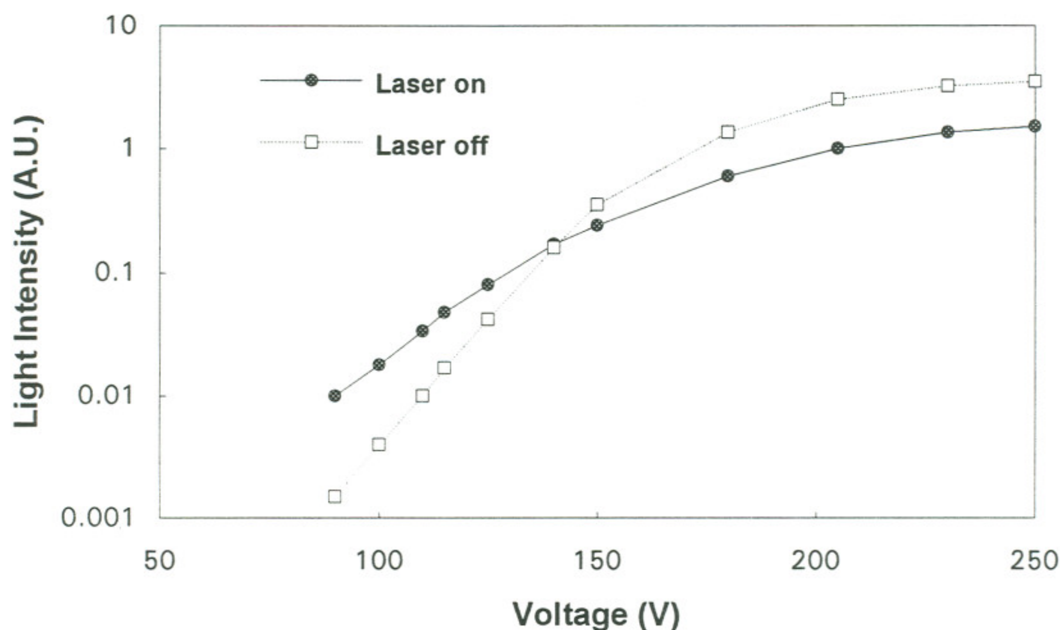

Fig. 5.2.2 The emission intensity (arbitrary unit) of the ZnS:Tb EL device with and without the laser radiation versus the operating pulse amplitude.

To understand why the UV laser radiation affects the EL intensity, the polarization charges (it is assumed that all charges reside at the phosphor-oxide interface with none in the bulk) and the electrical field in the phosphor were examined using the technique discussed in section 5.1. Fig. 5.2.3 and Fig. 5.2.4 compare the internal field and polarization charge variation following the driving voltage pulses in real time, with the laser on and off, respectively.

In Fig. 5.2.3 the peak voltage is 130 V, a voltage amplitude at which the EL intensity is enhanced under irradiation. From Fig. 5.2.3(a), it can be seen that without laser irradiation, the number of charges generated from the phosphor due to the driving voltage is small, so is the number of activators being excited. Hence the EL intensity is low. In the presence of UV laser radiation, photo generated carriers significantly increase the total charge swept across the phosphor, therefore the EL intensity is stronger. Unlike field extracted charges which are produced only during the duration of the applied pulses, the photo generated carriers are produced continuously by the laser radiation. These carriers drift in the polarization field (produced by polarization charge) and neutralize the polarization charges at the dielectric-phosphor interface. As a result, the net internal field for the duration of the pulse is reduced in the presence of the UV radiation as shown in Fig. 5.2.3(b).

In Fig. 5.2.4 the peak voltage is about 250 V, at this voltage the EL intensity is attenuated during the laser irradiation according to Fig. 5.2.2. From Fig. 5.2.4(a), it can be seen that a large portion of the polarization charges accumulated on the dielectric-phosphor interface is neutralized due to the photo generated carriers. This is detrimental to the electroluminescent intensity because reduced polarization charges mean a reduced total field for the next voltage pulse in the opposite polarity, since the total field is contributed by both voltage pulse and polarization charges. This is reflected in Fig 5.2.4(b) where the maximum field with the laser on is about two thirds of the maximum field with the laser off.

The photo generated electrons have been regarded as originating from photo stimulated band to band transitions. The possibility of other kind of electron donor-like defects or activators were ruled out by experiments: (a) using an undoped device and UV

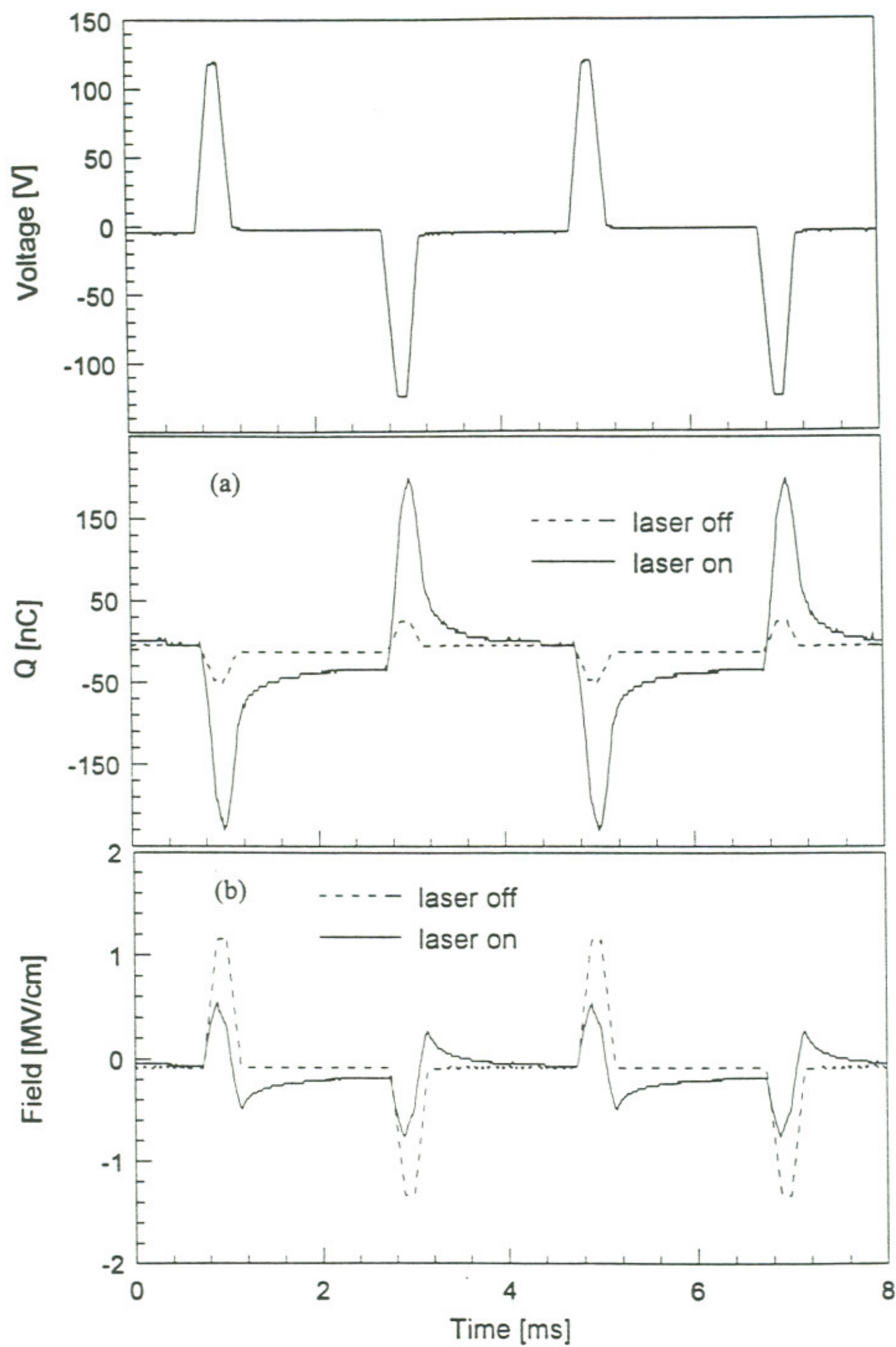

Fig. 5.2.3 The charge $Q_I(t)$ stored at the phosphor/oxide interface (a), and the average electric field (b) at 130 V pulses, with and without 352 nm radiation.

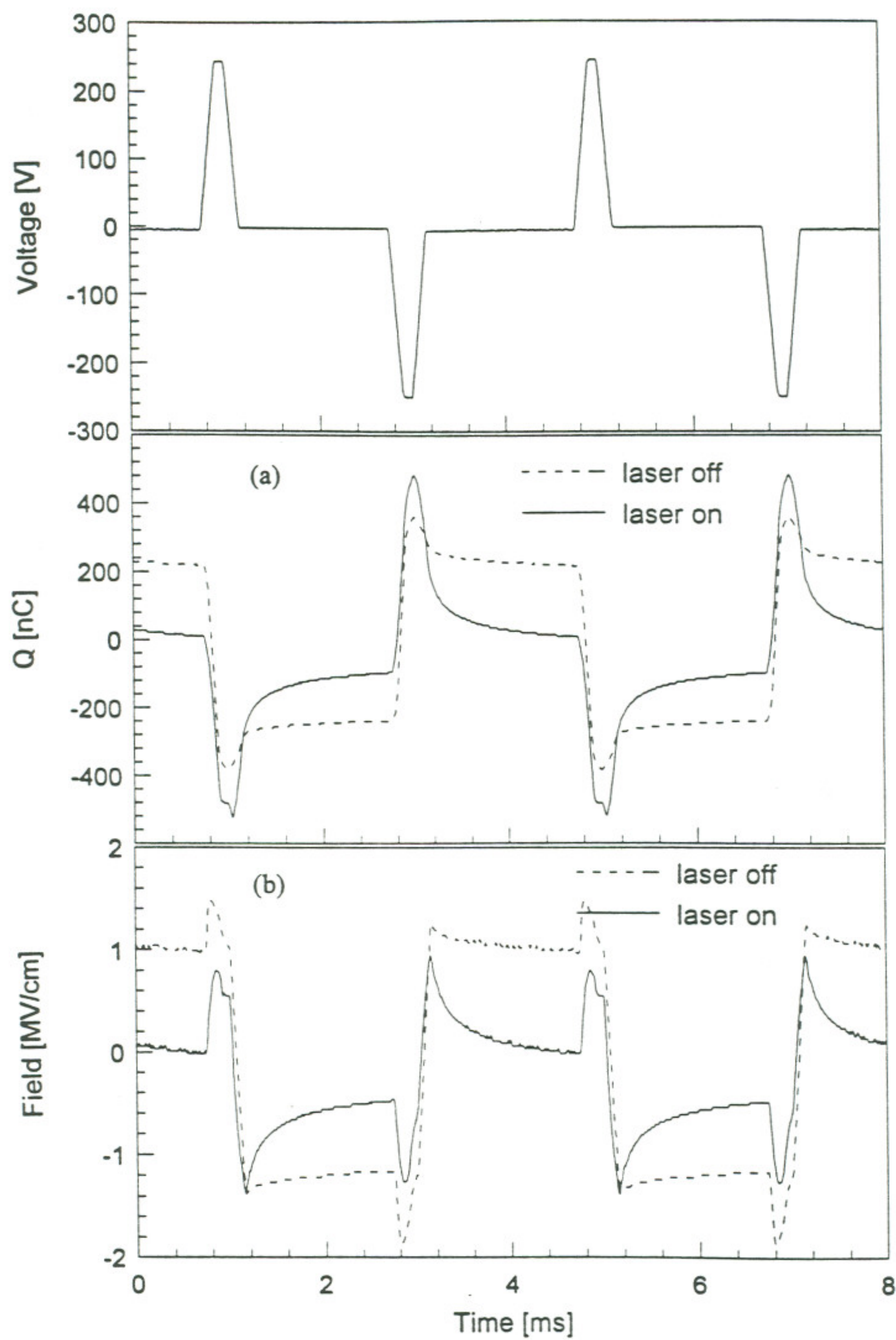

Fig. 5.2.4 The charge $Q_l(t)$ stored at the phosphor/oxide interface (a), and the average electric field (b) at 250 V pulses, with and without 352 nm radiation.

laser which yielded the same photo conductive current that was observed from the original doped device; (b) using the same doped device with visible laser radiation (455nm, 488nm and 528nm). There are two possible reasons why there were no other significant phenomena observed using a visible laser. (i) the interface state(s), as many researchers have indicated, may be deep (deeper than 2.5 eV). (ii) the cross section of the interface state(s) needed to absorb photons is very small. As will be discussed in section 5.4, the tunneling model suggests that the interface state is located about 0.6 ~ 1.0 eV below the conduction band edge of ZnS. Similar results have also been suggested by other authors [20, 21]. These results support the second (ii) hypothesis. If the interface state, however, is indeed proved to be deeper than 3.0 eV, other electron generating mechanism, such as impact ionization, must be considered.

It is worth noting that in Fig. 5.2.4, significant asymmetrical polarization field and polarization charge are shown. This could result from the ALE ZnS thin film growth characteristic shown by the AFM study discussed in section 4.3.

5.3 EL efficiency study of ZnS:Tb devices treated by rapid thermal annealing and at low temperature

There is an important issue to be addressed, that is whether post-deposition anneal of ALE samples would enhance the brightness for ZnS:Tb based devices. The idea was based on our prior work where rapid thermal anneal (RTA) of sputtered ZnS:Mn EL devices led to significant improvement in their brightness and luminescence efficiency [71]. To investigate the effect of annealing, one of two ZnS:Tb samples grown per ALE run was annealed using RTA, prior to metallization of the top electrodes. The RTA condition

was 700°C for 60s in an atmosphere pressure Ar gas environment. The characteristics of the devices with different Tb concentrations were examined, including brightness at 40V above threshold and relaxation times, as listed in Table III. The ZnS:Tb devices were low doped (0.3%), medium doped (1%) and high doped (2%) with Tb [72].

Table III Relaxation time and brightness of ZnS:Tb devices

Estimated Tb doping level	Brightness (fL) @ V_{th} + 40 V (1kHz)		Relaxation time (μs)		EL efficiency (lm/W)	
(atom %)	As grown	Annealed	As grown	Annealed	As grown	Annealed
low (0.3%)	31.2	31.0	228	331	N/A	N/A
medium (1%)	44.5	49.7	395	416	0.18	0.20
high (2%)	21.6	20.8	126	330	N/A	N/A

The EL spectra of these devices were taken by a spectrometer attached with a photomultiplier tube and an x-y recorder. There is no significant spectral difference among these devices with different doping level, annealed or as-grown. The EL spectrum of the medium doped device showed transitions from $^5D_4$ to $^7F_{3,4,5,6}$ levels [72] as shown in Fig. 5.3.1. These are relatively sharp peaks due to the screening effect from the 5s5p electron shell. The ground state $^7F_6$ results from 7 parallel spin electrons and one anti-parallel spin electron occupying the 7 orbitals with the directions of the orbital angular momentum m_L = 0, ±1, ±2, ±3. The first excited $^5D_4$ state has one of the 7 parallel spin electrons flipped over. The average relaxation life time of these transitions was measured by a Si photo detector when a bipolar voltage pulse was applied. The output signal from the photo

detector was read from an oscilloscope. Because these are forbidden f-f transitions, the measured relaxation life times were relative long, on the order of hundreds micro-seconds. From Table III, one can see the relaxation life times for all samples improved after RTA.

The increase of the relaxation life time suggested that some non-radiative relaxation channels have been removed by annealing. The luminescence efficiency measured for the two medium devices (done by Planar America) was 0.18 lm/watt for the as-grown sample and 0.20 lm/watt for the annealed sample. There is an increase of about 10% in luminescence efficiency by annealing.

The brightness vs. charge characteristic is another way to compare the efficiency of the TFEL devices. Brightness is measured by a TOPCON BM-7 luminance colorimeter in units of foot-lamberts. It is known that the photon emitting activators are stimulated by hot electrons traveling in the phosphor layer. The total number of electrons (difference between Q_l at positive maximum and negative maximum corresponding to the two peaks of the bipolar pulse) that have been driven across the phosphor layer during one pulse period can be recorded by the technique described in section 5.1. The comparison of brightness vs. charge plot between as-grown and annealed samples is shown in Fig. 5.3.2. As the amplitude of the driving voltage pulse increases, there are more electrons traveling across the phosphor, and they generate more photons. The slope of the Brightness-Charge curve is directly related to the quantum efficiency of the device. The annealed device gives out more photons for the same transferred charge. One should note that, as mentioned in section 5.1, the charge is assumed to travel between the two phosphor-oxide interfaces and there is no localized space charge in the phosphor.

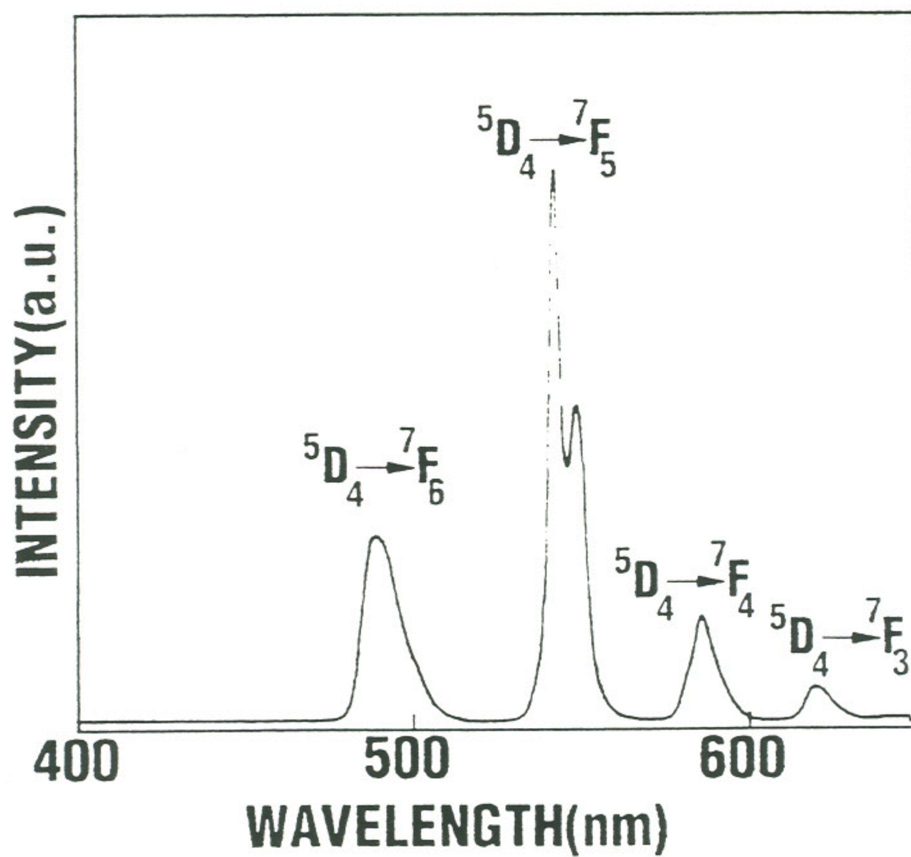

Fig. 5.3.1 Emission spectrum of ZnS:Tb electroluminescent device.

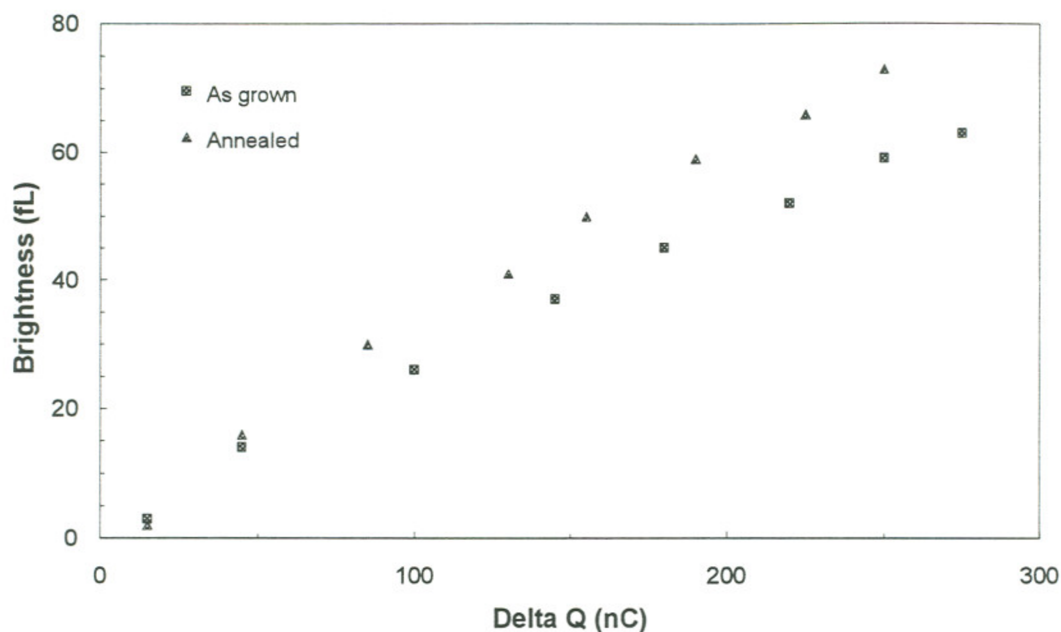

Fig. 5.3.2 Transferred charge (ΔQ) versus brightness plot for the medium doped device at f = 1kHz showing higher efficiency after RTA treatment.

Besides the crystal defects that can cause inefficiency for TFEL devices, thermal quenching may be another reason for reduction in luminescence efficiency. When the thin film temperature increases, lattice vibration can assist relaxation of electrons through non-radiative relaxation channels, by adsorbing (releasing) phonons. The thermal quenching phenomenon can be seen when the driving pulse frequency is high. In Fig. 5.3.3, brightness vs. frequency is plotted for the medium doped device. It is shown that at a liquid nitrogen temperature of 77K, the thermal quenching effect is greatly reduced.

The X-ray diffraction patterns show narrower peaks after RTA, indicating improved crystal quality in the sense of fewer defects and perhaps larger grain size. However, the peak intensity was not increased, but rather decreased by about 20% in

some cases. It is postulated that although the larger grain size after RTA will result in sharper peaks, it may also lead to a reduced number of grains contributing to the X-ray diffraction intensity. We should note that comparison of pre and post annealed x-ray diffraction spectra of undoped ZnS showed no significant difference.

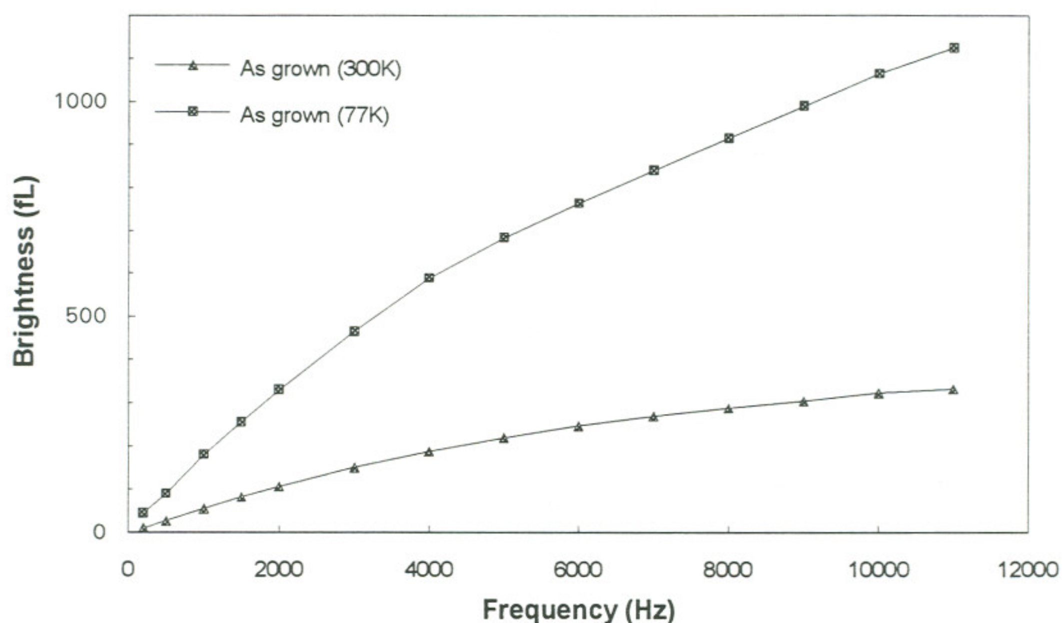

Fig. 5.3.3 Relationship between brightness and frequency for the medium doped as-grown device showing the brightness enhancement at lower temperature (77 K).

The results from RTA treatment and the low temperature measurement suggest that electroluminescent efficiency is closely related to the non-radiative relaxation channels in the crystal, which could be thermal phonons and defects.

5.4 Numerical modeling of C-V characteristics of ZnS:Tb ACTFEL devices

In order to emit visible light efficiently, the host materials used for TFEL device must be a wide band gap semiconductor so that the emission is not being re-absorbed by the host lattice. This type of device usually operates at very high electrical field, about 1.5 MV/cm for ZnS. For years, the source for the required conduction electrons at high field has been a point of debate. In this section, a ZnS:Tb based TFEL device (the medium doped device discussed in 5.3) is used as an example to address the electron transport mechanism. A numerical simulation based on the tunneling theory is presented. Another model, based on impact ionization is also briefly discussed

It has been widely accepted that the conducting charge in ZnS TFEL device results from electrons. The possible electron sources for the conducting current are: (a) field emission (tunneling) from interface states; (b) field emission from deep defect levels; (c) impact ionization from activators and (d) impact ionization from valence band. For ZnS based devices, the possibility of (c) has been ruled out [47]. The experimental evidence of space charge in the phosphor layer supports the theory that electrons originate from some defects states (b), and are field-emitted to the conduction band by tunneling. However, for the ACTFEL devices, at above breakdown voltage, the electrons transfer from one side of the phosphor to the other and stay in the phosphor-insulator interface states regardless of their origin (either from interface states or bulk). So in the following discussion the electron origin (a) and (b) will not be distinguished, rather a concept of electron tunneling from a source represented by a lumped density of states function $N(\varepsilon)$ located at energy ε (eV) below the conduction band is used in the numerical simulation. The impact ionization

theory (d) will be discussed separately. Although these two models, impact ionization and tunneling, are not necessarily mutually exclusive, much effort has been made to determine which mechanism is dominant.

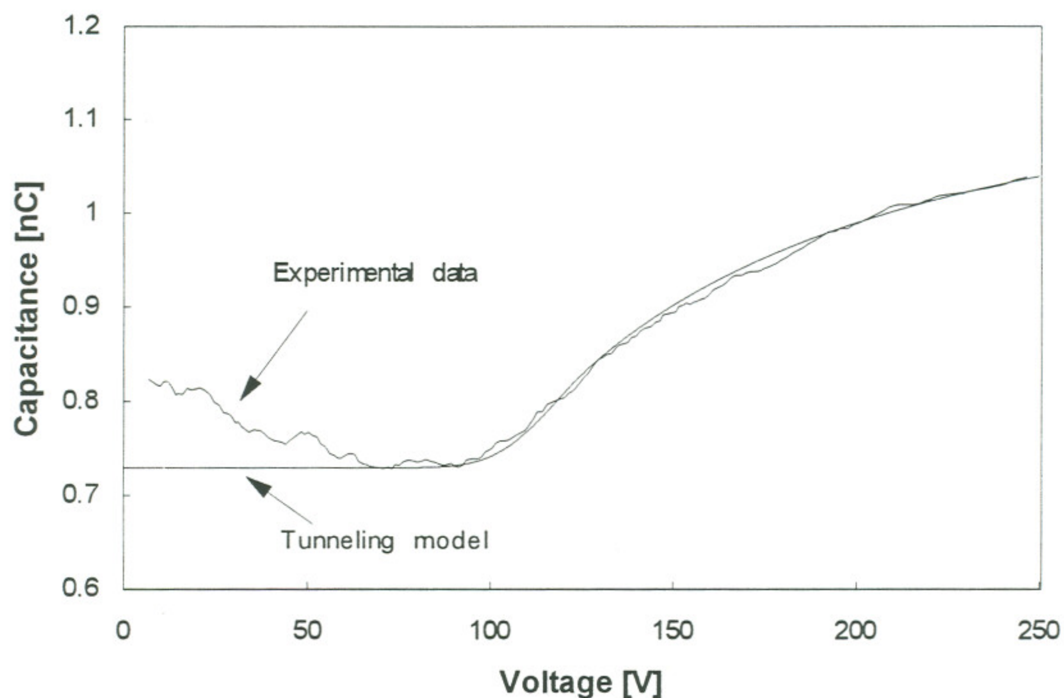

Fig. 5.4.1 C-V characteristics from experimental measurement and computer simulation, based on a ZnS:Tb ACTFEL device.

To measure the C-V characteristics of the device, a linear voltage ramp $V_2(t)$, was applied on the device shown in the Sawyer-Tower test set-up in Fig. 5.2.1. For C-V measurements, the capacitance variation of the EL device was determined by measuring the voltage across the device $V_2(t)$-$V_1(t)$, and the charge accumulated on the aluminum electrode at the same time, where the charge is determined by measuring the voltage drop

$V_1(t)$ on the series capacitor C_s in Fig. 5.2.1. The capacitance C(V) can be calculated as $C(V) = C_sV_1(t)/[V_2(t)-V_1(t)]$. Here C_s is 0.1 μF, which is much larger than the DUT.

Fig. 5.4.1 shows the experimental C-V plot of the same ZnS:Tb device. One can see as the voltage applied to the device is beyond breakdown voltage, the phosphor layer becomes conductive. This is equivalent to saying that the center capacitor in the equivalent circuit is a shunt, resulting in an overall increase in capacitance C(V).

In the tunneling model, the electron source is considered as a lumped density of state function which is assumed to have a Gaussian distribution located at ε_0 below the conduction band of ZnS:

$$N(\varepsilon) = \frac{N_0}{\sqrt{2\pi a}} \exp\left[-\frac{(\varepsilon - \varepsilon_0)^2}{2a^2} \right] \qquad \text{eq. (5.5.1)}$$

where a represents the width of the distribution and N_0 is the total number of electrons the state can hold. A FORTRAN program was written to simulate the voltage ramping process used during the C-V measurement described above.

The electrons trapped in interface states $N(\varepsilon)$ follow Fermi distribution. $\psi(\varepsilon, E)$, the tunneling rate of electrons through a Poole-Frenkel barrier under field E, can be calculated through eq. (2.6.1), where $m^* = 0.3\ m_e$ was used as the effective electron mass for ZnS [23]. Knowing the tunneling rate $\psi(\varepsilon, E(t))$ at a given voltage the C-V characteristics can be simulated based on eq (5.5.1), where the tunneling charge $Q_l(t)$ can be calculated as follows,

$$Q_L(t) = \int_{\Delta t} dt \int_0^{3eV} \frac{q \cdot N(\varepsilon)}{1+e^{(\varepsilon-\varepsilon_f(t))/kT}} \cdot \Psi(\varepsilon, E(t)) \cdot d\varepsilon \qquad \text{eq. (5.5.2)}$$

where, E(t) can be calculated from eq. (5.1.6). For each integration step $\Delta t = 0.12$ μs, which is corresponding to a 0.2 volt voltage step. The Fermi level $\varepsilon_f(t)$ is determined by the total trapped charge available, i.e.,

$$Q_{Total}(t) = \int_0^{3eV} \frac{q \cdot N(\varepsilon)}{1+e^{(\varepsilon-\varepsilon_f(t))/kT}} \cdot d\varepsilon \qquad \text{eq(5.5.3)}$$

During the $Q_l(t)$ integration in eq. (5.5.1), after each step, the amount of charge Q_l lost to tunneling is deducted from Q_{Total} and the $\varepsilon_f(t)$ is re-calculated and the new ε_f value is used for the next step integration.

With this tunneling model, the abrupt turn on behavior of C-V characteristics was numerically simulated. The modeled C-V curve is shown in Fig. 5.4.1. From the curve fitting, the most important parameters found were: $a = 0.02$ eV, which is about kT at room temperature, $\varepsilon_0 = 0.7$ eV, i.e., the electron states are 0.7 eV below the conduction band edge in the ZnS phosphor, $Q_{Total} = 6.8\text{x}10^3$ nC/cm^2 and $qN_0 = 9.1\text{x}10^3$ nC/cm^2 which are of the same order of magnitude as the polarization charge Q_l measured in section 5.3.

There are however, no experimental results supporting these simulation results. Rather our optical experiments designed to probe the interface states have failed. A possible reason for the inefficient optical stimulation could be that the cross section of photon absorption is too small.

Another theory on the origination of the free electrons is based on the band to band impact ionization leading to breakdown at high electrical field. This possibility has been ruled out by some authors [73] because the results from their Monte Carlo simulations and other theoretical estimations of the electron transport in the phosphor showed the electron energy distribution to be not high enough to induce avalanche breakdown. From their numerical simulation results, the number of high energy electrons in the whole electron ensemble that can excite band to band transition is low. Therefore it would not be possible to create an avalanche which, by definition, needs an infinite electron multiplication factor.

However it is not necessary to have a full scale avalanche to explain the abrupt turn on behavior of ZnS:Tb based ACTFEL devices. Actually, even if a small tail of the electron energy distribution exceeds the band gap energy, this portion of electrons will give a net gain in the total number of electrons. The Monte Carlo simulation developed by our group showed that, by counting the number of electrons with energy 1.5 times above the band gap energy E_g, and assuming they contribute to band to band excitation, a very good fit of the experimental C-V curve was achieved [74]. The results are analogous to what has been shown in the tunneling model and are not repeated here.

The agreement of the results of the tunneling model and the impact ionization model does not help to identify which mechanism is correct. Rather, as stated by Dr. Bringuier in 1993, "any reasonably-based model subsuming the feedback feature should yield comparable agreement" [75]. The feedback feature mentioned here is the field clamping effect due to the accumulating of polarization charge, which has been considered in the numerical simulations discussed in this section.

Chapter 6
Optical Characteristics of the EL Devices

Luminescence spectroscopy is a very helpful tool to unravel the complicated electronic structure of localized optical centers and the process of energy transfer among different centers. In this chapter, photoluminescence (PL) spectroscopy and electroluminescence spectroscopy of rare earth elements including Pr, Eu, Ce, are studied and presented as related to the process of ALE grown TFEL devices. The emission spectra shall be presented and energy transition shall be identified based on the principles outlined in section 2.5.

6.1 Praseodymium doped SrS and ZnS

To achieve white light emitting displays, several combinations of rare earth activators have been examined. Among these activators, Pr^{3+} luminescent centers are unique in the sense that they produce white light emission by themselves. The advantage of the single activator doping is that the color generally remains unchanged when the driving conditions are varied, while multi-activator doping has charge transfer possibilities which could alter the color of the light output.

SrS and ZnS TFEL devices doped with Praseodymium were made by ALE. The process conditions have been described in chapter 4. The EL spectra of ZnS:Pr and SrS:Pr/ZnS are shown in Fig. 6.2.1 (a) and (b) respectively. When considering LS coupling, two electrons in the 4f subshell of a Pr^{3+} ion will degenerate into many energy

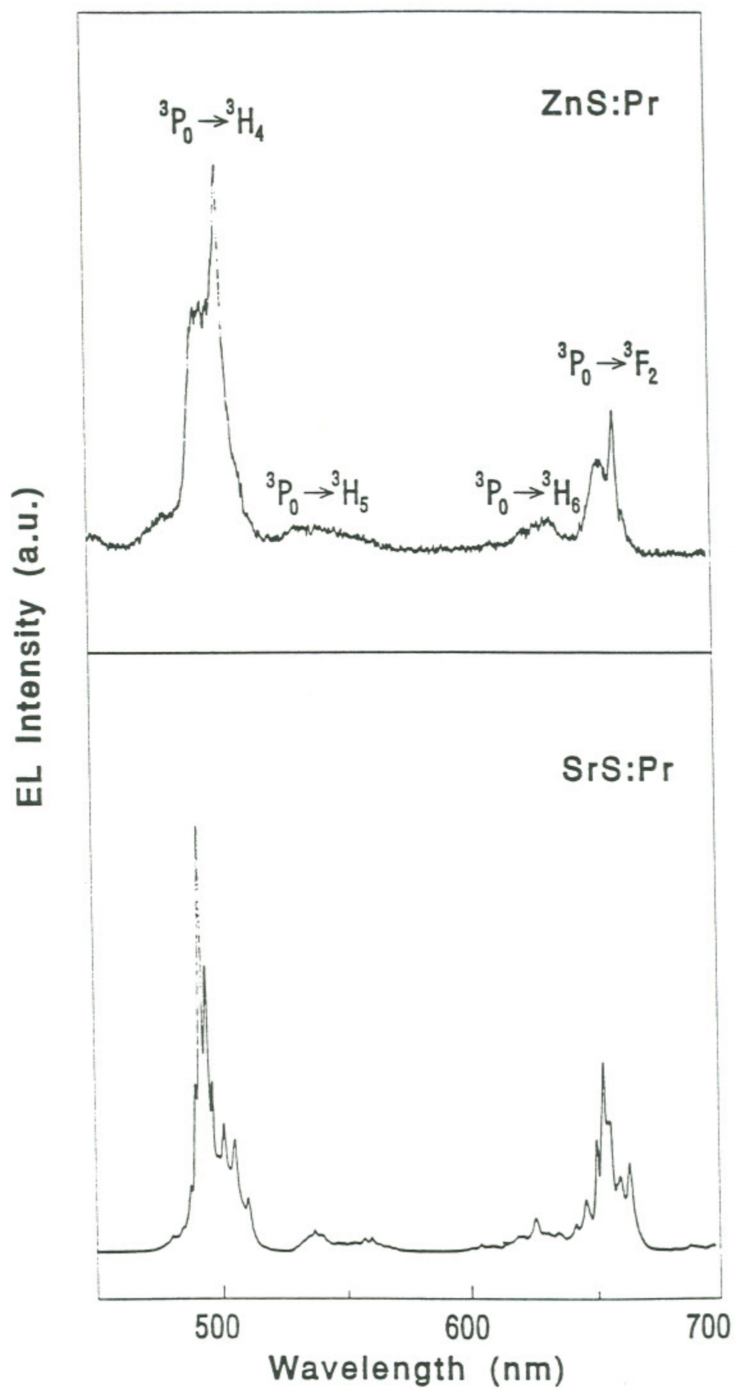

Fig. 6.1.1 Emission profiles of ZnS:Pr and SrS:Pr/ZnS electroluminescent devices.

levels. Among them the lowest energy state is, $^3H_4$. The next higher energy states are $^3F_{4,3,2}$, ...and $^3P_0$. It has been identified that the low energy peaks are $^3P_0$-$^3F_2$ transitions and the high energy peaks are $^3P_0$-$^3H_4$ transitions [76, 77]. It is interesting to note that the lower energy peak ($^3P_0$-$^3F_2$) in both spectra aligned with each other precisely as well as the higher energy peak ($^3P_0$-$^3H_4$). It is known that SrS and ZnS have a different crystal structure (see table IV [78]), ZnS is primarily hexagonal, and SrS is cubic, as discussed in Chapter 4. Therefore the crystal fields have different strengths and symmetries. The similarities between the two spectra provide a perfect example of how the 4f electrons are insensitive to their surroundings due to the 5s5p electron screening.

Table IV Comparison of physical properties of SrS, CaS and ZnS

	SrS	CaS	ZnS	ZnS
Crystal Structure	Rocksalt		3C	2H
Lattice constant(Å)	6.019	5.697	5.409	a=3.82, c=6.26
Ionic Radii of Cation(Å)	1.13 (Sr^{2+})	0.99 (Ca^{2+})	~0.74 (Zn^{2+})	
Ionicity	>0.785		~0.62	
Energy Bandgap(eV)	4.30	4.41	3.68	3.78
Dielectric Constant	9.4	9.3	8.3	8.3-16.0

The excitation mechanism is expected to be the same for both of these devices, i.e., both are due to electron impact excitation. As evidence for this, it was observed that the light pulse was emitted at the leading edge of the driving voltage pulse, as shown in

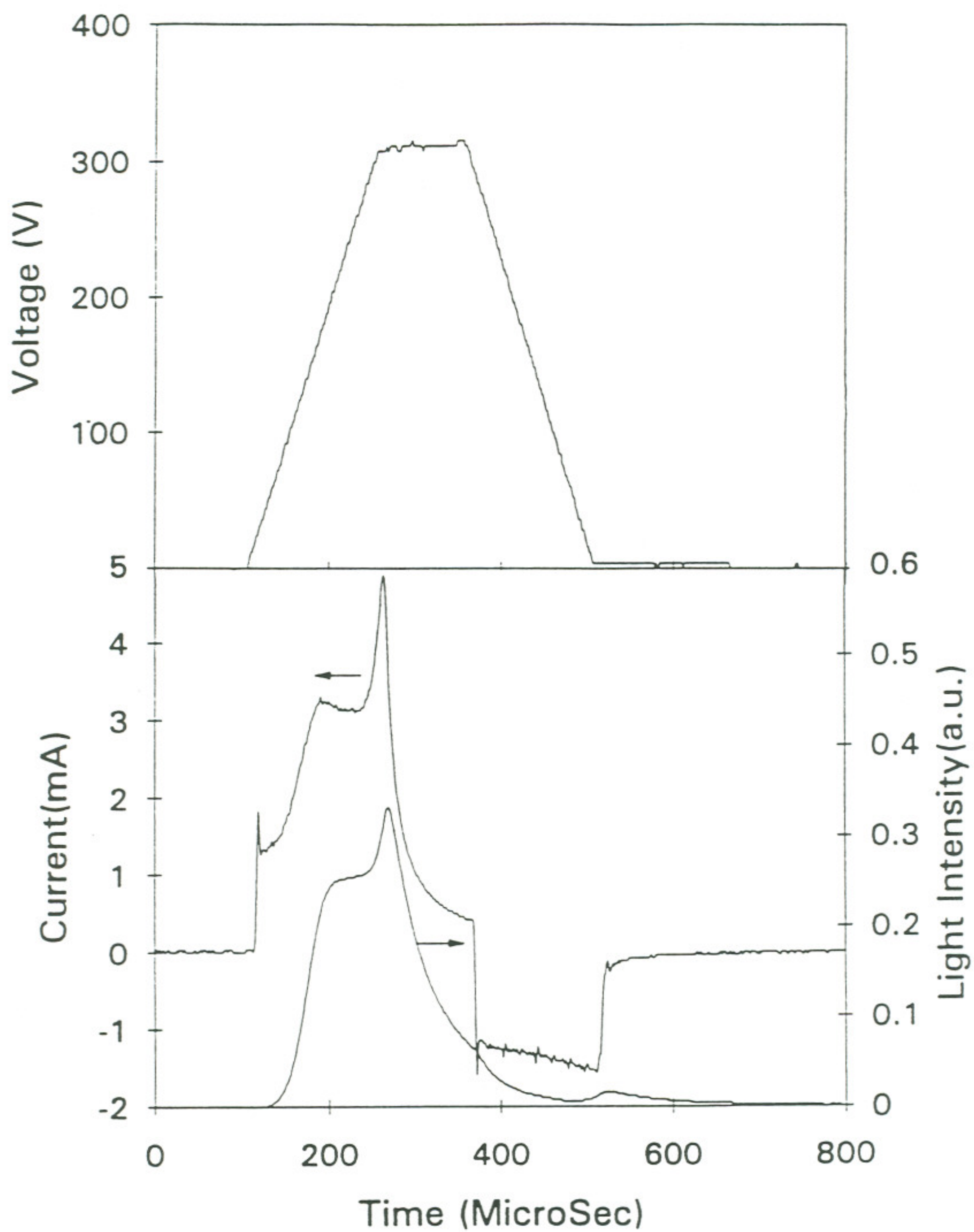

Fig. 6.1.2 Applied voltage pulse across the SrS:Pr EL device and its corresponding current and optical emission response.

Fig 6.1.2 for a SrS:Pr/ZnS sample. It was also noted that both current and light pulses had a two-stage profile. Therefore it is believed that ZnS and SrS have different breakdown fields, the SrS layer breaks down (corresponding to the first stage) prior to the breakdown of ZnS layer (corresponding to the second stage).

It was found that the SrS:Pr/ZnS based devices are an order of magnitude brighter than the ZnS:Pr devices. Because the ionic radius of Pr^{3+}(1.11Å) is very close to Sr^{2+} but much larger than Zn^{2+}, it is reasonable to assume that defects owing to the lattice distortion induced by the large Pr^{3+} ions in ZnS lattice lead to the decreased efficiency in ZnS:Pr devices. To support this postulate, these two devices were operated at 77K in liquid nitrogen; we found that the brightness of the ZnS:Pr device improved by a factor of 20, while the SrS:Pr device only improved by 3 times over the initial room temperature brightness. This suggests that non-radiative charge transfer conducted by lattice defects and assisted by thermal vibration is significantly reduced at low temperature in the ZnS:Pr devices.

6.2 SrS:Ce, SrS:Eu and $SrCl_2$:Eu based devices

SrS:Eu and SrS:Ce TFEL devices have been widely studied for their applications in full color EL displays. The EL emission of SrS:Eu is orange-red in color and SrS:Ce is greenish-blue. More recently, the idea of creating a "white phosphor" based on SrS doped with Ce and Eu has been suggested [79]. By and large two approaches have been used to make a white phosphor with a broad spectrum; (i) co-dope SrS with Ce and Eu; (ii) a multi-layer structure which includes SrS:Ce layer(s) and SrS:Eu layer(s). The advantage of the second approach is the elimination of energy transfer between Ce^{3+} and Eu^{2+} which

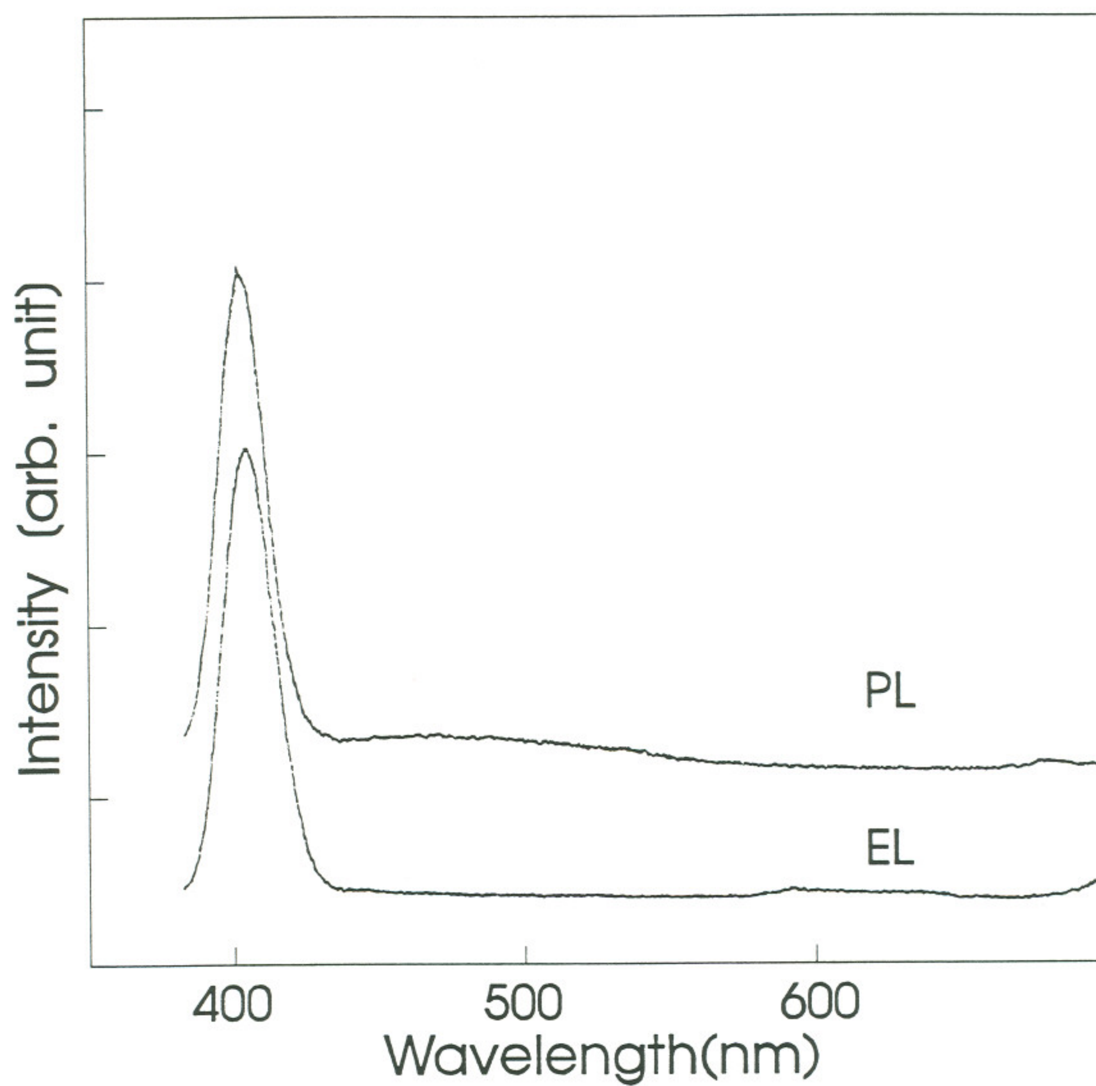

Fig. 6.2.1 Electroluminescent and photo-luminescent emission spectra of the violet light emission from $SrCl_2$:Eu in type A devices.

may result in lower luminescence efficiency and less stable color when operating at different conditions.

In this study, the atomic layer epitaxy technique was used to fabricate SrS TFEL devices doped with either Ce or Eu. The growth condition and precursors for SrS layer growth were described in section 4.6.

Two different device structures were made on Al_2O_3/ITO/glass substrates for both dopants; Structure A had 1000 Å undoped ZnS, followed by 8000 Å SrS, another 1000 Å undoped ZnS, and a top insulator layer of 2400 Å Al_2O_3. Structure B was made without the ZnS buffer layers, i.e., SrS, followed by Al_2O_3, both of the same thicknesses of structure A. The more detailed device fabrication conditions were described in chapter 4. As mentioned earlier, the purpose of the ZnS buffers layer is to protect SrS from being oxidized.

The EL emission and PL emission spectra of Eu doped devices with structure A (i.e. with ZnS buffer layer) are shown in Fig. 6.2.1. The EL emission was bright (9 cd/m^2 at 40 V above threshold, 1 kHz) and violet in color with a peak at 406 nm and full width at half maximum (FWHM) of 20 nm. The lifetime was 1 μs, and it was determined by measuring the decay time with a photon detector while a voltage pulse was applied. This is a relatively bright light source considering the location of the peak on the photonic sensitivity curve. The corresponding PL spectrum excited by 360 nm light from an Ar ion laser also shows a bright violet emission.

These results were very interesting since other TFEL device research groups have reported only orange-red light from similar SrS:Eu device structures [80, 81]. It is likely that our ALE grown samples were unintentionally doped with chlorine, since $ZnCl_2$ was used as a precursor for the ZnS buffer layer growth. Grazing incidence X-ray analysis

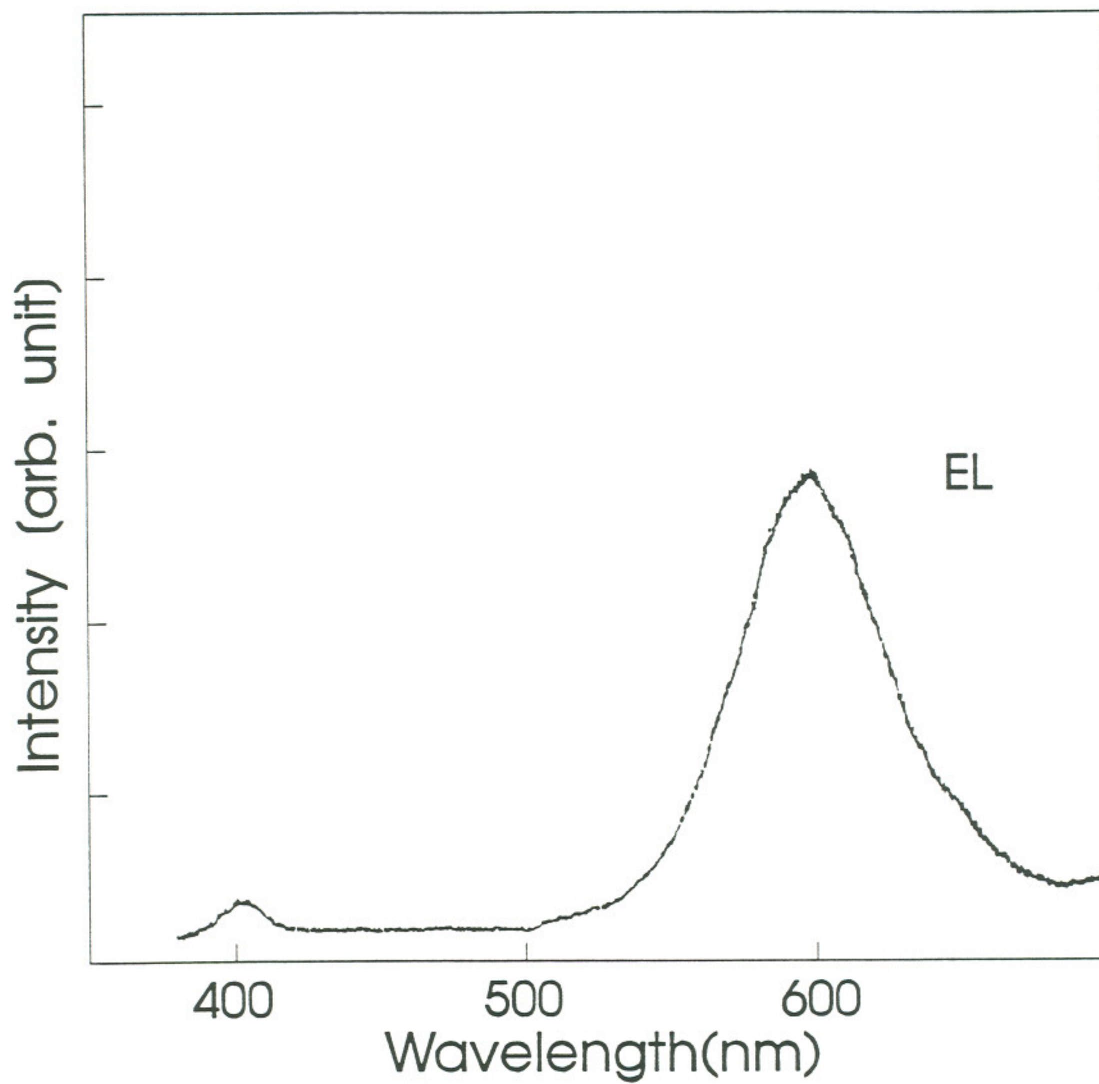

Fig. 6.2.2 Electroluminescent emission spectrum of type B device, SrS:Eu without ZnS buffer layers.

indeed showed, besides SrS (cubic phase) and ZnS (hexagonal phase), the presence of cubic $SrCl_2$ (see Fig. 6.2.4). It is worth noting that when SrS:Eu is co-doped with F or Cl, the results in the literature showed either a small wavelength shift or some change in the emission spectrum profile [80, 81], but no violet light emission from thin film EL devices have been reported. It was identified that the source of the violet emission is the $4f^6 5d$ to $4f^7$ ($^8S_{7/2}$, Eu^{2+} ground state) transition of Eu^{2+} in the $SrCl_2$ host, i.e., $SrCl_2:Eu^{2+}$. One of the earliest detailed reports of violet photoluminescence from Eu doped $SrCl_2$ crystals dates back to 1948 [82]. More recently, several investigations have shown that Eu^{2+} in alkaline earth fluoride and chloride hosts exhibits efficient 5d to 4f ($^8S_{7/2}$) emission [83, 84, 85]. In particular, T. Kobayasi reported PL emission from a $SrCl_2$:Eu crystal. Their findings are, at 293 K, peak wavelength = 410 nm, FWHM = 19 nm, lifetime = 0.95 μs, quantum efficiency = 0.93 with the excitation wavelength at 253.7 nm [86]. Their spectrum and lifetime results match our findings well .

To reduce the amount of chlorine, a second set of devices which do not contain the ZnS buffer layers (structure B), were fabricated. The devices emitted orange-red light and the EL emission spectrum is shown in Fig 6.2.2. The broad major peak centered at 610 nm is the $4f^6 5d$ to $4f^7$ ($^8S_{7/2}$) transition. The result agrees with the findings reported by the TFEL device researchers mentioned earlier.

It has been pointed out before that the electrons of rare earth elements in the 5d state have a strong interaction with the conduction band minimum of alkaline-earth sulfide lattices. This is also true for chloride crystals, i.e. the 5d electrons in Eu^{2+} interact strongly with the $SrCl_2$ host. T. Kabayasi has reported a 20 nm shift to shorter wavelength for the same transition of Eu^{2+} in a $BaCl_2$ crystal vs. a $SrCl_2$ crystal [86]. The transition

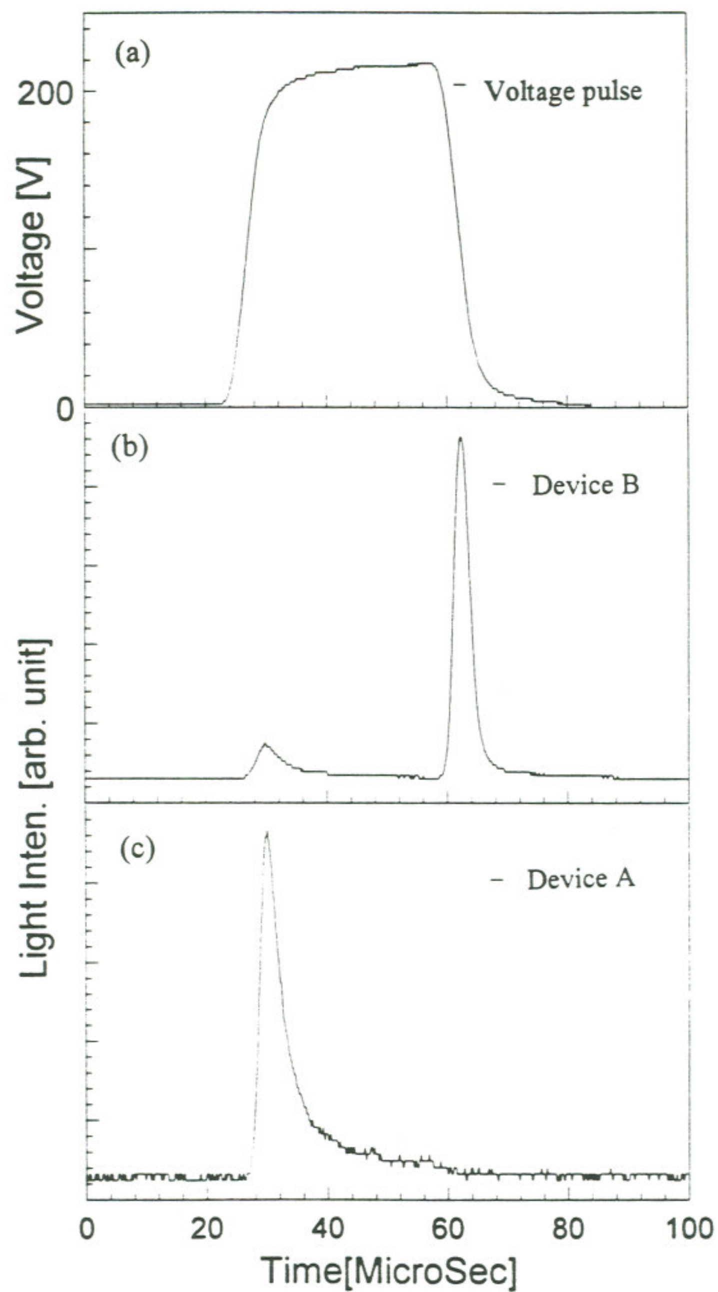

Fig. 6.2.3 The driving voltage pulse (a); the corresponding emission of orange-red light from type B devices (b); and violet light from type A devices (c).

energy shift from SrS to $SrCl_2$ is expected to be even stronger owing to the big difference of crystal field strength and symmetry, as we have observed.

To investigate the excitation mechanism of these devices (A and B type), the light pulse vs. time was measured by the photon detector, as shown in Fig 6.2.3. One can see that most of the light is emitted at the falling edge of the driving voltage pulse for the device with structure B (without ZnS buffer). This is evidence for the recombination excitation mechanism in the SrS host. For the device with structure B, the SrS:Eu device, Eu^{2+} is believed to be ionized to Eu^{3+} and the electrons lost in the conduction band become part of the polarization charge. When the external field is removed, electrons are recaptured by the Eu^{3+} ions due to Coulombic attraction, and become Eu^{2+} at the 4f5d state. They then de-excite back to the 4f ground state and emit light. For the device with structure A, the $SrCl_2$:Eu device, the light pulse is emitted at the leading edge, implying that the Eu^{2+} activators in the $SrCl_2$ host are excited by direct hot electron impact excitation and there is no interaction with the conduction band of $SrCl_2$. It is interesting to note that in Fig. 6.2.2, the same violet peak as for device A is observed, although it is quite weak. This was probably due to the fact that some $SrCl_2$ was formed at the SrS-Al_2O_3 interfaces, because $AlCl_3$ was the source used to grow Al_2O_3.

As already pointed out, X-ray analysis of the violet light emitting devices (structure A) showed presence of both SrS and $SrCl_2$. Therefore we expect thin layers of $SrCl_2$ to be located near the two SrS-ZnS interfaces. The chlorine source for the $SrCl_2$ formation is from residual $ZnCl_2$. If this is true more $SrCl_2$ formation should occur provided the number of SrS-ZnS interfaces increase. For this reason another sample was made, under the same growth condition, with ten periods of ZnS-SrS thin layers where each layer was 500 Å thick. In Fig. 6.2.4, the X-ray diffraction pattern of the devices with

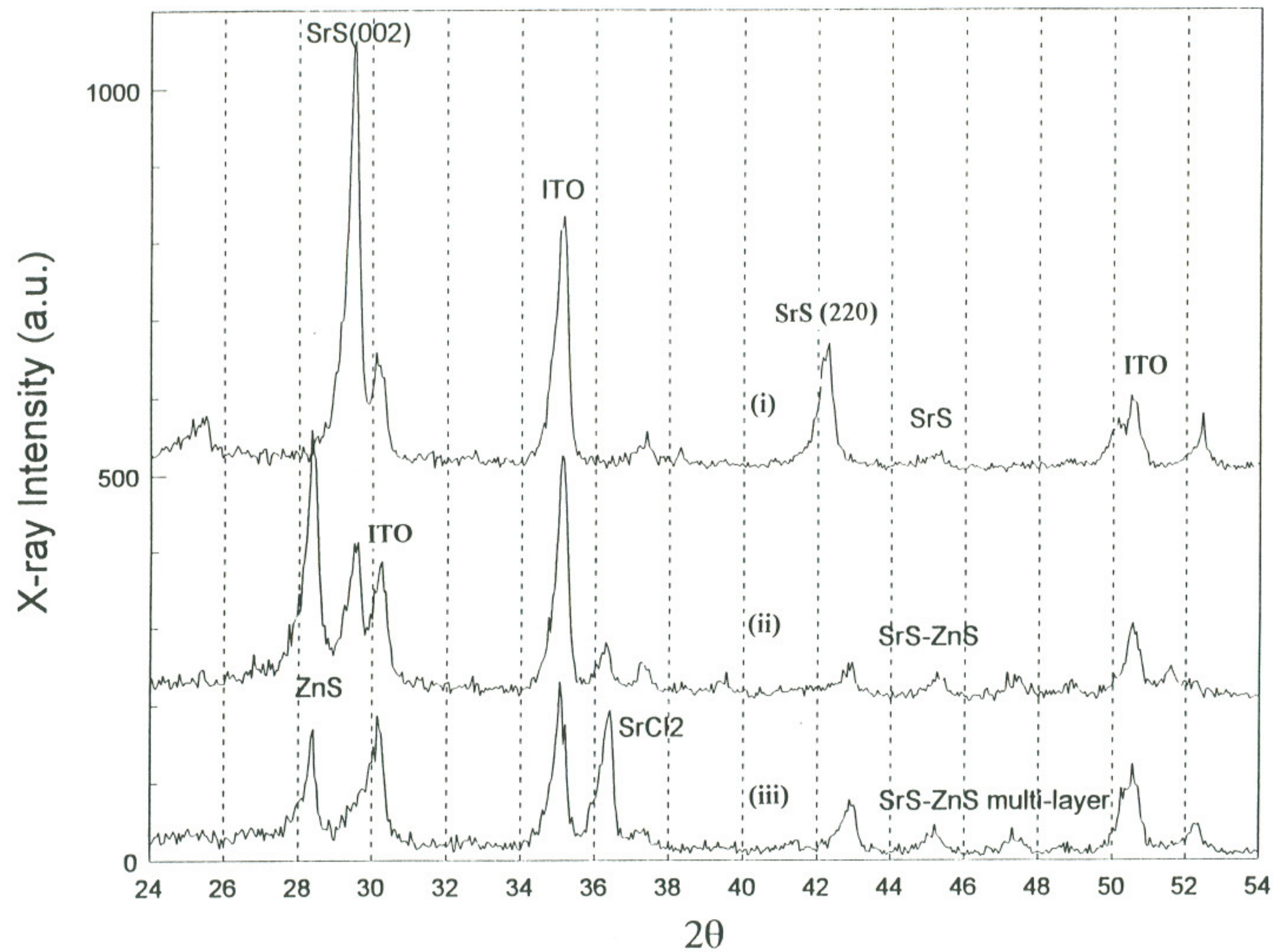

Fig. 6.2.4 X-ray diffraction patterns of (i) device type B, without ZnS layer; (ii) device type A, two ZnS buffer layers; (iii) device with ten ZnS-SrS alternative layers.

structure B, structure A and the multi-layer structure are marked with (i), (ii), (iii) respectively. The cubic phase $SrCl_2$ (220) peak located at $2\theta = 36.4^o$ does not show in (i) (the device without ZnS layer); a weak peak in (ii) (two ZnS buffer layers); a strong peak in (iii) (ten ZnS-SrS layers).

It should be noted that the attempt to make the violet light emission brighter by increasing the number of ZnS-SrS interface has failed (based on a limited number of experiments). These devices were too dim to measure the brightness and were short lived. A possible reason is that the crystal quality is poor when the device consists of many lattice mismatching layers

Cerium doped SrS devices with structure A (with ZnS buffer layer) were similarly fabricated and characterized for emission. The emission spectrum of the device with structure A is shown in Fig. 6.2.5. Besides the expected 5d to 4f ($^2F_{7/2}$) transition in the SrS host which is in the blue-green range, a peak which originates from the same 5d to 4f transition but in $SrCl_2$ host was observed. The new peak centered at 360 nm with FWHM = 15 nm. The peak actually consist of two transitions, one is 5d to $^2F_{7/2}$ (367 nm), the other is 5d to $^2F_{5/2}$ (344 nm) [87].

The emission spectrum of the device with structure B (no ZnS buffer layer) is shown in Fig. 6.2.6. The transition is identified as the Ce^{3+} 5d state to the 4f ($^2F_{5/2,7/2}$) states, where $^2F_{5/2}$ corresponds to the peak at higher energy. The light pulse vs. time relation bears the same characteristics as SrS:Eu in Fig 6.2.3 (b), i.e. the emission happened at the falling edge of the voltage pulse. Therefore the recombination mechanism is dominant for the SrS:Ce type devices.

In this section, two types of device structures were discussed, namely a phosphor layer consisting of SrS only and a phosphor layer consisting of ZnS and SrS doped with

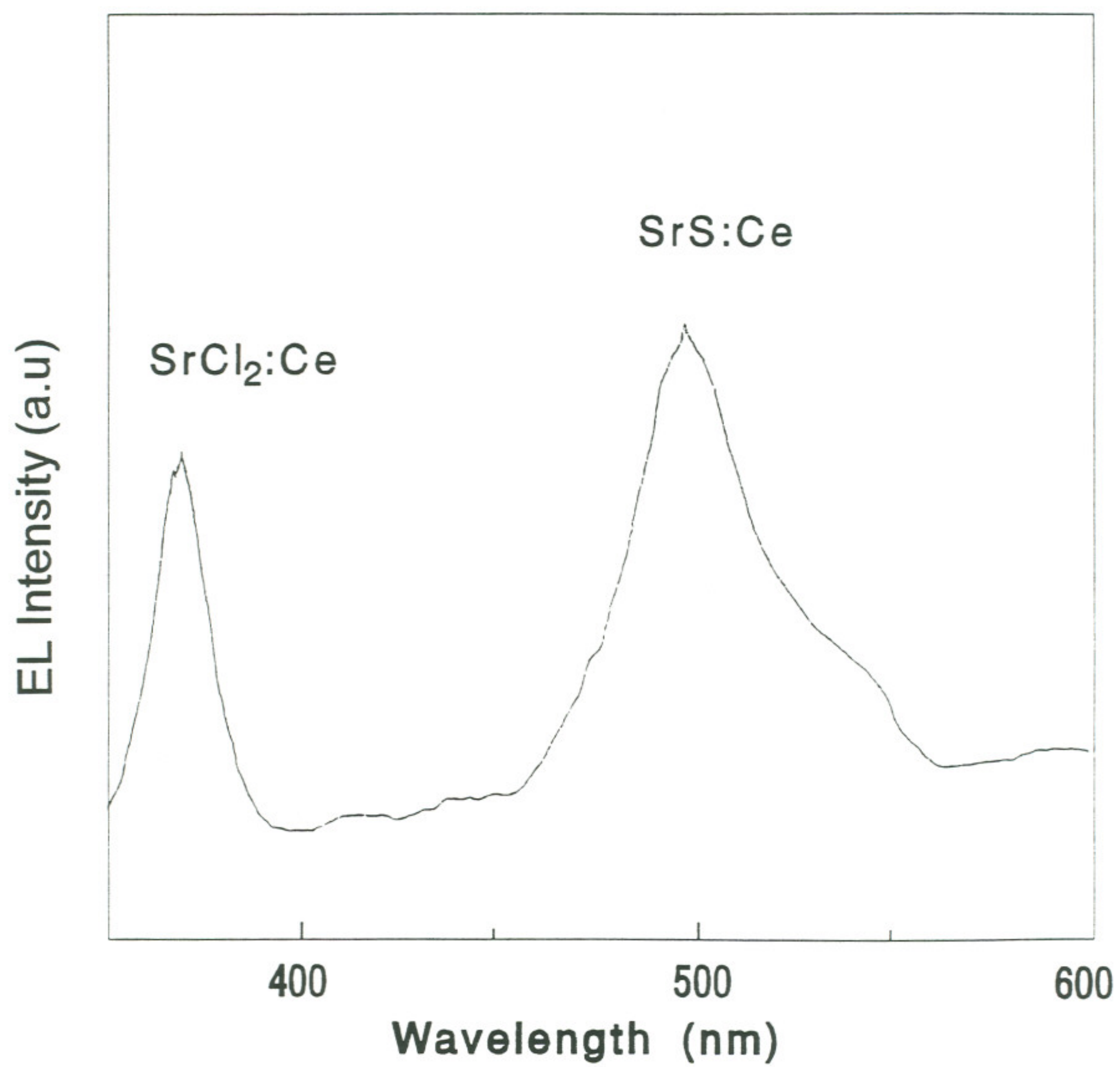

Fig. 6.2.5 EL spectrum of the UV light emission from $SrCl_2$:Ce in type A devices.

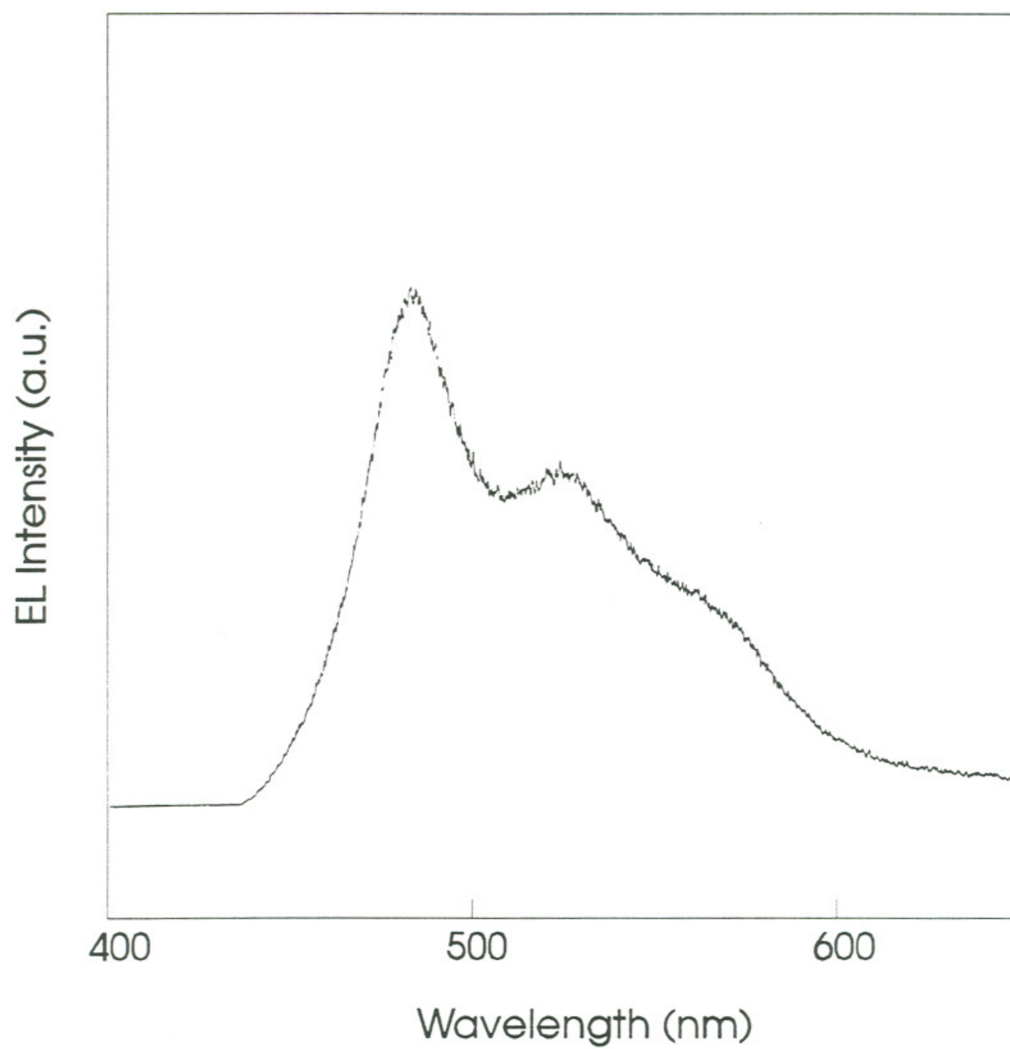

Fig. 6.2.6 Electroluminescent emission spectrum of type B devices, SrS:Ce without ZnS buffer layers.

Ce and Eu respectively. The intention was to fabricate a bright TFEL with blue (SrS:Ce) and red (SrS:Eu) emission. The discovery and identification of violet and UV emission from $SrCl_2$:Eu and $SrCl_2$:Ce was unexpected but leads to interesting prospects. The concept of $SrCl_2$:Eu TFEL devices emitting 406 nm deep blue light could be developed into a new phosphor contributing to the much needed blue color in the electroluminescent spectrum.

6.3 Summary

In this chapter, SrS:Pr and ZnS:Pr phosphors which emit white light were studied. SrS is a better host material for Pr than ZnS, because the SrS lattice matches the size of Pr atoms better. The emission spectra of Pr from both hosts are identical due to the shielded f-f transitions. Although Pr based phosphors emit white light, they are not suitable for full color display applications. The reason is that the emission spectrum from the Pr ion consists of a blue-green peak ($^3P_0$-$^3H_4$) and a red peak ($^3P_0$-$^3F_2$) but lacks the colors in between.

SrS:Eu and SrS:Ce phosphor based devices were studied because these two phosphors provide the blue-green and the orange-red colors. A combination of these two would produce a white phosphor with a broad band spectrum. As a result of our study, the blue-green and orange-yellow light emitting phosphors were observed as expected. In addition, the purple and UV light emitting phosphors, $SrCl_2$:Eu and $SrCl_2$:Ce were observed. The CIE coordinates of the studied devices are shown in the CIE diagram in Fig. 6.3.1. The CIE coordinate from the $SrCl_2$:Eu device provides a much needed color for full color display applications.

Table V. Summary of TFEL devices emission characteristics

	Energy levels	Light pulse*	Lifetime (μs)	CIE coordinates
$ZnS:Tb^{3+}$	$4f^8\,(^5D_4)$- $4f^8\,(^7F_{6,5,4,3})$	LE	>400	x=0.32 y=0.61
$ZnS:Pr^{3+}$	$4f^2\,(^3P_0)$- $4f^2\,(^3H_{6,5,4},{}^3F_2)$	LE	17	x=0.31 y=0.39
$SrS:Pr^{3+}$	$4f^2\,(^3P_0)$- $4f^2\,(^3H_{6,5,4},{}^3F_2)$	LE	33	x=0.36 y=0.39
$SrS:Eu^{2+}$	$4f^65d^1$(**)- $4f^7(^8S_{7/2})$	FE	< 1	x=0.60 y=0.39
$SrS:Ce^{3+}$	$5d^1\,(^2D)$- $4f^1(^2F_{5/2})$	FE	< 1	x=0.25 y=0.42
$SrCl_2:Eu^{2+}$	$4f^65d^1$(**)- $4f^7(^8S_{7/2})$	LE	< 1	x=0.17 y=0.01
$SrCl_2:Ce^{3+}$	$5d^1\,(^2D)$- $4f^1(^2F_{5/2})$	LE	< 1	UV UV
$ZnS:Mn^{2+}$	$3d^5$ - $3d^5$	LE	>400	x=0.53 y=0.48

* Light pulse coming out at leading edge: LE, or falling edge: FE; FE indicates recombination and LE indicates direct electron impact.

** No energy level related to the 4f5d state is designated by the notation based on LS coupling due to their strong interaction with host lattice.

Table V summarizes the emission characteristics of the TFEL devices that have been covered in this study. A few points about rare earth ion activators can be summarized from our comparative study; (i) f state to f state transition is insensitive to the crystal field perturbation due to the screening effect of 5s5p electrons, this was shown by comparing the emission spectra from ZnS:Pr and SrS:Pr based devices; (ii) d state to f state transition is susceptible to the host lattice crystal field, the same activator can emit a different color of light determined by the host lattice; (iii) d to f parity allowed transitions

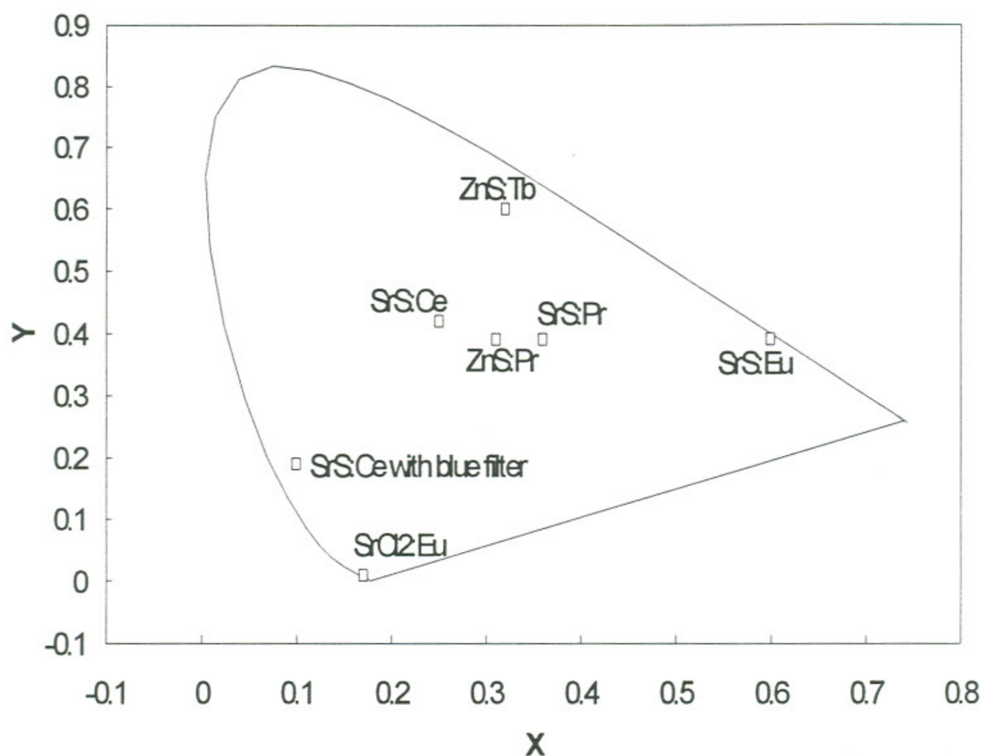

Fig. 6.3.1 CIE (Commission Internationale de l'Eclairage) coordinates measured from the studied devices shown in the CIE diagram. The CIE number of SrS:Ce with blue filter is from the reference [88].

can be characterized as having a shorter life time, while f to f parity forbidden transitions can be characterized as having longer life time.

Chapter 7
Summary and Conclusions

During the research described in this thesis, the F-120 ALE reactor was used to grow Al_2O_3, ZnS and SrS thin films. It was found that, besides reactant gas flow rate, substrate temperature plays an important role on thin film growth rate and its microstructure.

For Al_2O_3, the surface reaction was found to be exothermic determined from growth rate vs. temperature plot, and the thin film was identified as amorphous by X-ray diffraction data. The temperature window for growing good quality Al_2O_3 thin film was found having a wide range, from 400 °C to 500 °C (it could be beyond this range but no experiments were performed). This flexibility provides conveniences during device fabrication whereas several layers of thin films were grown sequencially in one run.

For ZnS, atomic force microscope studies showed that the grain size was small in the beginning of thin film growth and grew to larger size (from 80 nm at thickness of 36 nm to 250 nm at thickness of 540 nm) in the growth process. This finding suggests that the ZnS phosphor structure was not symmetric across the two sides owing to the grain growing larger. It was also noted from the electrical measurement that there were asymmetrical phenomena when a symmetrical bilopar pulse was applied to the ZnS:Tb device. The X-ray diffraction data showed that the thin film had a tendency to be in hexagonal phase at higher temperature (500 °C, substrate) and to be in cubic phase at lower temperature (400 °C, substrate). X-ray diffraction data showed improvements in

terms of crystal quality for the devices treated with post growth RTA at 700 °C. As a result, the annealed device also had better electroluminescence efficacy.

For SrS thin films, the crystal structure is a sodium-chloride type cubic structure per X-ray diffraction data. SrS appeared to react sensitively with moisture and oxygen. The devices usually had to be tested soon after the finish of its fabrication in order to get the best performance. Still the devices degraded during characterization. The reason could be due to the impurities in the $Sr(thd)_2$ powder, which is the strontium precursor used. It had been difficult to get consistant results from batch to batch during the fabrication of SrS based devices. In additon, it was found that a cubic phase of $SrCl_2$ can be formed near a ZnS-SrS interface, where Cl stems from $ZnCl_2$ which is the precursor of Zn for growing ZnS.

Electrical and optical properties of ZnS:Tb based devices were characterized by various techniques, including C-V measurement, internal field and polarization charge measurements, brightness vs. frequency measurements at room temperature and 77 K (to show the effect of thermal quenching). These measurements mostly were omitted for the SrS based devices due to the unstable device performance as mentioned above. The enhancement and attenuation of EL emissoin by UV irradiation on ZnS:Tb devices showed that the polarization charge was critical for luminescent efficacy. Rapid thermal annealing (RTA) was performed on ZnS:Tb based devices and showed a positive effect (about 10%) on electroluminescent efficacy. Numerical modeling based on the tunneling theory was performed, and a successful fit of the C-V characteristic to experimental data was achieved. The modeled parameters related to the electron density of state function was extracted through the curve fittings. The model showed that the active interface states are located near 0.7 eV below the ZnS conduction band.

A few kinds of dopants including Tb, Pr, Eu and Ce have been incorporated into ZnS and SrS devices. Electroluminescence and photoluminescence spectra for those devices were taken in order to understand the energy levels and the transition mechanisms of these optical activators. Brightness and CIE (Commission Internationale de l'Eclairage) numbers were measured as these parameters are important for the end display products. The transition energy levels of those activators have been identified in the corresponding host lattices. Two major excitation mechanisms, direct impact excitation and recombination mechanisms, have been differentiated accordingly by observing the dynamics of optical responses from the devices. For the first time, two new emission peaks 406 nm from $SrCl_2$:Eu and 360 nm from $SrCl_2$:Ce were observed from TFEL devices. The corresponding emission mechanism and energy levels were identified. The concept from the $SrCl_2$:Eu based deep blue light emitting device could be useful in the next generation full color TFEL display applications.

There are several issues remain unsolved during the cause of work. A systematic study on the luminescence performance of these devices is important. Further improvement of the device luminescence efficacy is always desired for making a commercial product. Many factors can contribute to the electroluminescence efficacy of a TFEL device. Among them two parameters are crucial, according to the discussion in chapter 4:

(i) the EL efficiency: this was characterized for the annealed and un-annealed ZnS:Tb devices. The annealed device had a better EL efficiency than the un-annealed one. The EL efficiency for the SrS based devices needs to be studied.

(ii) the amount of polarization charge, i.e. how much free charge can be generated at a given voltage, is important. This was indicated by the effect of UV radiation on

polarization charge measurement. If part of the polarization charge cannot be held (in the interface states) and relaxed back (assisted by UV light in this case), the brightness goes down. It would be interesting to observe the effect of UV radiation on the SrS:Eu and SrS:Ce based devices since the recombination mechanism is involved in the energy transition process for these two types of devices.

Another factor needs to be considered, that is the lifetime of the activator. For ZnS:Tb based devices, brightness vs. frequency measurement showed brightness saturation towards higher frequency (10 kHz). One of the reasons for the saturation, besides thermal quenching, is that Tb^{3+} has a long lifetime (> 400 μs). The SrS:Ce and SrS:Eu have an advantage in the aspect of frequency saturation because of their shorter lifetimes.

The effects of space charge might be important for the SrS:Ce and SrS:Eu based devices because the activators contribute to the total amount of polarization charge. The research on this subject needs to be conducted once a more stable SrS based device can be achieved.

It has been puzzling that for those $SrCl_2$ based devices, some devices showed an EL spectrum primarily from a $SrCl_2$ host; some devices showed a mixed spectrum, both $SrCl_2$ and SrS made a contribution. Additionally, the only few devices made with alternating SrS and $SrCl_2$ multi-layer device did not have a good EL or PL emission. A more thorough micro structure analysis, such as SEM or TEM study for these devices is needed before we can try to explain these puzzles.

References

[1] S. Morozumi, Advances in Electronics and Electron Physics **77**, 1 (1990).

[2] T. Scheffer, J. Nehring, M. Kaufmann, H. Amstutz, D. Heimgartner and P. Eglin, SID International Symposium Digest of Technical Papers **16**, 120 (1985).

[3] T. Scheffer, J. Nehring, *SID Seminar Lecture Notes 1*, Washington State Convention Center, Seattle, Washington, 1993, M-7/1(1993).

[4] Y. Takano, H. Murakami, T. Sakai, T. Kuriyama, K. Takahashi, SID International Symposium Digest of Technical Papers **25**, 731 (1994).

[5] N. Kumar, H. Schmidt, M. Clark, A. Ross, B. Lin, L. Fredin, B. Baker, D. Patterson, W. Brookover, C. Xie, C. Hilbert, R. Fink, C. Potter, A. Krishnan, D. Eichman, SID International Symposium Digest of Technical Papers **25**, 43 (1994).

[6] C. King, *SID Seminar Lecture Notes 1*, San Jose Convention Center, July, 1994, M-9/3 (1994).

[7] T. Ogura, A. Mikami, K. Tanaka, K. Taniguchi, M. Yoashida and S. Nakajima, Appl. Phys. Lett. **48**, 1570 (1986).

[8] K. Okamoto, T. Yoshimi and S. Miura, Appl. Phys. Lett. **53**, 678 (1988).

[9] T. Peters and J. Baglio, J. Electrochem. Soc.: Solid-State Sci. & Tech. **2**, 119 (1972).

[10] W. Barrow, R. Coovert, E. Dickey, C. King, C. Laakso, S. Sun, R. Tuenge, R. Wentross, J. Kane, SID International Symposium Digest of Technical Papers **24,** 761 (1993).

[11] W. Barrow, R. Coovert, C. King, SID International Symposium Digest of Technical Papers **15**, 294 (1984).

[12] H. Xian, G. Zhong, S. Tanaka, J.J. Appl. Phys. **28**, L1019 (1989).

[13] H. Ohnishi and T. Okuda, SID International Symposium Digest of Technical Papers **20**, 317 (1989).

[14] G. Destriau, J. Chim. Phys. **33**, 587 (1936).

[15] E. Chase, R. Hepplewhite, D. Krupka and D. Kahng, J. of Appl. Phys. **40**, 2512 (1969).

[16] T. Inoguchi, M. Taketa, Y. Kakihara, Y. Nakata, M. Yoshida, SID International Symposium Digest of Technical Papers **5**, 86 (1974).

[17] K. Yang, *Electrical & Optical Measurements on A.C. Thin-Film Electroluminescent Devices*, Ph.D. Dissertation, Department of Electrical Engineering, Oregon State University (1981).

[18] T. Inoguchi, S. Mito, *Electroluminescence,* by Springer Proc. Phys., Edited by J.I. Pankove, 202 (1977).

[19] D. Krupka and D. Mahoney, J. Appl. Phys. **43**, 2314 (1972).

[20] S. Kobayashi, J. Wager and A. Abu-Dayah, *Proceedings of the Sixth Internaltional Workshop on Electroluminescence*, El Paso, TX, 1992, edited by V. Singh and J. McClure, p. 234.

[21] Z. Zhang, B. Zhang, W. Zhao, X. Jiang, Z. Liu and S. Xu, J. Crystal Growth **117**, 1012 (1992).

[22] A. Aguilera, V. Singh and D. Morton, SID International Symposium Digest of Technical Papers **25**, 565 (1994).

[23] D. Smith, J. of Lumin. **23**, 209 (1981).

[24] H. Fitting, A. Von Czarnowski and G. Muller, J. Crystal Growth **101**, 876 (1990).

[25] R. Mach and G. Muller, J. Crystal Growth **101**, 967 (1990).

[26] K. Bhattacharyya, S. Goodnick, J. Wager, J. Appl. Phys. **73**, 3390 (1993).

[27] J. Fogarty, W. Kong, R. Solanki, SID International Symposium Digest of Technical Papers **25**, 569 (1994).

[28] K. Brennan, J. of Appl. Phys. **64**, 4024 (1988).

[29] C. Wolfe, N. Holonyak, Jr. and G. Stillman, *Physical properties of semiconductors*, Prentice Hall, Englewood Cliff, NJ, 299 (1989).

[30] T. Thompson, J. Allen, J. Phys. C: Solid State Phys. **20**, L499 (1987).

[31] E. Bringuier, J. Appl. Phys. **75**, 4291 (1994).

[32] D. Krupka, J. Appl. Phys. **43**, 476 (1972).

[33] J. Allen, *Electroluminescence*, by Springer Proc. Phys. **38**, 10 (1989).

[34] J. Allen, J. Lumin. **48**, 18 (1991).

[35] S. Keller, J. Mapes and G. Cheroff, Phys. Rev. **108**, 663 (1957).

[36] C. Sawyer and C. Tower, Phys. Rev. **35**, 269 (1930).

[37] S. Tanaka, H. Yoshiyama, Y. Mikami, J. Nishiura, S. Ohshio, H. Kobayashi, Japan Display '86, 242 (1986).

[38] A. Abu-Dayah, S. Kobayashi, J. Wager, Appl. Phys. Lett. **62**, 744 (1993).

[39] J. Davidson, J. Wager, I. Khormaei, C. King, R. Williams, IEEE Tran. on Elec. Dev., **39**, 1122 (1992).

[40] J. Wager, A. Douglas and D. Morton, *Proceedings of the Sixth Internaltional Workshop on Electroluminescence*, El Paso, TX, 1992, edited by V. Singh and J. McClure, p. 92.

[41] Y. Ono, H. Kawakami, M. Fuyama and K. Onisawa, Jpn. J. Appl. Phys. **26**, 1482 (1987).

[42] C. Kittel, *Intruduction to Solid State Physics*, 5th edition, by John Wiley & Sons, Inc., 441(1976).

[43] A. Kitai, *Solid State Luminescence*, by Chapman & Hall, edited by A. Kitai, 17 (1993).

[44] S. Tanaka, J. Crystal Growth, **101**, 958 (1990).

[45] H. Moos, J. Lumin. **1**, 106 (1970).

[46] G. Blasse, *Solid State Luminescence*, published by Chapman & Hall, edited by A. Kitai, 21 (1993).

[47] E. Bringuier, J. Appl. Phys. **66**,1314 (1989).

[48] E. Bringuier and A. Geoffroy, Appl. Phys. Lett. **60**, 1256 (1992).

[49] K. Neyts and P. De Visschere, J. Appl. Phys. **68**, 4163 (1990).

[50] T. Suntola and J. Antson, US Patent No. 4058 430 (1977).

[51] T. Suntola, J. Anston, A. Pakkala and S. Linfors, SID International Symposium Digest of Technical Papers **11**, 108 (1980).

[52] M. Simpson, P. Smith and G. Dederski, Surface Engineering **3**, 343 (1987).

[53] T. Suntola, Acta Polytecn. Scand., Electrical Engineering Series **64**, 242 (1989).

[54] T. Suntola, Material Science Report **4**, 261(1989).

[55] M. Leskela, L. Niinisto, E. Nykanen, P. Soininen and M. Tiitta, Acta Polytecn. Scand., Chemical Technology & Metallurgy Series **195**, 193 (1990).

[56] Sampuran-Singh and Anand, K.V., Thin Solid Films **37**, 453 (1976).

[57] S. Wolfe and R. Tauber, *Silicon Processing for the VLSI Era*, *Vol I*, by Lattice Press (1986).

[58] C. Goodman and M. Pessa, J. Appl. Phys. **60**, R65 (1986).

[59] A. Yariv, *Quantum Electronics, 2nd Ed.*, by Wiley (1975).

[60] M. Oikkonen, M. Blomberg, T. Tuomi and M. Tammenmaa, Thin Solid Films **124**, 317 (1985).

[61] J. Mita, M. Koizumi, H. Kanno, T. Hayaski, Y. Sekido, I. Abiko and K. Nihei, Jpn. J. Appl. Phys. **26**, L1205 (1987).

[62] A. Mikami, T. Ogura, K. Tanaka, K. Taniguchi, M. Yoshida and S. Nakajima, J. Appl. Phys. **61**, 3028 (1987).

[63] E. Soininen, Private communication (1994).

[64] M. Tammenmaa, H. Antson, M. Asplund, L. Hiltunen, M. Leskela, L. Niinisto, E. Ristolainen, J. Crys. Grow. **84**, 151 (1987).

[65] M. Leskela, L. Niinisto, E. Nykanen, P. Soininen and M. Tiitta, Mat. Res. Symp. Proc., 222 (1991).

[66] P. Flinn and G. Waychunas, J. Vac. Sci. Technol. **B 6**, 1749 (1988).

[67] V. Tanninen and T. Tuomi, Thin Solid Films **90**, 339 (1982).

[68] T. Shibata, K. Hirabayashi, H. Kozawaquchi and B. Tsjiyama, Jpn. J. Appl. Phys. **26**, L1664 (1987).

[69] R. Pappalardo amd M. Levinson, J. Appl. Phys. **66**, 6189 (1989).

[70] R. Pappalardo, J. Electrochem. Soc. **137**, 3469 (1990).

[71] D. Kim, F. Qian, R. Solanki, T. Tuenge and C. King, Mat. Res. Soc. Symp. **100**, 743 (1988).

[72] W. Kong, J. Fogarty and R. Solanki, Appl. Phys. Lett. **65**, 670 (1994).

[73] K. Bhattacharyya, S. Goodnick and J. Wager, J. Appl. Phys. **73**, 3390 (1993).

[74] J. Fogarty, W. Kong and R. Solanki, SID International Symposium Digest of Technical Papers **25**, 569 (1994).

[75] E. Bringuier, SID International Symposium Digest of Technical Papers **25**, 847 (1993).

[76] S. Tanaka, S. Ohshio, J. Nishiura, H. Kawakami, H. Yoshiyama and H. Kobayashi, Appl. Phys. Lett. **52**, 2102 (1988).

[77] W. Kong, J. Fogarty and R. Solanki, and D. Tuenge, Appl. Phys. Lett. **66**, 419 (1995).

[78] J. Li, Y. Lin, Y. Su, T. Wu and M. Yokoyama, *Prog. Crystal Growth and Charact.* **25**, 103(1992).

[79] H. Kobayashi, SPIE **1910**, 15 (1993).

[80] H. Xian, G. Zhong, S. Tanaka and H. Kobayashi, Jpn. J. Appl. Phys. **28**, L1019 (1989).

[81] B. Huettle, G. Mueller, R. Mach, C. Fanassier, J. Kreissi, P. Benalloiu, H. Xian and C. Barthou, *Proceedings of the Sixth Internaltional Workshop on Electroluminescence*, El Paso, TX, 1992, edited by V. Singh and J. McClure, p. 123.

[82] S. Freed and S. Katcoff, Physica **XIV**, 17 (1948).

[83] L. Brixner and A. Ferretti, J. of Solid State Chem. **18**, 111(1976).

[84] J. Lawson and S. Payne, Phys. Rev. **B 47**, 14003 (1993).

[85] U. Caldino G., M. Villafuerte-Castrejon and J. Rubio O., Crystal. Latt. Def. and Amorph. Mat. **18**, 511 (1989).

[86] T. Kobayasi, S. Mroczkowski, J. Owen and L. Brixner, J. Lumin. **21**, 247 (1980).

[87] O. Antonyyak, I. Kityk and N. Pidzyrallo, Opt Spectrosc. **63**, 311 (1987).

[88] M. Godlewski and M. Leskela, Critical Reviews of Solid State and Material Science **19**, 108 (1994).

Vita

The author, Weiran Kong, was born in Beijing, China, in August, 1963. He enrolled in NanKai University in 1981 and received B.S. in Physics in 1985. Following graduation from NanKai University, he was employed as an instructor in the Department of Electrical Engineering at Beijing Institute of Technology. In 1989 he enrolled in the Physics Dept. at Texas Tech University with a scholarship. In 1990, he entered Oregon Graduate Institute of Science & Technology to pursue a Ph.D. degree, and received M.S.E.E. and Ph.D. in Applied Physics in 1993 and 1996, respectively. He has co-authered several scientific publications and was a major contributor to a U.S. patent during the years at OGI.

LIST OF PUBLICATIONS:

[1] W. Kong and R. Solanki, "The effect of ultraviolet radiation on a ZnS:Tb thin film electroluminescent device", J. of Appl. Phys. **75**, 3311 (1994).

[2] W. Kong, J. Fogarty and R. Solanki, "Atomic layer epitaxy of ZnS:Tb thin film electroluminescent devices", Appl. Phys. Lett. **65**, 670 (1994).

[3] J. Fogarty, W. Kong and R. Solanki, "Monte Carlo simulation of electrical characteristics of high-field ACTFEL devices", SID Digest of technical papers **25**, 569 (1994).

[4] W. Kong, J. Fogarty and R. Solanki, and D. Tuenge "White light emitting ZnS:Pr and SrS:Pr electroluminescent devices fabricated via atomic layer epitaxy", Appl. Phys. Lett. **66**, 419 (1995).

[5] W. Kong, J. Fogarty and R. Solanki, "Violet light emitting electroluminescent devices by atomic layer epitaxy", Appl. Phys. Lett. **67**, 7 (1995).